LIÈGE université Library

https://lib.uliege.be

https://matheo.uliege.be

Active Layer Depth Characterization Using UAV-Based Hyperspectral Remote Sensing Université de Liège

Auteur : Boisbourdin, Sami
Promoteur(s) : Jonard, François
Faculté : Faculté des Sciences appliquées
Diplôme : Master en ingénieur civil en aérospatiale, à finalité spécialisée en "aerospace engineering"
Année académique : 2025-2026
URI/URL : http://hdl.handle.net/2268.2/26081

Avertissement à l'attention des usagers :

Tous les documents placés en accès ouvert sur le site le site MatheO sont protégés par le droit d'auteur. Conformément aux principes énoncés par la "Budapest Open Access Initiative"(BOAI, 2002), l'utilisateur du site peut lire, télécharger, copier, transmettre, imprimer, chercher ou faire un lien vers le texte intégral de ces documents, les disséquer pour les indexer, s'en servir de données pour un logiciel, ou s'en servir à toute autre fin légale (ou prévue par la réglementation relative au droit d'auteur). Toute utilisation du document à des fins commerciales est strictement interdite.

Par ailleurs, l'utilisateur s'engage à respecter les droits moraux de l'auteur, principalement le droit à l'intégrité de l'oeuvre et le droit de paternité et ce dans toute utilisation que l'utilisateur entreprend. Ainsi, à titre d'exemple, lorsqu'il reproduira un document par extrait ou dans son intégralité, l'utilisateur citera de manière complète les sources telles que mentionnées ci-dessus. Toute utilisation non explicitement autorisée ci-avant (telle que par exemple, la modification du document ou son résumé) nécessite l'autorisation préalable et expresse des auteurs ou de leurs ayants droit.



UNIVERSITE DE LIEGE
FACULTE DES SCIENCES APPLIQUEES



Université de Liège
Faculté des Sciences Appliquées

Active Layer Depth Characterization Using UAV-Based Hyperspectral Remote Sensing

Thesis presented to obtain the degree of
Civil Engineer in [Aerospace Engineering]

by

Sami Boisbourdin

Thesis supervisor : **Jonard François**

Academic year 2025–2026

Abstract

Permafrost degradation is one of the most significant consequences of climate warming in Arctic regions. Active Layer Depth (ALD), defined as the maximum seasonal thaw depth above permafrost, is widely used as an indicator of permafrost dynamics. However, traditional monitoring methods mainly rely on field measurements that provide accurate but spatially limited observations. In this context, UAV-based hyperspectral remote sensing offers new opportunities for investigating environmental variables associated with ALD variability.

This thesis evaluates the potential of hyperspectral imagery acquired by an unmanned aerial vehicle (UAV) for the characterization of ALD near Eight Mile Lake, Interior Alaska. A complete preprocessing workflow was implemented to transform raw hyperspectral acquisitions into atmospherically corrected reflectance mosaics, which were combined with field measurements of ALD.

Several complementary analyses were conducted, including spectral correlation analysis, vegetation indices, Principal Component Analysis (PCA), and Random Forest machine learning models. Feature selection strategies, DEM integration, and model robustness were also investigated.

The results demonstrate that hyperspectral imagery contains meaningful information related to ALD variability. The strongest spectral correlations reached approximately $|r| = 0.60$, while the optimized Random Forest model achieved a Pearson correlation coefficient of 0.801, a mean cross-validation R^2 of 0.592, and a global R^2 of 0.641. The inclusion of DEM information further improved predictive performance. In addition, a recurrent importance of the 512 nm wavelength was identified across multiple independent analyses.

Overall, the results highlight the potential of UAV-based hyperspectral remote sensing as a promising tool for local-scale permafrost monitoring and Active Layer Depth characterization.

Acknowledgments

I would like to express my sincere gratitude to Professor François Jonard for giving me the opportunity to undertake this internship and master's thesis project. I am also grateful for his guidance, valuable advice, and academic support throughout this work.

I would also like to warmly thank Jordan Bates for his continuous supervision, availability, and invaluable assistance throughout the project. His expertise, constructive feedback, and willingness to answer my many questions greatly contributed to both the internship and the successful completion of this thesis.

Declaration on the Use of Artificial Intelligence

This document includes the use of artificial intelligence tools, primarily for language improvement and the rephrasing of certain sections. These tools were used solely as writing assistants and did not generate any data, results, or analyses presented in this thesis.

Contents

Abstract i

Acknowledgments ii

1 Introduction 2

2 Background and State of the Art 4

2.1 Permafrost and Active Layer Depth 4

2.1.1 Definition of Permafrost 4

2.1.2 Active Layer Depth 6

2.2 Existing Methods for Active Layer Depth Measurement 8

2.2.1 CALM Network 8

2.2.2 In-situ Measurement Techniques 8

2.2.3 Limitations of Traditional Methods 10

2.3 Remote Sensing for Permafrost Studies 11

2.3.1 Remote Sensing Principle 11

2.3.2 Satellite Remote Sensing 11

2.3.3 UAV-Based Remote Sensing 13

2.4 Hyperspectral Remote Sensing 14

2.4.1 Principles of Hyperspectral Remote Sensing 14

2.4.2 Advantages and Challenges 16

2.4.3 Applications and Advantages for Environmental Monitoring . . 18

2.4.4 Challenges And Limitations 19

3 Methodology **21**

3.1 Study Area 21

3.2 Dataset Overview and Data Acquisition 25

3.3 Hyperspectral Data Processing Workflow 27

3.3.1 RGB data pre-processing 29

3.3.1.1 Image Alignment 29

3.3.1.2 Ground Control Point Integration 31

3.3.1.3 Point Cloud Generation 31

3.3.1.4 DEM Generation 32

3.3.1.5 Orthomosaic Generation 35

3.3.1.6 IMU-GPS File Generation 37

3.3.2 HSI Preprocessing 38

3.3.2.1 Flightline Extraction 38

3.3.2.2 Reflectance Calibration Target Preparation 39

3.3.3 Geocoding 39

3.3.3.1 Boresight Calibration 40

3.3.3.2 Hyperspectral Georectification 41

3.3.4 Atmospheric Correction 42

3.3.4.1 Atmospheric Correction Principles 42

3.3.5 Output Reflectance Products 43

3.3.6 Post-Processing and Final Mosaic Generation 44

4 Analysis and Results **48**

4.1 Data Preparation 48

4.2 Spectral Correlation Analysis 49

4.2.1 Methodology 49

4.2.2 Comparison of Extraction Approaches 51

4.2.3 Band-Wise Correlation Results 53

4.3 Vegetation Indices Analysis 54

4.3.1 Methodology 54
4.3.2 Spatial Distribution of Vegetation Indices 55
4.3.3 Correlation with ALD 59
4.4 Principal Component Analysis 61
4.4.1 Methodology 61
4.4.2 Variance Explained by Principal Components 63
4.4.3 Analysis of PCA Loadings 65
4.4.4 PCA-Based Band Selection 66

5 Random Forest Modeling **69**

5.1 Methodology 69
5.2 Full Hyperspectral Random Forest Model 72
5.3 Feature Importance and Band Selection 74
5.3.1 Principal Component Analysis 75
5.3.1.1 Random Forest Using Principal Components 75
5.3.1.2 PCA-Guided Band Selection 76
5.3.2 Random Forest Feature Importance 77
5.3.3 Band Selection Performance 79
5.4 Integration of DEM Information 81
5.5 Multispectral versus Hyperspectral Approaches 84
5.6 Comparison with Hyperspectral Reference Study 87
5.7 Model Validation and Robustness Analysis 87
5.7.1 Influence of Band Ordering 88
5.7.2 RFECV 90
5.7.3 Sensitivity Analysis 92
5.7.4 Edge-Effect Analysis 95
5.7.4.1 Spectral Signature Comparison 96
5.7.4.2 Influence of Edge-Effect Observations on Model Performance 100

5.8 Linear Regression Analysis 102

6 Discussion **106**

6.1 Main Findings 106

6.2 Recurrent Importance of the 512 nm Wavelength 107

6.3 Implications for Permafrost Monitoring 108

6.4 Limitations 109

6.5 Future Work 110

6.6 Concluding Remarks 110

7 Conclusion **111**

A Additional Orthomosaics **113**

List of Figures

2.1 Distribution of permafrost in the Northern Hemisphere, showing continuous, discontinuous and sporadic permafrost regions in 2020. Source: [27] 5

2.2 Schematic representation of carbon release processes in the atmosphere due to the growth of the active layer depth leading to a positive feedback loop. Source : [32] 7

2.3 Frost tube used to monitor seasonal freezing and thawing of the active layer. The frozen and unfrozen sections of the tube allow the identification of the thaw depth. Source : [74]. 9

2.4 Examples of satellite platforms commonly used for permafrost and environmental monitoring. 13

2.5 Illustration of a hyperspectral data cube, composed of two spatial dimensions and one spectral dimension. Each pixel contains a full spectral signature across multiple wavelengths. Source : [19] 15

2.6 Comparison between hyperspectral and multispectral spectral sampling. Hyperspectral systems provide continuous spectral information and allow the detection of narrow absorption features related to vegetation pigments, water content, and biophysical properties. Source : [41] . . . 17

3.1 Location of the study area near Eight Mile Lake in Interior Alaska, USA. 22

3.2 RGB orthomosaic of the study area located near Eight Mile Lake, Interior Alaska, USA. The image illustrates the tundra landscape and the spatial extent covered during the UAV acquisition campaign. 23

3.3 Spatial distribution of the Active Layer Depth (ALD) sampling locations in red overlaid on the RGB orthomosaic of the study area. 24

3.4 HAIP Blackbird V2 hyperspectral sensor mounted on the UAV platform used during the acquisition campaign. Source : [29] 26

3.5 Overview of the hyperspectral preprocessing workflow applied in this study. The workflow was adapted from the processing pipeline developed within the EOSystM laboratory for HAIP Blackbird V2 UAV acquisitions. 28

3.6 Sparse point cloud generated during the image alignment stage in Agisoft Metashape. 30

3.7 Comparison of Digital Elevation Models (DEMs) generated from two different UAV acquisitions. Despite variations in acquisition parameters, both DEMs present globally consistent terrain structures and elevation patterns. 33

3.8 Elevation difference map between the LiDAR-derived DEM and the DEM generated from the hyperspectral processing workflow. 34

3.9 Comparison of RGB orthomosaics generated from two different UAV acquisition campaigns. Despite variations in flight parameters, both orthomosaics present globally consistent terrain structures and vegetation patterns. 36

3.10 RGB orthomosaic generated from the snow-covered acquisition campaign. The presence of snow reduced the visibility of stable surface features required for reliable calibration and georectification procedures. 37

3.11 Comparison between two hyperspectral reflectance mosaics generated from different acquisition campaigns. The campaign presenting the highest overall geometric and radiometric consistency was selected for the subsequent analyses. 44

3.12 Final hyperspectral mosaic generated before the post-processing refinement stages. 46

3.13 Final hyperspectral mosaic generated after the post-processing refinement stages. The trimming of flightline borders considerably reduced the visibility of residual edge artifacts. 47

4.1 Comparison of Pearson correlation coefficients obtained for the pixel-based, 2 m buffer, and 5 m buffer datasets across the hyperspectral spectral range. The vertical axis was inverted for visualization purposes in order to facilitate the identification of wavelength regions exhibiting the strongest negative correlations with ALD. 51

4.2 Comparison of Spearman correlation coefficients obtained for the pixel-based, 2 m buffer, and 5 m buffer datasets across the hyperspectral spectral range. The vertical axis was inverted for visualization purposes in order to facilitate the identification of wavelength regions exhibiting the strongest negative correlations with ALD. 52

4.3 NDVI derived from the hyperspectral dataset. 56

4.4 PRI derived from the hyperspectral dataset. 57

4.5 NDVI derived from multispectral imagery 58

4.6 Comparison between NDVI derived from hyperspectral imagery, NDVI derived from multispectral imagery, and the corresponding difference map. 59

4.7 Pearson correlation coefficients between the computed vegetation indices and ALD for the pixel-based, 2 m buffer, and 5 m buffer datasets. 60

4.8 Explained variance ratio of the first principal components. 63

4.9 Cumulative explained variance as a function of the number of principal components. 64

4.10 Loading coefficients of the first five principal components as a function of wavelength. 65

4.11 Band importance derived from the absolute loading sum of PC2–PC5. . 67

5.1 Observed versus predicted ALD values obtained using Random Forest models trained with the complete hyperspectral dataset for the three spatial extraction strategies. 73

5.2 Random Forest feature importance as a function of wavelength for the 2 m buffer dataset. 77

5.3 Comparison between PCA absolute loading sum and the top20 most important RF bands. 78

5.4 Evolution of model performance as a function of the number of selected bands. 80

5.5 Random Forest feature importance obtained using hyperspectral bands and DEM information. 82

5.6 Evolution of model performance as a function of the number of selected hyperspectral and DEM features. 83

5.7 Feature importance obtained using the multispectral dataset. 85

5.8 Feature importance obtained using the multispectral dataset combined with DEM information. 86

5.9 Spectral signatures of all selected locations used in the edge-effect analysis. 96

5.10 Spectral signatures for the three investigated edge-effect zones. Each zone contains one edge-effect location and two neighboring reference locations. 97

5.11 Example of wavelength-dependent relative spectral differences observed in Zone 3. 99

5.12 Standardized regression coefficients obtained for the linear regression model using the seven most important spectral bands selected by the Random Forest feature selection procedure. Variables are ranked according to the absolute value of their coefficients. 103

5.13 Standardized regression coefficients obtained for the linear regression model using the optimized feature set including DEM information. Variables are ranked according to the absolute value of their coefficients. . . 104

A.1 RGB orthomosaic generated from Campaign 3. 113

A.2 RGB orthomosaic generated from Campaign 5. 114

A.3 RGB orthomosaic generated from Campaign 6. 114

List of Tables

3.1 Overview of the hyperspectral acquisition campaigns. 27

4.1 Highest Pearson and Spearman correlation coefficients obtained for the buffer-based datasets. 53

5.1 Baseline Random Forest performance obtained using all hyperspectral bands for the three spatial extraction strategies. 73

5.2 Random Forest performance obtained using PCA components as input variables. 75

5.3 Random Forest performance obtained using wavelengths selected from PCA loadings. 76

5.4 Random Forest performance for selected feature subset sizes. 81

5.5 Comparison between the optimal hyperspectral model and the optimal hyperspectral + DEM model. 83

5.6 Comparison between multispectral and hyperspectral Random Forest models. 84

5.7 Comparison between the results obtained in this study and those reported in the reference hyperspectral study. 87

5.8 Influence of hyperspectral band ordering on model performance. 89

5.9 Most important predictors identified using the original and reversed band ordering. 89

5.10 Predictors selected by RFECV. 91

5.11 Comparison between the RF feature importance approach and RFECV. 91

5.12 Sensitivity analysis results obtained using different random states for the cross-validation procedure. 93

5.13 Frequency of selection of the best performing wavelengths across the ten tested random states. 94

5.14 Average model performance across all tested random states. 94

5.15 Mean absolute spectral differences between edge-effect and reference locations. 98

5.16 Comparison of the optimized Random Forest model before and after removing the identified edge-effect observations. Results correspond to the average values obtained across ten different cross-validation random states. 100

5.17 Influence of edge-effect removal on Mean CV R^2. 101

5.18 Comparison between Linear Regression and Random Forest models. . . 102

Chapter 1

Introduction

Permafrost represents a major component of high-latitude environments and plays a fundamental role in the global climate system. Defined as ground that remains at or below 0°C for at least two consecutive years, permafrost stores large quantities of organic carbon accumulated over thousands of years. As Arctic regions experience accelerated warming, permafrost degradation has become an increasing concern due to its potential impacts on hydrology, ecosystem dynamics, infrastructure stability, and greenhouse gas emissions. Among the different indicators used to monitor permafrost evolution, Active Layer Depth (ALD) is particularly important because it directly reflects the seasonal thawing processes occurring above the frozen ground.

Traditional ALD monitoring mainly relies on in-situ measurements such as mechanical probing, frost tubes, and borehole temperature observations. While these approaches provide accurate local measurements, they remain labor-intensive and often fail to adequately capture the strong spatial variability that characterizes permafrost environments. Remote sensing has therefore emerged as a valuable complementary tool, offering the possibility to investigate large areas and identify environmental variables potentially linked to thaw dynamics.

Recent developments in unmanned aerial vehicle (UAV) technology have considerably expanded the capabilities of remote sensing for environmental monitoring. In particular, hyperspectral sensors provide detailed spectral information through hundreds of narrow and contiguous wavelength bands, enabling a refined characterization of vegetation, soil properties, moisture conditions, and other surface characteristics. Because Active Layer Depth cannot be directly observed from remote sensing data, hyperspectral imagery offers the potential to identify indirect spectral indicators associated with permafrost processes.

The objective of this thesis is to investigate the potential of UAV-based hyperspectral

remote sensing for the characterization of Active Layer Depth in Arctic tundra environments. A complete hyperspectral processing workflow was developed to transform raw UAV acquisitions into georeferenced reflectance products suitable for analysis. Several complementary approaches were then applied, including spectral correlation analysis, vegetation indices, Principal Component Analysis (PCA), and Random Forest machine learning models. Particular attention was devoted to feature selection, model robustness, and the identification of spectral regions most strongly associated with ALD variability.

The study aims not only to evaluate the predictive capability of hyperspectral data for ALD estimation, but also to improve the understanding of the spectral information contributing to these predictions. Ultimately, this work seeks to assess the relevance of UAV hyperspectral imagery as a tool for local-scale permafrost monitoring and to identify promising directions for future research in Arctic environments.

Chapter 2

Background and State of the Art

2.1 Permafrost and Active Layer Depth

2.1.1 Definition of Permafrost

The goal of this thesis is to analyze permafrost within a certain region. Even though the study area and methodology will be discussed later, a first big step is to have a clear context of what is going to be studied and what it represents.

Permafrost refers to the ground being at a temperature of 0°C or below for a period of at least 2 consecutive years. Its name can be misleading as the term "frost" might suggest the necessity of a presence of ice, however the ice content doesn't matter, as some permafrost can be ice-free. [34] The composition of the ground varies, it can consist of soil, sediments or rocks. Geographically, permafrost is mostly found in high latitudes regions of the Northern Hemisphere including areas such as Alaska, Canada, Siberia as illustrated in 2.1.

Its spatial distribution is mostly controlled by climate conditions, but some local factors such as vegetation, soils' physical and thermal properties have an important impact as well [17].

Permafrost plays a crucial role in the Earth's climate evolution. In fact, it stores large quantities of organic carbon. In the context of climate change, a rise of the temperature can lead to a destabilization of this frozen carbon inducing a release of greenhouse gases into the atmosphere. This release can then accelerate the climate change even more creating a positive feedback loop [68].

Given its importance in the climate system, characterizing its spatial distribution is crucial. As shown on 2.1, permafrost is not uniformly distributed and presents some

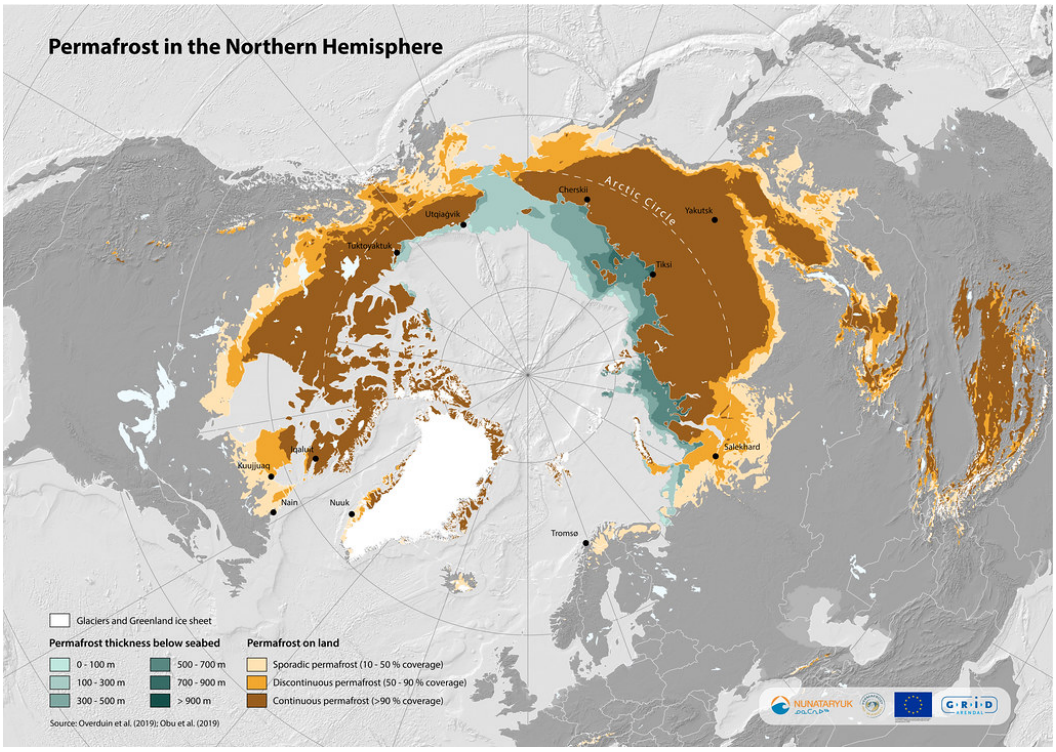


Figure 2.1: Distribution of permafrost in the Northern Hemisphere, showing continuous, discontinuous and sporadic permafrost regions in 2020. Source: [27]

variability depending on the environmental conditions.

Permafrost is classified in three different zones based on the proportion of ground that remains permanently frozen in a given area [46] :

- **Continuous permafrost:** Permafrost occupies more than 90% of the ground surface. It is typically found in the coldest regions and is relatively stable over large areas.
- **Discontinuous permafrost:** Permafrost covers between 50% and 90% of the ground. It is more fragmented and its presence depends more strongly on local environmental conditions.
- **Sporadic permafrost:** Permafrost is present in less than 50% of the area and occurs in isolated patches, mainly controlled by local factors such as vegetation and soil properties [24].

Furthermore, at smaller spatial scales, the presence and variability of the permafrost is strongly influenced by local factors such as vegetation, soil composition, moisture content impacting the thermal regime of the ground. Also, snow cover can act as an insulator and can reduce heat losses.

Despite this classification, permafrost cannot be considered as a static system. In fact, the uppermost layer undergoes yearly temperature variations due to seasonal thawing during the summer and refreezing during the winter. Permafrost is then considered as a dynamic system [35].

2.1.2 Active Layer Depth

This particular layer which is subject to seasonal thawing and refreezing is referred to as : Active Layer. It is located at the interface between the atmosphere and the underlying permafrost [34]. Consequently, its depth varies along the year with a maximum at the end of the thawing season. And this maximum depth is called : Active Layer Depth (ALD) .

Thus, the active layer depth is a key component for permafrost studies as it links the outside atmosphere and the frozen ground through energy exchanges. One of the primary roles of the active layer is its influence on heat transfer processes. In fact, during the thawing season, heat from the atmosphere penetrates the ground which increases the depth of the active layer. This determines how much thermal energy is transferred to the permafrost which then impact its stability. As a result, variations in ALD is a possible indicator of changes in the thermal state of the atmosphere thus of permafrost and can be used to point out climate changes impacts in the Arctic regions [35] [46].

In addition to thermal processes, the active layer influences hydrological dynamics as well. In fact, after thawing, soil becomes permeable, water can then infiltrate and circulate within the upper layers of the ground. Consequently, changes in the soil moisture can happen and the formation of wetlands may take place. ALD is then also able to modify local hydrology and landscape evolution [46].

The active layer also plays a role in biogeochemical processes, particularly as mentioned earlier in relation to carbon cycle. In fact, organic matter is stored in the soil and can become active when thawed leading to a release of greenhouse gases such as carbon dioxide (CO_2) and methane (CH_4) contributing to a feedback mechanism as illustrated in 2.2 where an increase of the surface temperature leads to a growth of the active layer. The thawing can then activate and release organic matter in the atmosphere. Those greenhouse gases can then increase the surface temperature which in return can increase the active layer depth. As a conclusion, an increase in ALD may enhance larger carbon emissions, amplifying the global warming [71] [69].

Since they are obviously linked, similarly to permafrost, active layer depth is controlled by environmental factors. The main driver is air temperature as higher temperatures

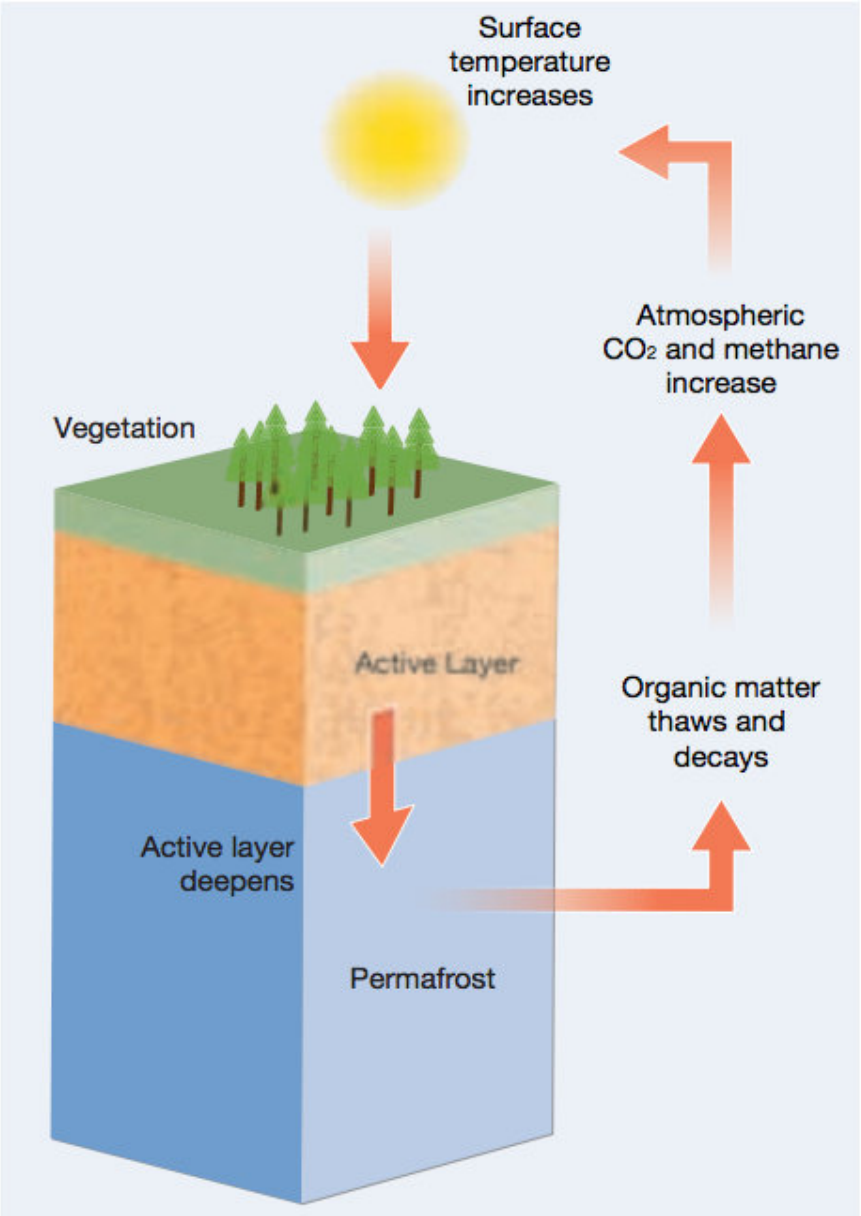


Figure 2.2: Schematic representation of carbon release processes in the atmosphere due to the growth of the active layer depth leading to a positive feedback loop. Source : [32]

lead to a deeper active layer. Then, soil moisture and composition, thermal conductivity affect the heat transfer rate as well. Vegetation cover also has an impact on ALD as it can act as a protective layer reducing solar radiation on the ground. As a result, the active layer depth can vary significantly over short distances [46].

Given this strong variability, accurately characterizing the active layer depth can be challenging.

2.2 Existing Methods for Active Layer Depth Measurement

As discussed above, active layer depth is a major parameter to understand the permafrost dynamics. Accurate measurements are then mandatory to provide a monitoring of permafrost evolution and assessing the impact of climate change. Traditionally, ALD has been measured using in-situ techniques, allowing a direct ground observations at specific locations. However, due to spatial variability of permafrost systems, those measurements need to be done systematically [22].

2.2.1 CALM Network

To address this need, several international monitoring programs have been established. Among those, the Circumpolar Active Layer Monitoring (CALM) network is one of the most widely used. The CALM program was established to provide standardized and long-term observations of active layer thickness, mainly across Arctic and sub-Arctic regions.

It consists of a network of monitoring sites distributed across permafrost areas, where systematic measurements are carried out following protocols.

At each site, the active layer depth is typically measured using mechanical probing at multiple points arranged in predefined grids as it will be explained right after.

In addition to spatial measurements, repeated observations over time enable the analysis of temporal changes in active layer thickness and permafrost dynamics [13].

2.2.2 In-situ Measurement Techniques

There are several different in-situ measurements techniques used to determine the active layer depth.

The most widely used technique is mechanical probing. This method is conceptually pretty simple, it consists in putting a thin and rigid metal rod vertically into the ground until it reaches the frozen layer, preventing further penetration. And the depth at which the metal rod is stopped, is interpreted as the bottom of the active layer. Typically, those measurements are made on a grid of sampling points. The nodes are evenly distributed (continuous spacing of 1,10 or 100 meters depending on the site) [12].

Another method is ground temperature measurements. This method is mostly used in mountain regions or areas where mechanical probing is not feasible. It consists of an array of temperature sensors installed vertically in boreholes, extending from the ground surface downward through the active layer and into the permafrost. These measurements can be recorded continuously, providing information on the seasonal evolution of ground temperatures. By analyzing temperature variations, it is possible to determine the depth at which the ground remains frozen throughout the year, and thus estimate the maximum thaw depth [9].

A third technique involves frost/thaw tubes as shown in 2.3. Frost tubes consist of a tube filled with liquid that freezes when temperatures drop below 0°C. They provide information about seasonal progression of thaw and maximum seasonal thaw. By observing the frozen and unfrozen part of the tube, it's possible to identify the position of the thaw or freezing point at the installation point [23].

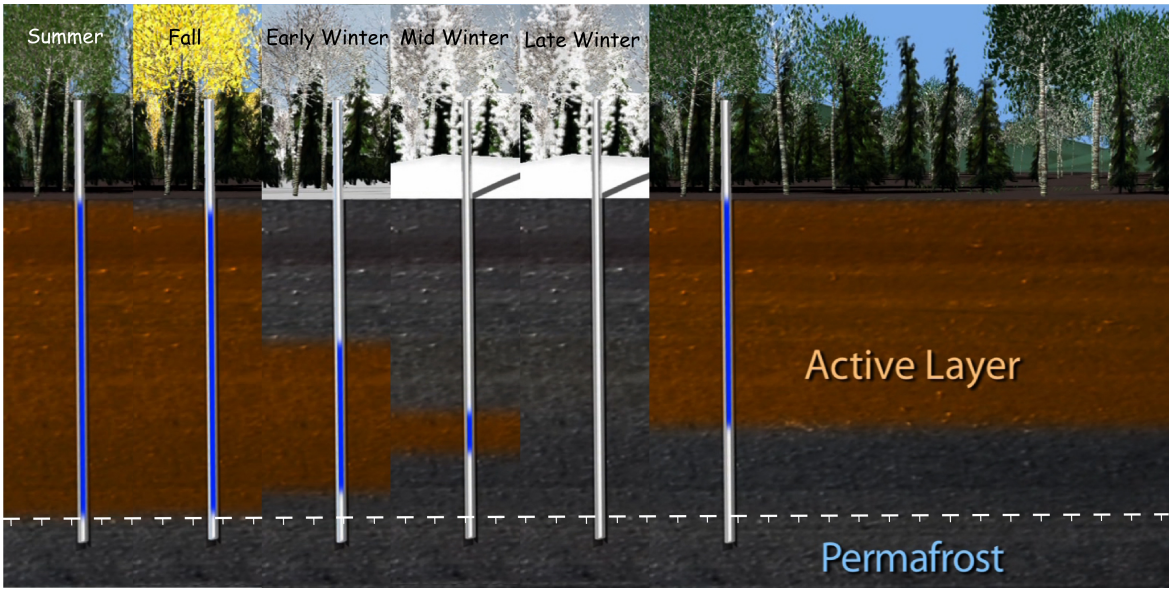


Figure 2.3: Frost tube used to monitor seasonal freezing and thawing of the active layer. The frozen and unfrozen sections of the tube allow the identification of the thaw depth. Source : [74].

Together, these techniques provide complementary information about the active layer.

In-situ measurement techniques provide direct and reliable observations of Active Layer Depth, making them essential for permafrost studies. Because these methods are based on physical measurements of the ground, they offer a high level of accuracy (cm) at specific locations.

One of the best advantages is that they rely on actual measurements rather than using indirect estimations or models that can reveal themselves inaccurate and lead to wrong estimations. Mechanical probing allows rapid and direct measurements during field campaigns.

In addition to that, temperature measurements provide continuous data over time which is valuable to capture seasonal evolution.

Finally, in-situ measurements can also be useful to validate numerical models and remote sensing approaches [23] [13].

2.2.3 Limitations of Traditional Methods

Despite their accuracy, in-situ measurement techniques present several significant limitations, particularly when applied at large spatial scales.

One of the main limitation is its restricted spatial coverage. In fact, measurements are made at discrete locations which can't show the spatial variability of permafrost across a whole region. This is a critical point since as mentioned earlier, permafrost varies due to soil moisture, vegetation, soil composition...

In addition to that, in-situ measurements require human effort due to the repetition of the measurements needed across the years to conduct those manual experiments. Also, boreholes, made for ground temperature measurements, can weaken the ground and impact thermal conditions.

Also, as permafrost regions are often located in remote and harsh environments, some regions are complicated to reach therefore logistic issues may appear.

Another important limitation is that most in-situ methods provide point-based observations. Techniques such as frost tubes and ground temperature measurements offer detailed information at specific locations but do not adequately represent spatial heterogeneity at larger scales.

Furthermore, the installation and maintenance of monitoring systems, such as boreholes or frost tubes, require specialized equipment which can further limit their applicability.

As a consequence, relying solely on in-situ measurements can be difficult to get large

and extensive ALD information [13].

To overcome these limitations, remote sensing techniques have been increasingly used to provide spatially continuous observations of permafrost dynamics.

2.3 Remote Sensing for Permafrost Studies

2.3.1 Remote Sensing Principle

To overcome these limitations, remote sensing techniques have been increasingly used to provide spatially continuous observations of permafrost dynamics. While field measurements provide accurate and direct observations, their limited spatial coverage makes them improvable [45].

Remote sensing is the acquisition of information about the Earth's surface without direct physical contact, typically through sensors mounted on satellites or airborne platforms. These sensors record variations in electromagnetic signals reflected or emitted by the surface, which can be used to infer physical and environmental properties [41].

Focusing on permafrost research, remote sensing provides indirect observations of surface characteristics such as vegetation cover, soil moisture, and land surface temperature... These variables can be used to analyze permafrost dynamics and estimate parameters such as Active Layer Depth.

One of the main advantages of remote sensing is its ability to provide spatially continuous data over large and possibly inaccessible regions which makes it suitable for studying Arctic environments, where field measurements may be tough to conduct. In addition to that, repeated observations is easier to organize, therefore allowing the tracking of temporal changes. As a reminder, monitoring temporal changes is primordial to keep track of the impacts of climate change on permafrost systems.

Two main categories of remote sensing techniques can be distinguished: satellite remote sensing and airborne remote sensing [41].

2.3.2 Satellite Remote Sensing

Satellite remote sensing has been used as a useful way to monitor permafrost at regional and global scales. From the growing amount of studies related to permafrost observations, its importance is increasing for large scale observations. As showed in

recent studies, satellite observations allow to identify and monitor permafrost related features over long periods and vast Arctic regions [59].

As said earlier, permafrost is a subsurface feature, so observing it from space might seem counterproductive. In fact, remote sensing methods rely on the analysis of surface characteristics that are related to permafrost conditions. Those characteristics include vegetation cover, land surface temperature, soil moisture, water distribution... Based on those variables, remote sensing can infer the presence and state of permafrost [45].

To capture those environmental variables, a variety of satellite sensors can be used. Sensors such as optical, thermal, microwave or multispectral are used.

Optical sensors provide observations of surface reflectance and enable the analysis of vegetation dynamics over several years. Thermal infrared sensors are used to estimate land surface temperature, which is used to control the thermal regime of the ground. Microwave sensors, and particularly Synthetic Aperture Radar (SAR), can provide additional information on soil moisture and surface deformation and have a great advantage of being usable even with cloudy weather.

Based on recent studies, the common methodology is to combine the different satellite datasets to improve the permafrost monitoring. Combining optical, thermal and radar observations allow for a better understanding and comprehension of the relations between surface conditions and subsurface processes [45].

Among all Earth observations satellites, several satellite missions are particularly important for permafrost studies. Landsat (2.4a) provides one of the longest continuous Earth observation records, with data available since the 1970s, making it highly valuable for long-term environmental monitoring. Also, the Sentinel missions developed by the European Space Agency (ESA) have significantly improved data availability and quality. Sentinel-2 (2.4b) offers optical imagery, while Sentinel-1 provides SAR data that can be used to monitor ground deformation and freeze–thaw processes [20].



(a) Landsat 8 satellite, providing long-term optical Earth observation data. Source : [55]



(b) Sentinel-2 satellite from ESA, offering high-resolution optical imagery with frequent revisit time.Source : [14]

Figure 2.4: Examples of satellite platforms commonly used for permafrost and environmental monitoring.

Despite these advantages, satellite remote sensing also presents important limitations. One of the main challenges is the spatial resolution of satellite data, which is often insufficient to capture the very small scale features of Active Layer Depth [45].

In addition to that, optical and thermal satellite data are affected by atmospheric conditions such as cloud cover, low solar illumination, and polar night, which can significantly reduce data availability in Arctic regions [41].

Overall, satellite remote sensing is a very useful method but its drawbacks highlight the need of complementary approaches.

2.3.3 UAV-Based Remote Sensing

An alternative to satellite remote sensing is UAV-based remote sensing. It is emerging and is a good middle ground between satellite and in-situ measurements, providing high resolution data over targeted areas.

One of the main advantages of UAVs is their ability to operate at low altitude, which allows the acquisition of imagery at better spatial resolution than satellites. This makes a good point for permafrost studies, where surface features and active layer processes may vary significantly over short distances. Recent UAV studies have successfully monitored land surface changes associated with permafrost thaw [82] [83].

Another argument in favor of UAVs is their flexibility. Indeed, they can be deployed on demand, repeated over short time intervals. Compared with manned airborne surveys, UAVs are generally less expensive, safer, and easier to operate in targeted field campaigns. They can also carry different lightweight sensors depending on the

scientific objective, including RGB, multispectral, hyperspectral, thermal, LiDAR, and atmospheric sensors [51] [84].

However, UAV remote sensing also has limitations. Its spatial coverage is much smaller than satellite observations, making it less suitable for large surface observations. UAV operations are also constrained by battery life, flight regulations, weather conditions, wind, visibility, and accessibility of field sites. In Arctic environments, these constraints can be particularly important.

Overall, UAV remote sensing provides a great approach for permafrost studies. It does not replace satellite monitoring, but complements it by providing very high-resolution observations over selected areas. This makes UAVs particularly relevant for studying local variability and for validating or improving satellite-based products. In the context of this thesis, UAV data are especially useful because they allow detailed analysis of surface properties potentially linked to Active Layer Depth [51].

2.4 Hyperspectral Remote Sensing

2.4.1 Principles of Hyperspectral Remote Sensing

Hyperspectral remote sensing, also referred to as imaging spectroscopy, consists in acquiring detailed spectral information from Earth surface materials through a large number of narrow and contiguous spectral bands. Unlike more conventional multispectral systems, hyperspectral sensors measure the reflected or emitted radiation continuously across the whole electromagnetic spectrum, allowing a much finer characterization of surface properties. According to the Remote Sensing course, "Imaging spectroscopy refers to airborne, spaceborne, or UAV imaging spectrometers capable of measuring solar radiation reflected by Earth surface materials in many contiguous wavebands" [41].

The principle of hyperspectral remote sensing is based on spectroscopy, which studies the interaction between matter and electromagnetic radiation. Different materials interact differently with incoming radiation depending on their physical and chemical properties. As a result, each material presents a specific spectral response, commonly referred to as a spectral signature. These spectral signatures can then be used to identify or characterize vegetation, soil, water, minerals, or other surface materials [41].

A hyperspectral image is generally represented as a three-dimensional data cube composed of two spatial dimensions and one spectral dimension as illustrated in 2.5.

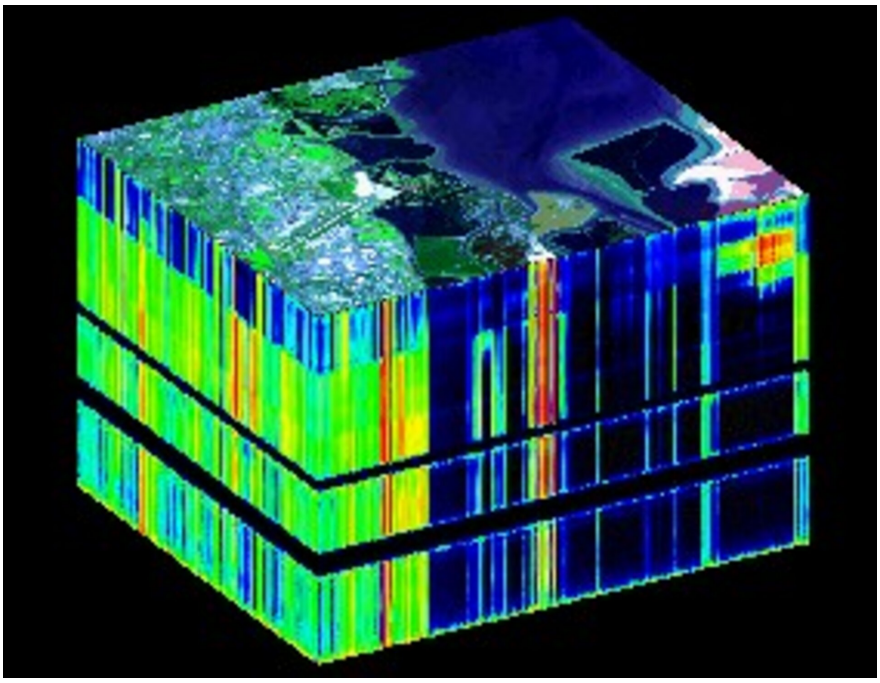


Figure 2.5: Illustration of a hyperspectral data cube, composed of two spatial dimensions and one spectral dimension. Each pixel contains a full spectral signature across multiple wavelengths. Source : [19]

For each pixel of the image, a complete reflectance spectrum is available over a large wavelength range. This additional spectral dimension provides significantly more information than conventional multispectral imagery and allows the detection of subtle spectral variations that may not be visible using broad multispectral bands [41] [11].

In fact, hyperspectral imagery allows the characterization of land surfaces with greater detail than multispectral systems because the large number of narrow spectral bands can directly describe important absorption and reflectance features. These absorption features are particularly important for environmental studies because they are related to biochemical and biophysical properties of surface materials [41].

Hyperspectral systems have been developed for more than three decades and have been deployed on airborne, UAV, and spaceborne platforms. Several airborne sensors such as AVIRIS, HyMap, APEX, or HySpex have been widely used for environmental and ecosystem studies. More recently, new generations of spaceborne hyperspectral missions such as PRISMA and EnMAP have considerably expanded the availability of hyperspectral data for Earth observation applications.

2.4.2 Advantages and Challenges

Although multispectral and hyperspectral remote sensing are both based on the analysis of electromagnetic radiation reflected or emitted by Earth surface materials, the type and amount of information retrieved from these systems differ considerably. Multispectral imagery generally relies on a limited number of broad spectral bands designed to capture major surface characteristics, whereas hyperspectral systems provide much denser spectral sampling across the electromagnetic spectrum [41] [50].

This difference in spectral resolution has important implications for environmental analysis. Broad multispectral bands are often sufficient to identify large-scale patterns such as vegetation distribution, water bodies, or general land cover classes. However, they may not adequately capture subtle spectral variations associated with biochemical or biophysical properties of surface materials. As a result, different materials can sometimes exhibit similar responses within broad multispectral bands, limiting their separability [50].

Hyperspectral imagery addresses this limitation by capturing narrow absorption and reflectance features linked to the composition and physical properties of materials. These spectral features are particularly important because they are directly related to variables such as chlorophyll concentration, pigment composition, moisture content, mineralogy, or vegetation stress. Previous studies have shown that hyperspectral observations can therefore provide more detailed information on ecosystem properties than conventional multispectral imagery [50].

The richer spectral content of hyperspectral data also improves material discrimination capabilities. Surface materials that may appear spectrally similar in multispectral imagery can often be separated using hyperspectral observations because small variations in reflectance become detectable at narrow wavelength intervals. This increased sensitivity is especially relevant for environmental applications involving gradual or subtle surface changes [50] [62].

To illustrate the differences between multispectral and hyperspectral imaging, Figure 2.6 presents the spectral sampling characteristics of both systems. Multispectral sensors only measure reflectance within a limited number of broad wavelength intervals, whereas hyperspectral systems acquire continuous spectral information through hundreds of narrow contiguous bands. This denser spectral sampling allows the detection of subtle absorption and reflectance features associated with surface material properties [30].

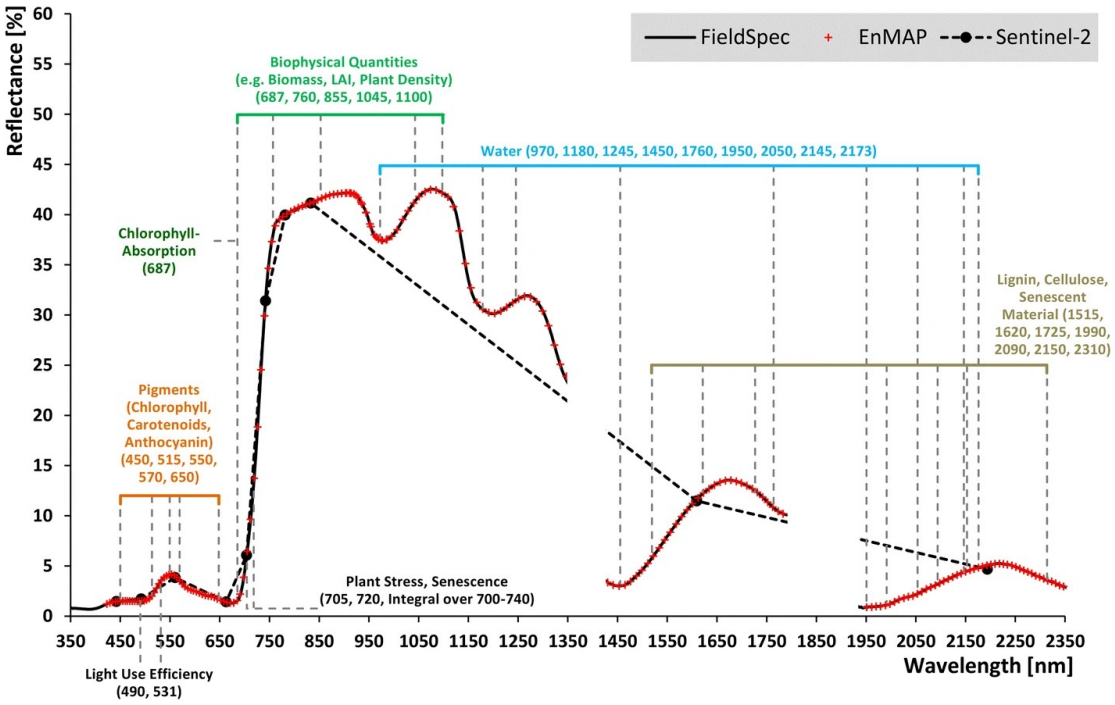


Figure 2.6: Comparison between hyperspectral and multispectral spectral sampling. Hyperspectral systems provide continuous spectral information and allow the detection of narrow absorption features related to vegetation pigments, water content, and biophysical properties. Source : [41]

This additional spectral information explains the growing interest in hyperspectral remote sensing for environmental and ecosystem monitoring applications.

In the context of permafrost studies, these capabilities are particularly valuable because Active Layer Depth cannot be directly observed from remote sensing data. Instead, remote sensing approaches rely on indirect surface indicators such as vegetation condition, soil moisture, or surface composition. Since these variables may present subtle spectral differences, hyperspectral imagery potentially offers improved sensitivity for detecting environmental variations linked to permafrost dynamics [45].

However, the increased spectral richness of hyperspectral imagery also introduces important analytical challenges. Neighboring spectral bands are often highly correlated, resulting in strong spectral redundancy. In addition, hyperspectral datasets are generally characterized by very large data volumes and increased sensitivity to noise. These characteristics complicate data analysis and frequently require advanced preprocessing techniques [41].

Another major challenge associated with hyperspectral imagery is the so-called "curse of dimensionality." As the number of spectral bands increases, the complexity of data analysis also grows significantly, potentially reducing model robustness and increasing computational cost. Consequently, dimensionality reduction approaches such as Prin-

cipal Component Analysis (PCA), feature extraction, or band selection techniques are commonly applied before performing statistical or machine learning analyses.

Therefore, the choice between multispectral and hyperspectral imagery should not simply be considered as a trade-off between low and high spectral resolution. Instead, both approaches provide complementary capabilities depending on the objectives and scale of the study. Multispectral systems remain highly efficient for operational large-scale monitoring, while hyperspectral observations provide more detailed spectral information for advanced environmental characterization.

2.4.3 Applications and Advantages for Environmental Monitoring

One of the major strengths of hyperspectral remote sensing lies in its ability to retrieve detailed biochemical and biophysical information from surface materials. Because hyperspectral sensors capture narrow spectral features associated with specific absorption processes, they enable the estimation of environmental variables that are difficult to assess using conventional multispectral observations.

In vegetation studies, hyperspectral imagery has been widely used to estimate parameters related to plant physiology and ecosystem functioning. Several spectral regions are strongly associated with chlorophyll absorption, pigment composition, and vegetation structure [61] [42]. As highlighted in the course material by François Jonard, specific wavelength regions can be related to chlorophyll content, carotenoids, anthocyanins, biomass, leaf area index, and plant density. These variables are particularly relevant for environmental monitoring because they provide information on vegetation health and stress conditions [41].

Hyperspectral observations are also highly sensitive to water content and moisture conditions. Water absorption features occurring in the near-infrared and shortwave infrared regions are commonly used to estimate vegetation water content and soil moisture. Since moisture plays a major role in thermal and hydrological processes, this capability is particularly important for Arctic and permafrost environments.[41].

Another important application of hyperspectral remote sensing concerns the characterization of soil and surface composition. Hyperspectral data can provide information on mineralogy, organic matter, and surface material properties through the analysis of diagnostic absorption features. This level of spectral detail allows a more refined characterization of surface heterogeneity than conventional broadband observations [61].

Beyond the retrieval of individual variables, hyperspectral imagery is particularly valuable for detecting gradual or subtle environmental changes. Small variations in vegetation condition, moisture distribution, or surface composition may induce measurable spectral changes before visible modifications occur at larger scale. This sensitivity explains the growing interest in hyperspectral approaches for ecosystem monitoring and climate-related applications [26].

In permafrost studies, these capabilities are especially relevant because many environmental variables influenced by Active Layer Depth can potentially affect spectral reflectance. Variations in soil moisture, vegetation composition, plant stress, and surface hydrology are closely linked to thaw dynamics and ground thermal conditions. Although Active Layer Depth itself cannot be directly measured from hyperspectral imagery, the analysis of these indirect surface indicators may improve the characterization of permafrost-related processes.

Hyperspectral imagery is therefore increasingly considered a promising tool for environmental and ecosystem monitoring, particularly when fine-scale spatial variability and subtle surface changes must be analyzed. Combined with UAV platforms, hyperspectral sensors offer the possibility to acquire high-resolution spatial and spectral information, making them particularly suitable for local-scale studies in heterogeneous Arctic environments.

2.4.4 Challenges And Limitations

Despite its strong potential for environmental monitoring, hyperspectral remote sensing also presents several important challenges related to data acquisition, preprocessing, and analysis. The large amount of spectral information provided by hyperspectral sensors considerably increases the complexity of data processing compared with conventional multispectral imagery.

One of the main limitations of hyperspectral imagery is the very high dimensionality of the data. Hyperspectral datasets commonly contain hundreds of spectral bands, resulting in extremely large data volumes. While this spectral richness provides detailed information about surface materials, it also increases storage requirements, computational cost, and processing time [41].

Another important issue concerns spectral redundancy. Because neighboring hyperspectral bands are often highly correlated, a significant amount of information may be repeated across the spectrum. This redundancy can complicate statistical analysis and reduce the efficiency of predictive models if all spectral bands are used directly [53] [6].

Hyperspectral imagery is also highly sensitive to noise and atmospheric effects. Certain wavelength regions may be strongly affected by atmospheric absorption, sensor instability, or illumination variability, potentially degrading data quality. Consequently, hyperspectral datasets generally require extensive preprocessing steps before analysis, including radiometric calibration, atmospheric correction, noise reduction, and geometric correction [25].

The high dimensionality of hyperspectral data also leads to the so-called "curse of dimensionality." As the number of spectral variables increases, the complexity of the feature space grows significantly, which may reduce model robustness and increase the risk of overfitting. This issue is particularly important when the number of observations remains limited compared with the number of spectral bands.

To address these challenges, dimensionality reduction and feature extraction techniques are commonly applied prior to statistical analysis or machine learning modeling. Principal Component Analysis (PCA), band selection approaches, and feature extraction methods are frequently used to reduce redundancy while preserving the most relevant spectral information. In addition, machine learning algorithms are increasingly employed to exploit the complexity of hyperspectral datasets and identify non-linear relationships between spectral features and environmental variables [44]

Another limitation concerns the operational use of hyperspectral systems. Hyperspectral sensors are generally more expensive and technically demanding than conventional multispectral systems. Data acquisition and processing workflows therefore require significant computational resources and expertise.

Despite these challenges, ongoing developments in sensor technology, data processing, and machine learning continue to improve the applicability of hyperspectral remote sensing for environmental studies.

Chapter 3

Methodology

This chapter presents the methodology developed and applied in this study to pre-process and analyze UAV-based hyperspectral imagery acquired over Arctic tundra environments. The objective of the workflow is to transform the raw hyperspectral acquisitions into analysis-ready products suitable for investigating Active Layer Depth.

The methodology combines pre-processing, image alignment, surface generation, geocoding, atmospheric correction and post-processing. Due to the complexity and high dimensionality of hyperspectral datasets, several preprocessing stages were required before the spectral information could be reliably analyzed.

This chapter introduces the study area and the dataset acquired during the UAV campaign. The complete hyperspectral preprocessing workflow is then described in detail, from raw data to the generation of atmospherically corrected hyperspectral mosaics.

3.1 Study Area

The study area is located near Eight Mile Lake in Interior Alaska, USA, approximately 14-15 km west of the town of Healy and north of the Alaska Range, close to the northern boundary of Denali National Park. The site is situated within the discontinuous permafrost zone at approximately 63°52'42.1"N and 149°15'12.9"W, with an elevation of approximately 690–700 m above sea level [70] [56] [75].



Figure 3.1: Location of the study area near Eight Mile Lake in Interior Alaska, USA.

The study area corresponds to a moist acidic tundra ecosystem characterized by tundra vegetation dominated by tussock-forming sedges, deciduous and evergreen shrubs, mosses, and peat-rich soils [75]. The vegetation mainly consists of *Eriophorum vaginatum* together with shrub species and *Sphagnum* mosses [70]. The site is located on a gently sloping northeast-facing terrain affected by discontinuous permafrost and thermokarst processes [56].

The regional climate is characterized by cold winters and relatively mild summers. Mean annual air temperature in Healy was reported to be approximately $-1.3°C$ between 1976 and 2005, with average monthly temperatures ranging from approximately $-16°C$ in December to $15°C$ in July. Mean annual precipitation is approximately 378 mm, while snow cover generally extends from mid-September to mid-May with an average snow thickness of approximately 52 cm [75].

Soils within the study area are classified as Cryosols according to the WRB soil classification system and Gelisols according to the USDA soil taxonomy. The soils are characterized by an organic layer approximately 45–65 cm thick overlying cryoturbated mineral soils composed of glacial till and windblown loess deposits. Previous studies reported active layer thicknesses ranging approximately between 50 and 120 cm depending on local environmental conditions and permafrost degradation state [75].

The Eight Mile Lake site has been extensively studied over the past decades due to its sensitivity to climate warming and permafrost degradation. Previous investigations documented progressive permafrost warming, thawing processes, thermokarst forma-

tion, and associated hydrological and ecological changes across the site. Permafrost degradation within the study area has resulted in ground subsidence, modifications of near-surface hydrology, and vegetation changes including increasing shrub abundance in areas affected by long-term thaw [70].

The strong spatial variability of vegetation, moisture conditions, thermokarst features, and thaw depth observed across the study area makes the site particularly relevant for hyperspectral remote sensing applications investigating Active Layer Depth (ALD) variability and permafrost-related surface processes.

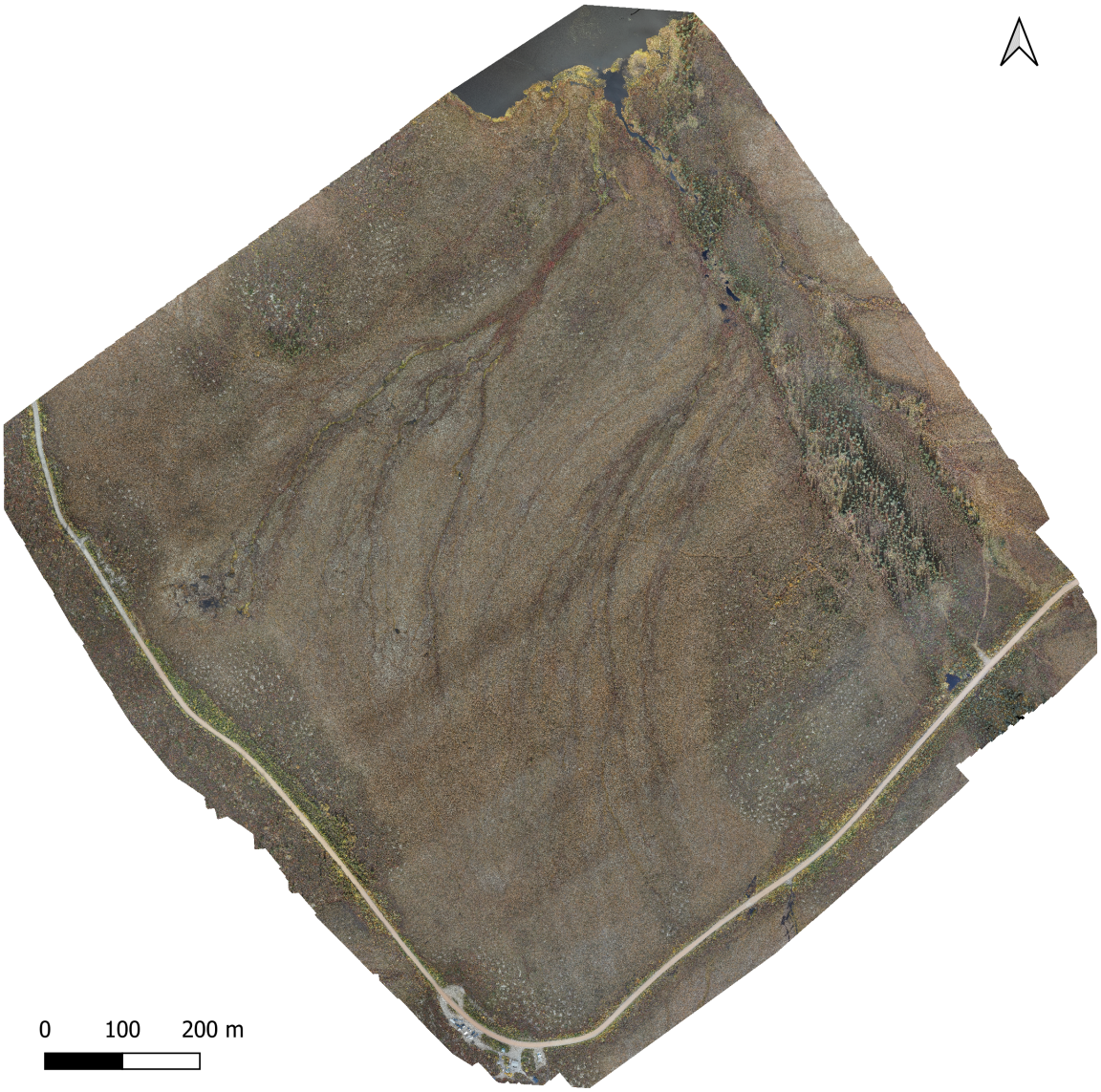


Figure 3.2: RGB orthomosaic of the study area located near Eight Mile Lake, Interior Alaska, USA. The image illustrates the tundra landscape and the spatial extent covered during the UAV acquisition campaign.

Active layer thickness measurements were collected at 126 sampling locations distributed along three transects across the study area. The spatial distribution of the

sampling locations across the study area is presented in Figure 3.3

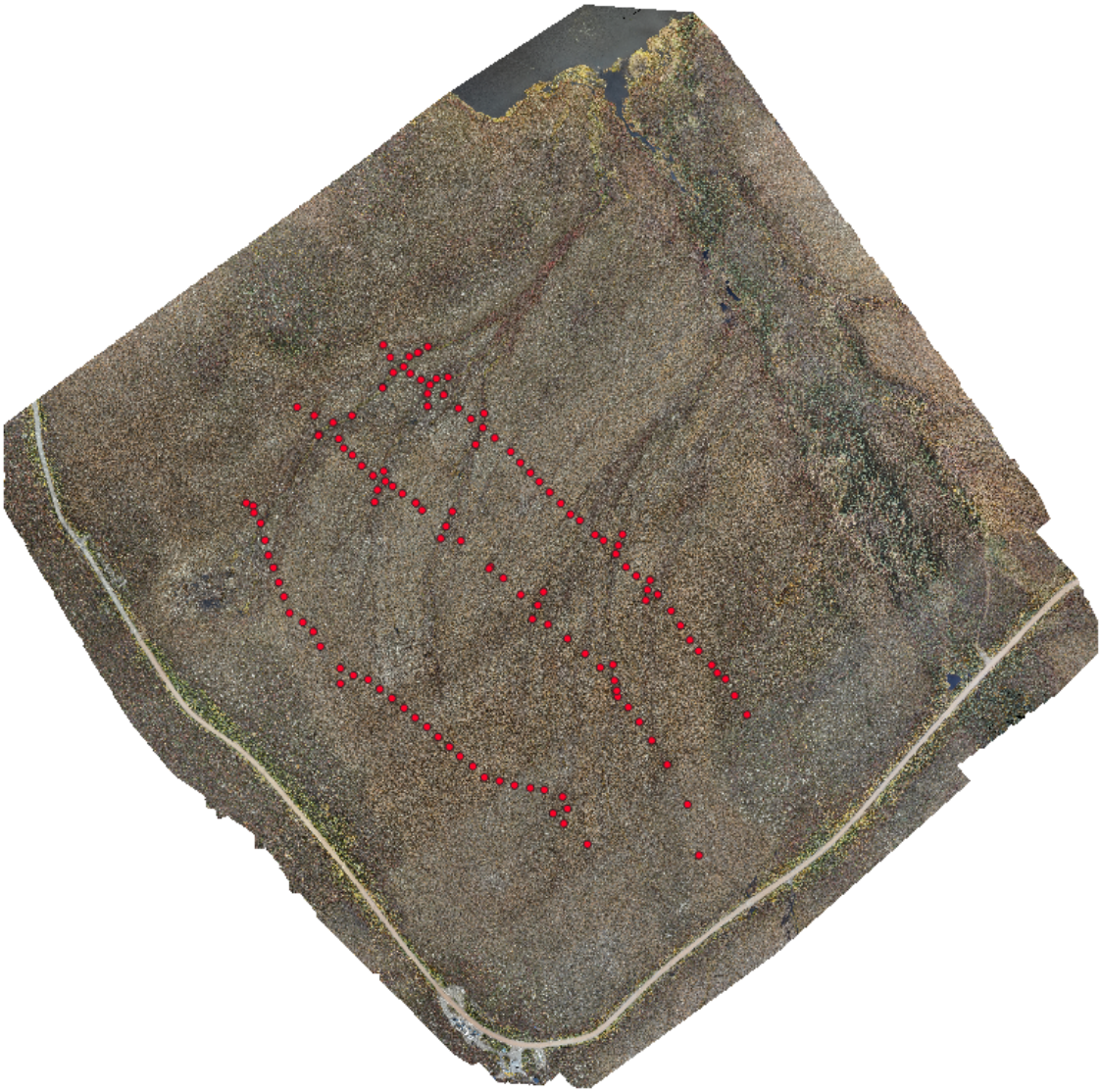


Figure 3.3: Spatial distribution of the Active Layer Depth (ALD) sampling locations in red overlaid on the RGB orthomosaic of the study area.

The measurements were carried out manually using a graduated metal probe inserted vertically into the ground until the frozen layer was reached as discussed in the thaw depth measurement method section.

The sampling strategy was designed to capture the spatial variability of thaw depth across the different surface and vegetation conditions present within the site. For each measurement location, geographic coordinates were recorded using a multi-band RTK GNSS Reach RS2+ rover connected to a Reach RS2+ base station located in Emlid (Budapest, Hungary), providing high-precision positioning information for the subsequent spatial analyses.

3.2 Dataset Overview and Data Acquisition

The hyperspectral dataset used in this study was acquired during a UAV field campaign conducted in Alaska as part of a broader permafrost monitoring initiative carried out by the EOSystM laboratory of the University of Liège. The objective of the campaign was to acquire very high spatial and spectral resolution imagery of Arctic tundra environments in order to investigate environmental surface properties potentially related to Active Layer Depth variability.

A total of six UAV flights were initially available for this study. The acquisitions were performed over several days in September 2025 using a drone platform equipped with the HAIP Blackbird V2 hyperspectral sensor as seen on Figure 3.4. During this campaign, in addition to the hyperspectral data, multispectral and LiDAR data were also collected. This way, the different types of data can be compared or put together to get better results. In parallel with the hyperspectral acquisitions, RGB imagery was also collected to support the photogrammetric reconstruction workflow and the generation of spatial reference products required for hyperspectral georectification.

The HAIP Blackbird V2 sensor records hyperspectral information across 100 spectral bands covering the visible and near-infrared spectral regions. The spectral range extends from approximately 502 nm for the first band to 997 nm for the last band, with a spectral sampling interval of 5 nm between consecutive bands. As a result, each flight generated a substantial amount of raw hyperspectral and RGB data of the same study area presented before, leading to a complex and computationally intensive preprocessing workflow. All hyperspectral acquisitions were performed using comparable flight parameters in order to ensure consistent data quality across the different campaigns. The UAV was operated at an altitude of 120 m above the take-off point and a flight speed of 13.2 m s^{-1}. Adjacent flight lines were planned with a side overlap of 30%.



Figure 3.4: HAIP Blackbird V2 hyperspectral sensor mounted on the UAV platform used during the acquisition campaign. Source : [29]

Initially, the preprocessing workflow was applied to all available flights. However, several limitations progressively emerged during the different preprocessing stages, leading to the exclusion of some datasets throughout the workflow. These limitations were mainly related to acquisition conditions, image quality, and processing feasibility.

For example, one of the flights was characterized by extensive snow cover over the study area. Although the RGB and hyperspectral acquisitions themselves were successfully completed, the presence of large homogeneous snow-covered surfaces complicated the boresight calibration procedure performed later in the workflow. Since the boresight optimization requires the identification of common ground features between the hyperspectral imagery and the RGB orthomosaic, the lack of visible surface structures prevented the reliable collection of corresponding control points. Consequently, this flight was excluded from the subsequent processing stages.

Additional flights were progressively discarded during later preprocessing steps due to differences in data quality, processing consistency, and computational constraints associated with the complete hyperspectral workflow. Because hyperspectral preprocessing involves computationally demanding operations, processing the entirety of the available dataset within the timeframe of this study was not feasible.

As a result, the final analysis focused on the flight providing the most suitable re-

sults. The complete workflow and methodology applied to the raw data is going to be discussed in the next chapter.

Table 3.1: Overview of the hyperspectral acquisition campaigns.

Campaign	Date	Remarks
1	17/09/2025	Flight-line configuration A
2	18/09/2025	Flight-line configuration A
3	19/09/2025	Flight-line configuration A
4	23/09/2025	Flight-line configuration B
5	24/09/2025	Flight-line configuration B; partially cloud affected
6	24/09/2025	Partial coverage; acquired to replace part of Campaign 5

Six hyperspectral acquisition campaigns were available for processing. Two different flight-line configurations were used during the field campaign. Campaigns 1, 2 and 3 were acquired using a first flight-line orientation, while Campaigns 4, 5 and 6 followed a second acquisition pattern characterized by a different flight-line orientation.

In addition, part of Campaign 5 was affected by cloud contamination. Campaign 6 was therefore acquired to replace the affected area and only covered approximately half of the study site rather than the full survey area.

3.3 Hyperspectral Data Processing Workflow

The complete hyperspectral preprocessing workflow applied in this study is summarized in Figure 3.5. The workflow was adapted from the processing pipeline developed within the EOSystM laboratory for HAIP Blackbird V2 UAV acquisitions and includes the procedures required to perform the ALD analysis, or any type of analysis based on hyperspectral data.

Compared with conventional RGB or multispectral imagery, hyperspectral UAV data processing remains particularly complex due to the high dimensionality of the data, the large volume of generated information. In addition, pre-processing workflows are often strongly dependent on the sensor characteristics and software environment, making fully standardized processing approaches difficult to apply across different datasets and platforms.

Throughout the full pre-processing, several different software are going to be used, as they are the one provided in the lab.

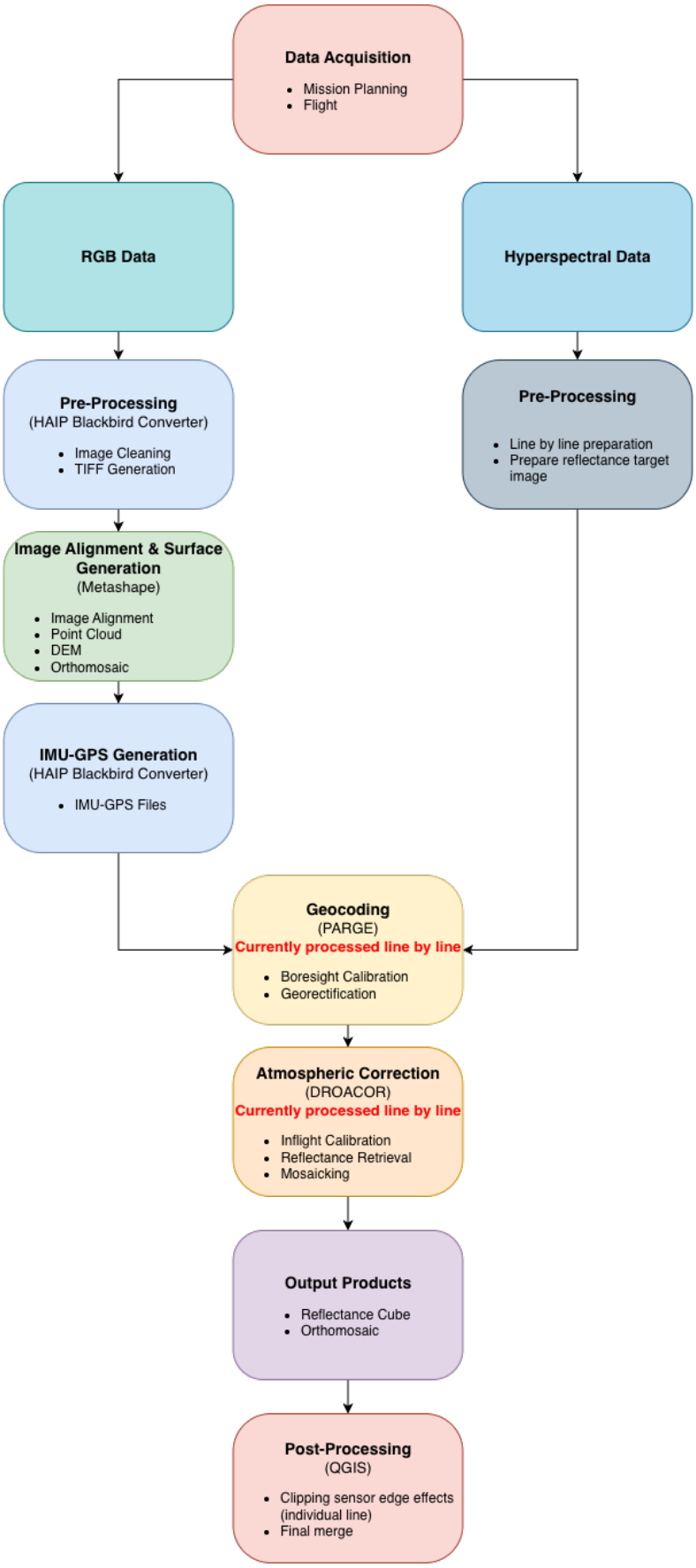


Figure 3.5: Overview of the hyperspectral preprocessing workflow applied in this study. The workflow was adapted from the processing pipeline developed within the EOSystM laboratory for HAIP Blackbird V2 UAV acquisitions.

3.3.1 RGB data pre-processing

The first step of the preprocessing workflow consisted in preparing the RGB imagery acquired during the UAV campaign. The raw RGB data generated by the HAIP Blackbird V2 system were initially processed using the HAIP Blackbird Converter software in order to generate exploitable image products compatible with the rest of the workflow. The HAIP Blackbird Converter is the software dedicated to the HAIP Blackbird sensors, it will be used later in the workflow as well.

During this step, the RGB imagery was converted into TIFF (Tagged Image File Format) format and organized according to the acquisition flights. Indeed, the six flights were processed independently, so it important to keep it that way for the entirety of the workflow to avoid mixing different images from different flights. The TIFF format was selected because of its compatibility with photogrammetric processing software and its ability to preserve image quality without significant compression artifacts [1].

The generated RGB TIFF images were used in Agisoft Metashape for the photogrammetric reconstruction workflow, including image alignment, point cloud generation, and orthomosaic creation.

3.3.1.1 Image Alignment

Following the RGB preprocessing stage, the generated TIFF imagery was imported into Agisoft Metashape software for photogrammetric reconstruction. The first step of this workflow consisted in aligning the RGB images in order to reconstruct the geometry of the full scene. In fact, at this point, the RGB data is only a serie of a few thousands overlapping images of the scene.

The image alignment process implemented in Agisoft Metashape is based on Structure-from-Motion (SfM) photogrammetric principles [77]. During this stage, the software automatically detects characteristic features within the overlapping RGB images and searches for corresponding features across neighboring photographs. These characteristic features generally correspond to visually distinctive elements such as edges, texture variations, rocks, vegetation patterns, or contrast discontinuities that remain identifiable from different viewing angles. In other words, any recognizable features that the algorithm can distinguish [3].

Once matching features are identified between multiple overlapping images, the software estimates the relative camera positions and orientations through triangulation and bundle adjustment procedures. Simultaneously, an initial three-dimensional reconstruction of the scene geometry is generated in the form of a sparse point cloud [3].

For an order of magnitude, the sparse point cloud have several hundreds thousands of tie points, leading to a rather important processing time.

The quality of the image alignment strongly depends on several factors including image overlap, illumination conditions, and the presence of sufficiently distinctive surface features [21].

The image alignment stage can therefore be associated with a first needed preliminary step to generate different surfaces, including dense point clouds, Digital Elevation Models (DEMs), and orthomosaics, directly depend on the geometric consistency of the reconstructed camera positions and scene geometry.

Figure 3.6 illustrates the sparse point cloud obtained after the image alignment procedure.

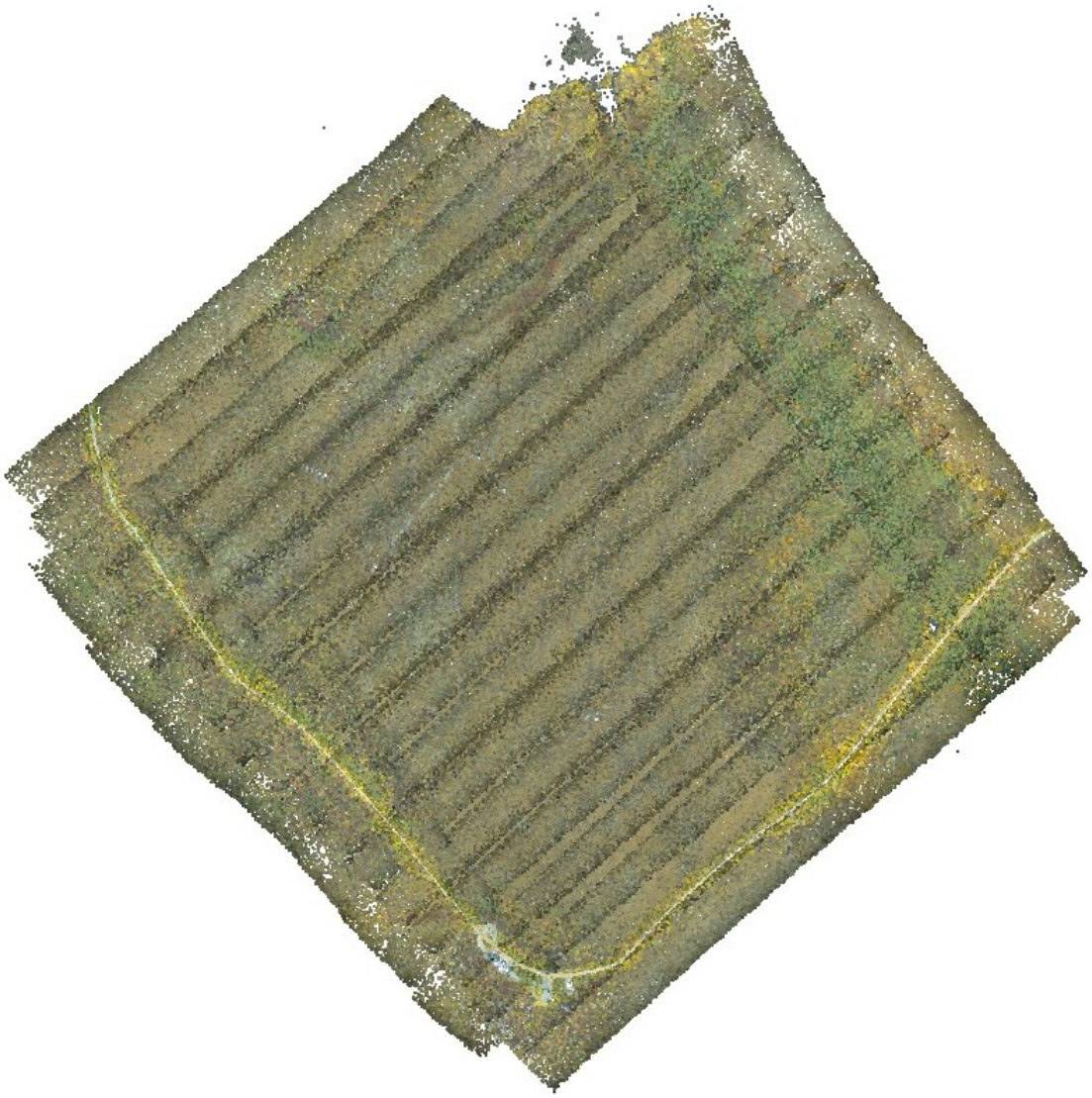


Figure 3.6: Sparse point cloud generated during the image alignment stage in Agisoft Metashape.

3.3.1.2 Ground Control Point Integration

Prior to making the flights, different Ground Control Points (GCPs) have been put in the scenery. They consist of a black and white plate.

Ground Control Points correspond to reference locations with known geographic coordinates measured directly in the field during the acquisition campaign. These points provide spatial constraints allowing the photogrammetric model to be accurately georeferenced within a real-world coordinate system [38].

The GCP integration procedure was performed manually within Agisoft Metashape by identifying the corresponding locations of each control point across multiple RGB images. Particular attention was given to the precise placement of the markers in order to minimize geometric inaccuracies during the subsequent reconstruction stages.

Once the GCPs were integrated into the aligned dataset, the camera positions and scene geometry were optimized through bundle adjustment procedures. This refinement stage improved the spatial consistency of the photogrammetric reconstruction and reduced geometric distortions affecting the generated terrain products.

The integration of GCPs was particularly important for the generation of reliable Digital Elevation Models (DEMs) and RGB orthomosaics, which were later used during the hyperspectral georectification and boresight calibration procedures. Accurate spatial referencing was therefore essential to ensure the consistency between the RGB products and the hyperspectral imagery throughout the preprocessing workflow.

3.3.1.3 Point Cloud Generation

Following the image alignment and GCP integration stages, a dense point cloud was generated in Agisoft Metashape in order to obtain a more detailed three-dimensional reconstruction of the study area.

In photogrammetry, a point cloud corresponds to a three-dimensional representation of the observed scene composed of a large number of points positioned in space according to their estimated geographic coordinates. Each point represents a portion of the reconstructed surface and may contain additional information such as RGB color values derived from the original imagery [77].

While the sparse point cloud generated during the image alignment stage mainly serves to estimate the camera geometry and reconstruct the general structure of the scene, the dense point cloud provides a significantly more detailed representation of the terrain surface. The dense reconstruction is obtained by performing dense image matching between the aligned photographs in order to estimate depth information for a much

larger number of pixels across the overlapping images [77].

Again, for an order of magnitude, compared to the sparse cloud with a few hundreds thousands points, in this case the dense point cloud is around 150 000 000 points. In terms of processing time it can reach 24 hours just for this step.

However, the generated dense point cloud is highly important as it constitutes the basis for the generation of the Digital Elevation Models (DEMs) and RGB orthomosaics used throughout the hyperspectral preprocessing workflow.

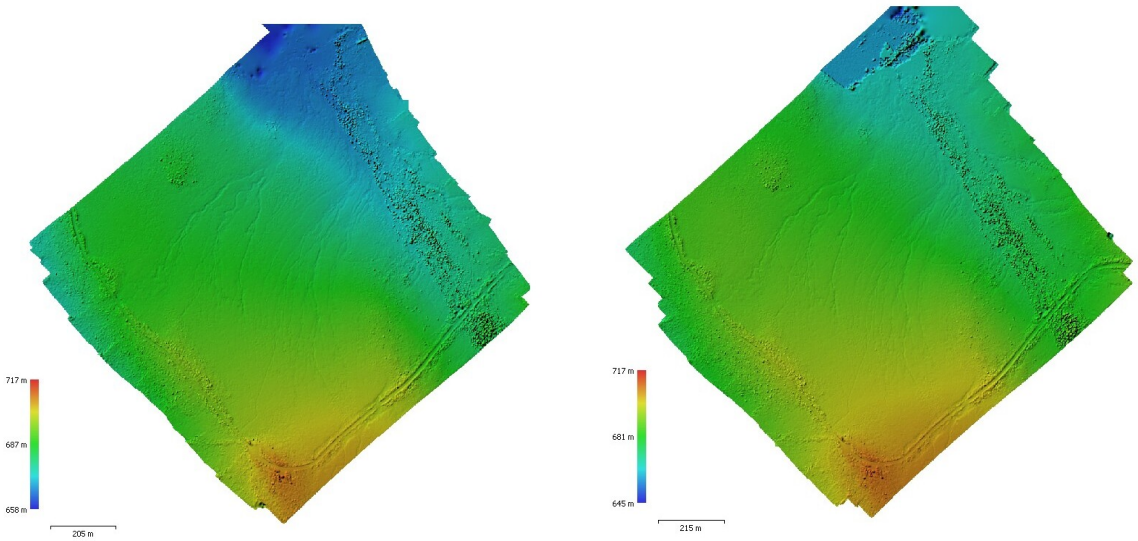
3.3.1.4 DEM Generation

Following the dense point cloud reconstruction stage, Digital Elevation Models (DEMs) were generated in Agisoft Metashape in order to obtain a raster representation of the terrain elevation across the study area.

A DEM corresponds to a digital representation of the surface topography in which each pixel contains an elevation value associated with the terrain surface. In the context of UAV photogrammetry, DEMs are commonly derived from dense point clouds by interpolating the elevation information reconstructed [52].

As mentioned earlier, the DEM quality is dependent on the dense point cloud. So inevitably, depending on the campaign, the DEM results can differ. In fact, each campaign had different illumination conditions, weathers etc...

A quick way of validating a DEM would be to visually look at the DEMs produced from different campaigns. Despite variations in conditionsbetween the different UAV acquisitions, the generated DEMs remained globally consistent in terms of terrain representation and spatial structure. Figure 3.7 illustrates an example of a DEM generated during the photogrammetric reconstruction workflow.



(a) Flight 1 (b) Flight 2

Figure 3.7: Comparison of Digital Elevation Models (DEMs) generated from two different UAV acquisitions. Despite variations in acquisition parameters, both DEMs present globally consistent terrain structures and elevation patterns.

In order to qualitatively evaluate the consistency of the photogrammetrically reconstructed terrain surface, the generated DEMs were compared with a DEM derived from LiDAR data available for the study area.

LiDAR (Light Detection and Ranging) is an active remote sensing technique based on the emission of laser pulses toward the ground surface and the measurement of the returned signal travel time. By precisely estimating the distance between the sensor and the terrain, LiDAR systems are capable of generating highly accurate three-dimensional representations of the surface topography [76].

Compared with photogrammetric reconstruction methods, LiDAR-derived elevation models are generally considered more robust for terrain representation, particularly in environments characterized by dense vegetation or complex surface structures. Several studies have shown that photogrammetric reconstructions may exhibit larger elevation uncertainties and tend to underestimate surface elevations relative to LiDAR-derived products under certain land cover conditions [47]. Consequently, LiDAR products are frequently used as reference datasets for terrain modeling applications, which is also the case in this study. Although DEMs generated from Metashape are used throughout the preprocessing workflow, LiDAR-derived elevation products are preferred during the machine learning analyses of thaw depth.

A way of comparing both results is to make a difference map, as seen on Figure 3.8

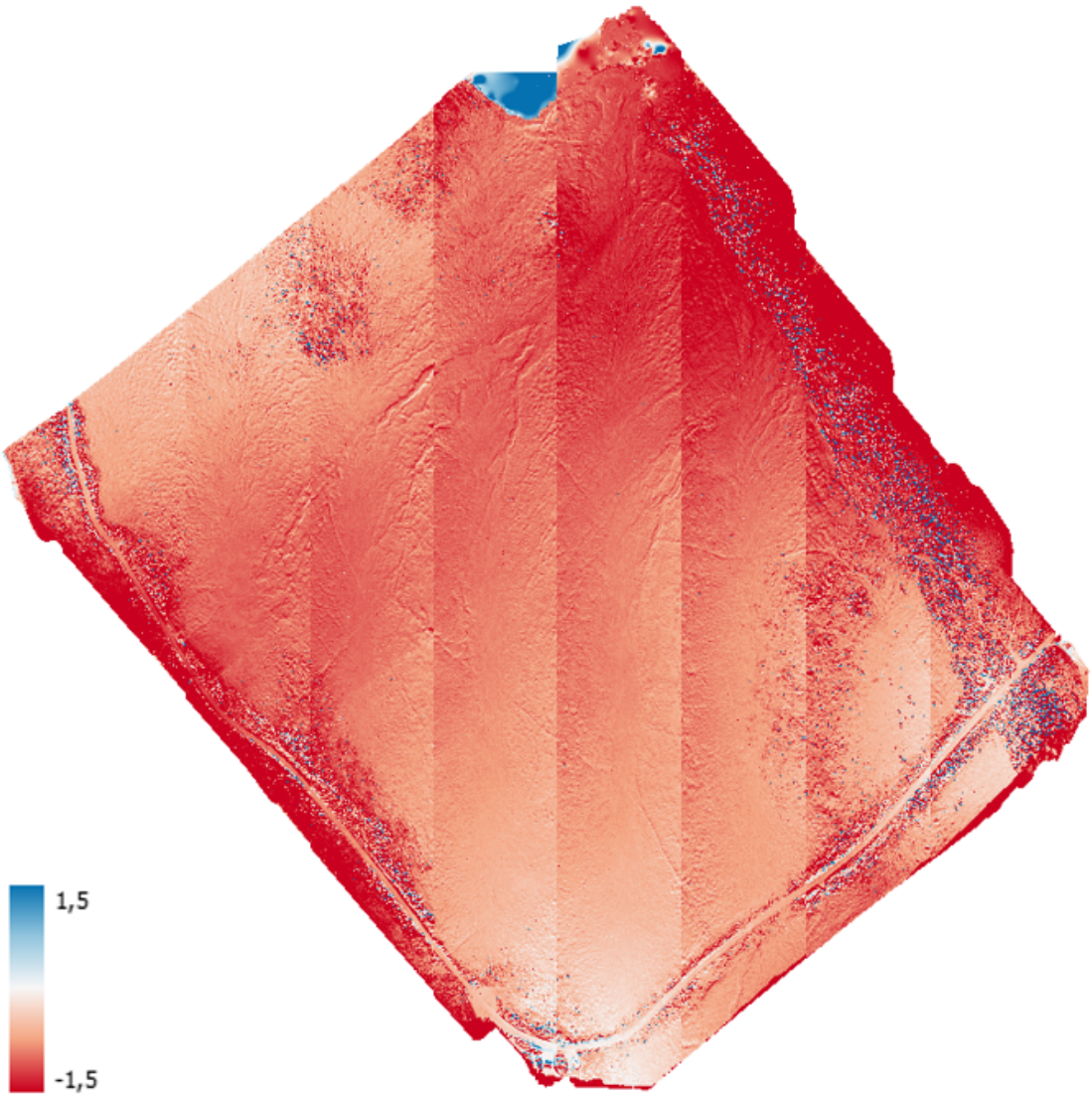


Figure 3.8: Elevation difference map between the LiDAR-derived DEM and the DEM generated from the hyperspectral processing workflow.

Overall, the largest elevation differences are mainly located along the borders of the study area. This behavior is expected, as DEM quality generally decreases near mosaic edges and areas characterized by lower overlap or less reliable reconstruction [48]. Since the field sampling locations are concentrated within the central portion of the study area, these border effects are not expected to significantly influence the analyses.

Within the central portion of the study area, the elevation differences remain relatively limited and generally fall within the range indicated by the color scale, approximately between -1.5 m and 1.5 m. The map also reveals several striping patterns extending across the study area. However, their exact origin could not be determined with certainty from the available data.

Although the difference map appears to be dominated by negative values, the sign of

the differences is not further interpreted in this study. Several processing-related factors may contribute to systematic offsets between both elevation products, including differences in DEM generation algorithms, georeferencing procedures, interpolation methods, or vertical reference definitions. Consequently, the analysis focuses primarily on the spatial distribution and magnitude of the differences rather than on the interpretation of a sign.

Overall, the comparison indicates a satisfactory agreement between the LiDAR-derived DEM and the hyperspectral DEM within the central portion of the study area, where all analyses were performed.

3.3.1.5 Orthomosaic Generation

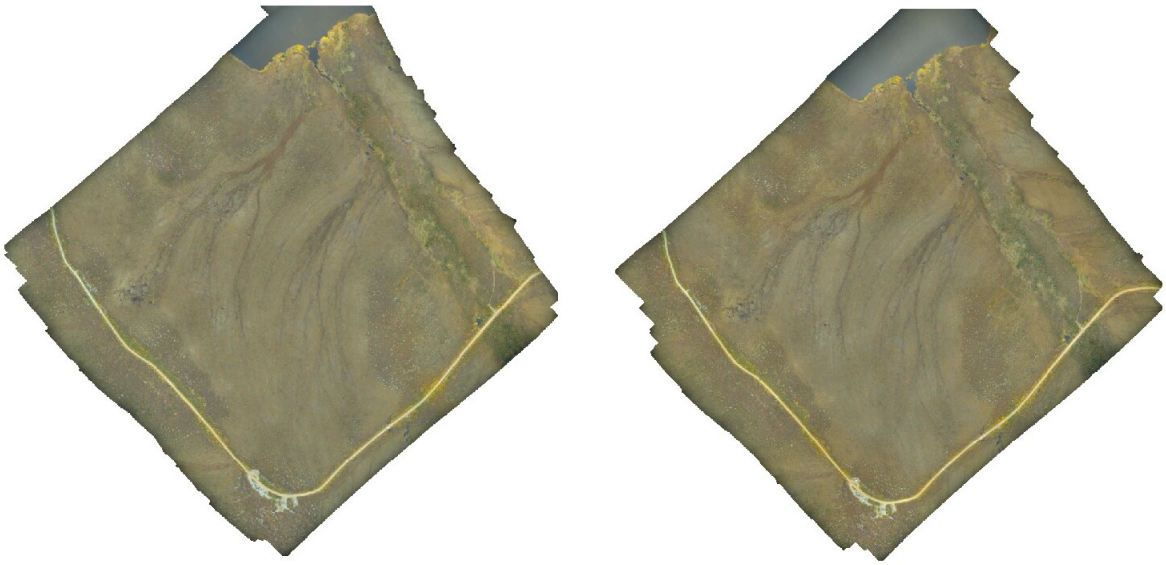
Following the DEM generation stage, RGB orthomosaics were produced in using the aligned RGB imagery together with the reconstructed terrain model. Orthomosaics correspond to geometrically corrected composite images generated by mosaicking multiple overlapping photographs while accounting for terrain relief and camera geometry [80].

Unlike conventional aerial photographs, orthomosaics provide a spatially consistent representation of the study area in which distortions caused by camera perspective and topographic variations are minimized. Each pixel is therefore associated with a corrected geographic position, allowing reliable spatial visualization and spatial comparison across the entire scene [80].

The orthomosaic generation process relied on the previously estimated camera positions together with the DEM generated during the photogrammetric reconstruction workflow. Individual RGB images were projected onto the reconstructed terrain surface before being merged into a single continuous raster covering the study area [77].

The generated RGB orthomosaics played an important role throughout the hyperspectral preprocessing workflow. In particular, they were later used during the boresight calibration and georectification stages in order to visually compare spatial features between the RGB and hyperspectral datasets. The orthomosaics also provided a detailed visualization of the tundra landscape and surface heterogeneity observed across the study area [77].

Despite variations in acquisition parameters between the different UAV campaigns, the generated orthomosaics remained globally consistent in terms of terrain representation, vegetation distribution, and overall spatial structure. Figures 3.9a and 3.9b illustrate examples of RGB orthomosaics generated from two different acquisition campaigns.



(a) Campaign 1 (b) Campaign 2

Figure 3.9: Comparison of RGB orthomosaics generated from two different UAV acquisition campaigns. Despite variations in flight parameters, both orthomosaics present globally consistent terrain structures and vegetation patterns.

Although most acquisition campaigns produced satisfactory orthomosaics, one campaign was characterized by significant snow cover across a substantial portion of the study area. As illustrated in Figure 3.10, the snow-covered surfaces considerably reduced the visibility of stable ground features and surface textures required for reliable photogrammetric reconstruction and subsequent calibration procedures.

The presence of snow introduced additional difficulties during the workflow, particularly during the boresight calibration stage where visual correspondences between the RGB orthomosaic and the hyperspectral imagery were required. Homogeneous snow-covered areas provided fewer distinctive features for accurate spatial matching and visual interpretation.

Consequently, the snow-covered acquisition campaign was excluded from the subsequent hyperspectral preprocessing workflow. Following this selection step, the number of campaigns considered for further processing was reduced from six to five acquisitions.

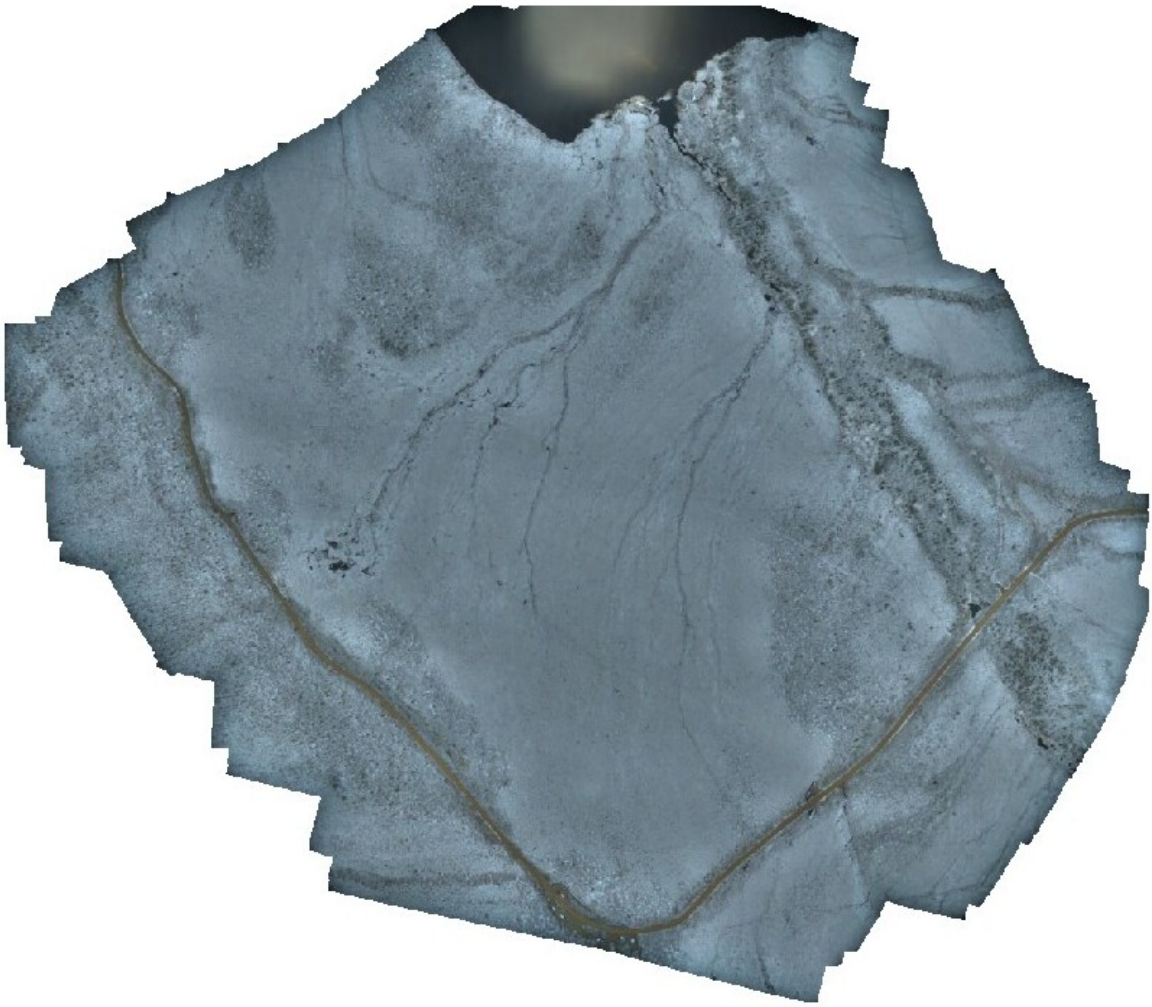


Figure 3.10: RGB orthomosaic generated from the snow-covered acquisition campaign. The presence of snow reduced the visibility of stable surface features required for reliable calibration and georectification procedures.

Additional orthomosaics generated from the remaining acquisition campaigns are provided in Appendix A

3.3.1.6 IMU-GPS File Generation

The last step of the RGB preprocessing is related to the generation of the IMU-GPS files. In fact, navigation-related information are required for the hyperspectral georectification stages. And those were generated using the HAIP Blackbird Converter software. This step consisted in extracting and organizing the navigation data associated with the hyperspectral acquisitions, including GPS positioning and inertial measurement information recorded during the UAV flights.

The generated IMU-GPS files contained essential information regarding the spatial position and orientation of the hyperspectral sensor during the acquisitions. In par-

ticular, these files included navigation parameters such as geographic coordinates, altitude, roll, pitch, and yaw values associated with each hyperspectral scanline.

The IMU-GPS information constituted a critical component of the subsequent hyperspectral georectification workflow performed in PARGE. During the georectification process, the navigation data were used together with the DEM and RGB orthomosaics generated during the RGB preprocessing workflow in order to spatially reconstruct the hyperspectral imagery and estimate the geometric position of each scanline across the study area.

However, due to residual geometric uncertainties associated with sensor orientation and platform motion during the acquisitions, additional geometric refinement procedures were later required during the boresight calibration stage.

The generation of the IMU-GPS files marked the end of the RGB preprocessing branch of the workflow. In parallel, additional preprocessing operations were also performed directly on the hyperspectral imagery before both processing branches were integrated within the PARGE georectification workflow.

3.3.2 HSI Preprocessing

In parallel with the RGB preprocessing workflow, several preprocessing operations were also performed directly on the hyperspectral imagery prior to the georectification stages carried out in PARGE.

3.3.2.1 Flightline Extraction

The hyperspectral acquisitions were first separated into individual flightlines corresponding to the successive acquisition paths followed by the UAV during the campaigns. For information, the first three campaigns have a total of 16 flightlines, campaign 4 and 5 have 22 flightlines and the last campaign has 9 flightlines. Indeed, as seen on the different orthomosaics provided earlier or in the Appendix, the paths were not always the same.

Instead of processing the complete hyperspectral dataset as a single image, each flightline was processed independently during the subsequent georectification workflow. This approach was mostly used to allow improved geometric corrections and calibrations. Processing the flightlines individually facilitated the correction of potential alignment errors affecting specific portions of the acquisitions.

3.3.2.2 Reflectance Calibration Target Preparation

In addition to the flightline extraction procedures, reflectance calibration targets acquired during the field campaigns were prepared for the subsequent radiometric correction stages. These calibration targets consisted of reference panels with known reflectance properties positioned within the scene during the hyperspectral acquisitions.

The calibration panels provided a radiometric reference allowing the normalization and correction of the hyperspectral data prior to the atmospheric correction stages. By comparing the measured hyperspectral signal with the known reflectance characteristics of the calibration targets, the workflow aimed to improve the radiometric consistency of the generated reflectance products.

The prepared calibration target data were later integrated within the atmospheric correction workflow performed in DROACOR in order to support the generation of reliable surface reflectance products.

3.3.3 Geocoding

Following the RGB and HSI preprocessing stages, the hyperspectral imagery was processed in PARGE (PARametric GEocoding), a software specifically designed for the geometric correction and georectification of airborne and UAV hyperspectral data.

As a reminder, hyperspectral data is acquired using pushbroom sensors which are recorded line by line during the UAV flight. Consequently, the geometric reconstruction of the hyperspectral imagery depends not only on the terrain geometry but also on the precise position and orientation of the sensor during each scanline acquisition [66].

Small uncertainties affecting the GPS positioning, IMU measurements, UAV motion, or sensor orientation may therefore introduce geometric distortions and spatial misalignments within the reconstructed hyperspectral imagery. Accurate georectification procedures are consequently required in order to spatially reconstruct the hyperspectral data and ensure spatial consistency with the RGB-derived products generated during the previous workflow stages[73].

The PARGE workflow implemented in this study mainly consisted of two major stages: boresight calibration and hyperspectral georectification. In order to improve the geometric accuracy of the reconstruction, the preprocessing operations were performed independently for each individual flightline rather than processing the complete hyperspectral acquisition as a single dataset [65].

The georectification workflow performed in PARGE relied on several products generated during the previous preprocessing stages, including the DEM, RGB orthomosaics, IMU-GPS navigation files, and separated hyperspectral flightlines. These products were jointly used to spatially reconstruct the hyperspectral imagery and refine its geometric consistency across the study area.

3.3.3.1 Boresight Calibration

The first major stage performed in PARGE consisted of the boresight calibration procedure. This step aimed to refine the geometric relationship between the hyperspectral sensor and the navigation system mounted on the UAV platform.

During hyperspectral acquisitions, small misalignments may exist between the physical orientation of the sensor and the orientation estimated by the IMU/GPS system. These residual offsets may affect the roll, pitch, and yaw angles associated with the hyperspectral scanlines and consequently introduce spatial distortions or positioning errors within the reconstructed imagery [73].

Because pushbroom hyperspectral sensors acquire the scene line by line during the UAV motion, even small orientation uncertainties may generate noticeable geometric discrepancies between neighboring scanlines or between the hyperspectral imagery and the RGB-derived products generated during the previous preprocessing stages.

The boresight calibration procedure therefore aimed to minimize these geometric inconsistencies by refining the orientation parameters used during the hyperspectral reconstruction. This calibration stage was performed independently for each individual flightline in order to improve the geometric accuracy of the corrections and reduce the complexity associated with processing the complete acquisition as a single dataset.

The calibration process relied on visual comparisons between the georeferenced hyperspectral imagery and the RGB orthomosaics generated during the photogrammetric reconstruction workflow. Distinctive terrain features such as vegetation structures, water tracks, surface patterns, and geomorphological elements were used as spatial references to evaluate the geometric consistency between both datasets.

The DEM generated in Agisoft Metashape also played an important role during the calibration procedure. Since the geometric reconstruction of hyperspectral imagery is strongly influenced by terrain variations, the DEM allowed terrain-induced distortions to be accounted for during the scanline projection and spatial correction procedures.

Several iterative adjustments were performed during the boresight calibration stage in order to progressively improve the alignment between the hyperspectral flightlines

and the RGB reference products. The calibration quality was evaluated visually by assessing the spatial correspondence of identifiable terrain structures across the different datasets.

The line-by-line processing strategy adopted throughout the workflow considerably facilitated this calibration stage. Treating each flightline independently allowed local geometric inaccuracies to be corrected more precisely while preventing potential error propagation across the complete hyperspectral acquisition.

Following the boresight calibration procedure, the refined geometric parameters were used during the final georectification stage in order to generate spatially corrected hyperspectral flightlines consistent with the RGB-derived products and terrain geometry of the study area.

3.3.3.2 Hyperspectral Georectification

Following the boresight calibration procedure, the refined geometric parameters were used to perform the final georectification of the hyperspectral imagery in PARGE. This stage aimed to generate spatially corrected hyperspectral flightlines accurately aligned with the terrain geometry and the RGB-derived reference products generated during the previous preprocessing stages.

The georectification workflow relied on the DEM, the corrected IMU/GPS navigation data, and the refined boresight calibration parameters obtained during the previous calibration stage. Using these inputs, each hyperspectral scanline was spatially projected onto the reconstructed terrain surface in order to estimate the geographic position associated with every pixel of the hyperspectral imagery.

Because the hyperspectral data were acquired using a pushbroom sensor, the geometric reconstruction process had to account for the continuous motion of the UAV platform during the acquisitions. Variations in sensor orientation, altitude, platform stability, and terrain elevation could otherwise introduce distortions affecting the spatial consistency of the reconstructed imagery.

The use of the DEM during the georectification stage was particularly important in order to account for terrain-induced geometric distortions. By integrating elevation information into the reconstruction process, the workflow improved the spatial positioning of the hyperspectral data across the study area and reduced geometric discrepancies associated with topographic variations.

The georectification procedure was performed independently for each hyperspectral flightline following the line-by-line processing strategy adopted throughout the work-

flow. This approach allowed local geometric adjustments to be applied more precisely and improved the overall spatial consistency of the reconstructed imagery.

Following the georectification stage, spatially corrected hyperspectral flightlines were obtained for each acquisition campaign. These georeferenced products constituted the basis for the subsequent atmospheric correction procedures performed in DROACOR in order to generate surface reflectance data suitable for spectral analysis and machine learning applications.

3.3.4 Atmospheric Correction

Following the georectification procedures performed in PARGE, the hyperspectral flightlines were processed in DROACOR in order to perform atmospheric correction and generate surface reflectance products suitable for spectral analyses [67].

Although the hyperspectral imagery had already been geometrically corrected during the previous preprocessing stages, the recorded signal still contained atmospheric and radiometric effects affecting the measured spectral response. Consequently, additional correction procedures were required in order to retrieve reflectance values more representative of the actual surface properties of the study area.

3.3.4.1 Atmospheric Correction Principles

Hyperspectral sensors measure electromagnetic radiation reaching the sensor after interactions between solar illumination, the atmosphere, and the Earth's surface. As a result, the recorded signal is influenced not only by the reflectance properties of the observed surface but also by atmospheric scattering, absorption effects, illumination conditions, and sensor-related radiometric variations [39].

Atmospheric gases, aerosols, and water vapor may alter the spectral signal recorded by the sensor by absorbing or scattering portions of the incoming and reflected radiation. These atmospheric effects can introduce spectral distortions and reduce the comparability of spectral measurements across the scene.

The objective of atmospheric correction is therefore to minimize these atmospheric influences in order to retrieve surface reflectance values more directly related to the physical properties of the observed materials. Surface reflectance products are particularly important for hyperspectral analyses since spectral indices, band correlations, dimensionality reduction methods, and machine learning models strongly depend on the radiometric consistency of the spectral data [39].

In this workflow, atmospheric correction was performed in DROACOR using the geo-

rectified hyperspectral flightlines generated in PARGE together with the calibration target information prepared during the HSI preprocessing stages. The correction procedures aimed to improve the radiometric consistency of the generated hyperspectral products prior to the spectral analysis and Active Layer Depth (ALD) modeling stages.

Following the atmospheric correction workflow, reflectance hyperspectral flightlines were generated for each acquisition campaign. These corrected products were subsequently used to produce the final hyperspectral mosaics employed throughout the remainder of the study.

3.3.5 Output Reflectance Products

Following the atmospheric correction procedures performed in DROACOR, reflectance hyperspectral products were generated for each georectified flightline. These products consisted of hyperspectral reflectance cubes containing both spatial and spectral information across the full wavelength range covered by the HAIP Blackbird V2 sensor.

Unlike conventional RGB imagery, hyperspectral reflectance cubes contain a large number of spectral bands for each spatial pixel of the scene. Consequently, each pixel is associated not only with a geographic position but also with a complete spectral signature describing the reflectance properties of the observed surface materials across the visible and near-infrared spectral regions [2].

The generated reflectance products constituted the primary datasets used throughout the subsequent stages of this study. In particular, these hyperspectral cubes were later employed for spectral index computation, correlation analyses, dimensionality reduction procedures, and machine learning applications related to Active Layer Depth (ALD) estimation.

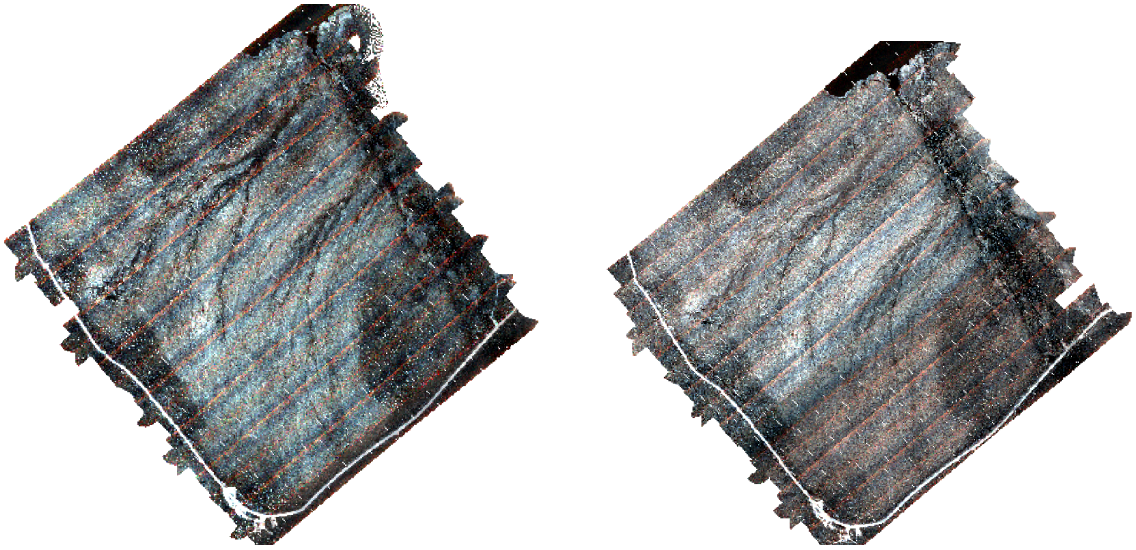
Although the atmospheric correction workflow substantially improved the radiometric consistency of the hyperspectral data, residual edge effects were still observed along portions of certain flightlines. These artifacts mainly appeared as abnormal pixel values and color inconsistencies affecting the outer regions of the reconstructed [72].

The origin of these edge effects was mainly related to geometric and radiometric uncertainties affecting the borders of the hyperspectral flightlines during the reconstruction and correction procedures. Because the hyperspectral imagery was acquired line by line using a pushbroom sensor mounted on a moving UAV platform, the outer scanlines were generally more sensitive to small geometric inaccuracies, sensor instabilities, and reconstruction uncertainties.

Following the generation of the reflectance mosaics, a final selection step was performed

in order to identify the acquisition campaign presenting the most suitable quality for the subsequent spectral analyses and machine learning applications. The selection was primarily based on the visual assessment of the reconstructed mosaics, including the evaluation of geometric consistency, radiometric quality, residual artifacts, and overall spatial coherence across the study area.

Although several acquisition campaigns produced satisfactory results throughout the preprocessing workflow, noticeable differences remained between the final mosaics in terms of reconstruction quality and residual artifacts. Figure 3.11 illustrates a comparison between two reflectance mosaics generated from different acquisition campaigns.



(a) Selected campaign (b) Rejected campaign

Figure 3.11: Comparison between two hyperspectral reflectance mosaics generated from different acquisition campaigns. The campaign presenting the highest overall geometric and radiometric consistency was selected for the subsequent analyses.

Consequently, the acquisition campaign presenting the most spatially and radiometrically consistent reconstruction was retained for the subsequent analyses performed throughout this study, which correspond to campaign 1. In conclusion, at this stage, the five other campaigns were rejected.

3.3.6 Post-Processing and Final Mosaic Generation

In order to reduce the residual edge artifacts affecting portions of the hyperspectral flightlines, additional post-processing operations were performed prior to the generation of the final hyperspectral mosaics.

The post-processing stage mainly consisted of trimming the outer borders of the flightlines where the edge effects were the most visible. Since the acquisition campaigns were

performed with significant overlap between adjacent flightlines, these problematic border regions could be partially removed without generating substantial gaps within the spatial coverage of the study area.

The overlap between neighboring flightlines therefore played an important role during the refinement stage by allowing visually degraded regions to be excluded while preserving the overall spatial continuity of the reconstructed hyperspectral imagery.

Following the trimming procedures, the corrected hyperspectral flightlines were merged together in order to generate continuous hyperspectral mosaics covering the complete study area. The mosaicking procedures combined the reflectance information from all corrected flightlines into a single multi-band hyperspectral dataset.

For visualization purposes, different spectral band combinations were used when displaying the final hyperspectral mosaics in QGIS. These band combinations only affected the visual rendering of the images and did not modify the underlying hyperspectral data used throughout the analyses.

Figure 3.12 illustrates the final hyperspectral mosaic obtained before the post-processing refinement procedures.

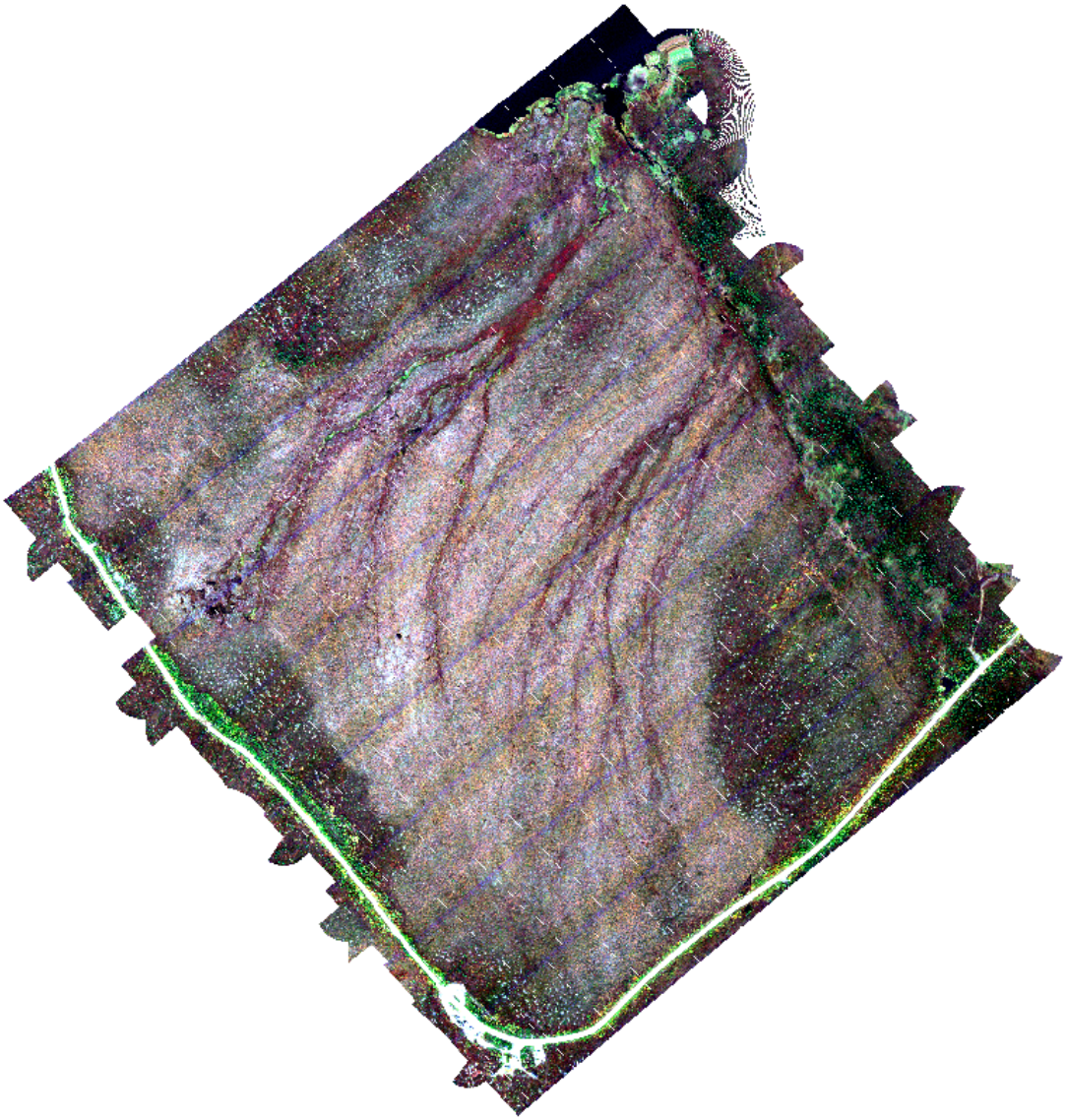


Figure 3.12: Final hyperspectral mosaic generated before the post-processing refinement stages.

Figure 3.13 illustrates the final hyperspectral mosaic obtained after the post-processing refinement procedures. Compared with the initial reconstruction, the visibility of edge artifacts was substantially reduced following the trimming and mosaicking stages.

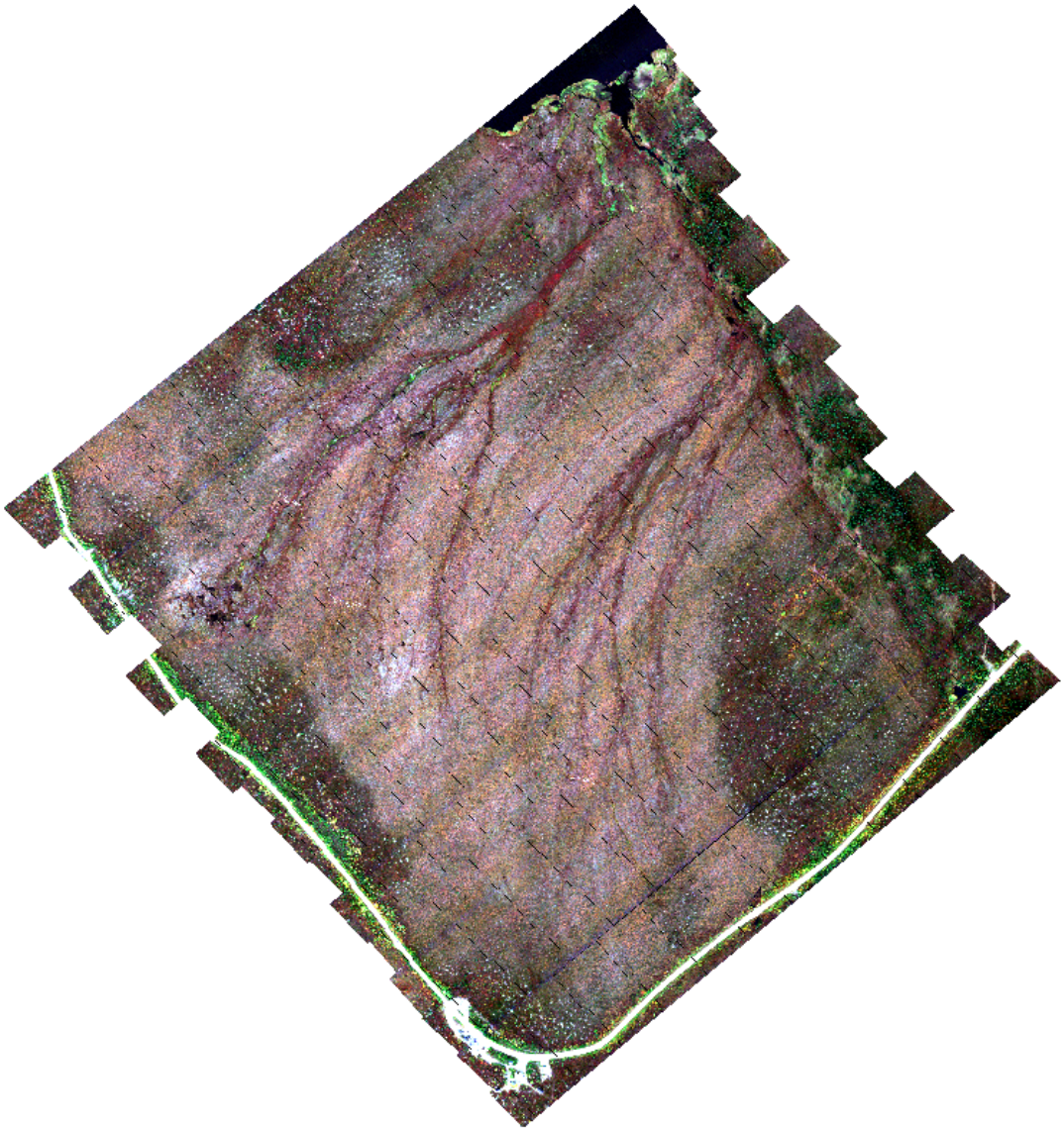


Figure 3.13: Final hyperspectral mosaic generated after the post-processing refinement stages. The trimming of flightline borders considerably reduced the visibility of residual edge artifacts.

The final hyperspectral mosaics generated through this workflow constituted the primary datasets used throughout the subsequent spectral analyses, dimensionality reduction procedures, and machine learning modeling stages of this study.

Chapter 4

Analysis and Results

4.1 Data Preparation

Following the hyperspectral preprocessing workflow, several datasets were generated in order to perform the subsequent spectral analyses and machine learning procedures. These datasets combined hyperspectral reflectance information with the corresponding Active Layer Depth (ALD) measurements acquired during the field campaigns.

The final hyperspectral mosaics generated through the preprocessing workflow constituted the primary datasets used throughout the analyses. Each hyperspectral pixel contained reflectance values distributed across the 100 spectral bands of the HAIP Blackbird V2 sensor covering the visible and near-infrared spectral regions.

In order to investigate the relationships between hyperspectral information and thaw depth variability, spectral values were extracted at the locations corresponding to the in situ ALD measurements. Several extraction approaches were considered throughout the analyses in order to evaluate the influence of spatial aggregation on the obtained results.

A first dataset was generated using direct pixel-based extraction, where the reflectance values associated with the hyperspectral pixel located at each measurement position were retrieved. This approach allowed the analyses to preserve the maximum spatial resolution of the hyperspectral imagery and directly evaluate the spectral response associated with the measurement locations.

However, relying exclusively on pixel-level extraction may introduce several limitations in hyperspectral analyses. Small geometric inaccuracies remaining after the georectification stages, GPS uncertainties associated with the field measurements, local spatial heterogeneity, and noise affecting individual pixels may reduce the robustness of the

extracted spectral information.

In order to reduce the influence of these local variations and improve the robustness of the extracted spectral information, mean reflectance values were also computed within buffer zones surrounding the measurement locations. Buffer extraction was performed using circular areas centred on each field measurement point. Consequently, a 2 m buffer corresponds to a circular region with a radius of 2 m around the sampling location, while a 5 m buffer corresponds to a radius of 5 m.

Different buffer sizes were considered throughout the analyses in order to evaluate the influence of spatial averaging on the relationships between hyperspectral information and ALD variability.

The generated datasets therefore contained hyperspectral reflectance information together with the corresponding thaw depth measurements and spatial information associated with each sampling location. These datasets were later used for the correlation analyses, vegetation index computations, dimensionality reduction procedures, and machine learning applications presented throughout the remainder of this study.

4.2 Spectral Correlation Analysis

4.2.1 Methodology

The objective of the spectral correlation analysis was to investigate the relationships between hyperspectral reflectance and Active Layer Depth (ALD) measurements. By evaluating the correlation between each spectral band and the corresponding ALD values, this analysis aimed to identify the wavelength regions exhibiting the strongest sensitivity to thaw depth variations. In addition, the spectral correlation analysis provided a first assessment of the predictive potential of the hyperspectral data prior to the application of more advanced dimensionality reduction and machine learning techniques.

Two complementary correlation metrics were considered throughout this study: the Pearson correlation coefficient and the Spearman rank correlation coefficient. The use of both metrics allowed the investigation of different types of relationships between spectral reflectance and ALD [54].

The Pearson correlation coefficient measures the strength and direction of a linear relationship between two variables and is defined as:

$$r = \frac{\sum_{i=1}^{n}(x_i - \bar{x})(y_i - \bar{y})}{\sqrt{\sum_{i=1}^{n}(x_i - \bar{x})^2}\sqrt{\sum_{i=1}^{n}(y_i - \bar{y})^2}} \tag{4.1}$$

where x_i represents the reflectance value of a given spectral band, y_i represents the corresponding ALD measurement, $\bar{x}$ and $\bar{y}$ are the sample means of the reflectance and ALD datasets, respectively, and n denotes the number of observations. The Pearson coefficient ranges between -1 and 1, where values close to 1 indicate a strong positive linear relationship, values close to -1 indicate a strong negative linear relationship, and values near 0 indicate little or no linear relationship. So in the context of this study, particular attention was given to the absolute magnitude of the correlation coefficients, as both strong positive and strong negative correlations may reveal wavelength regions sensitive to ALD variability.

In addition to Pearson correlation, the Spearman rank correlation coefficient was also computed. Unlike Pearson correlation, Spearman correlation is based on the ranks of the observations rather than their absolute values and is therefore capable of identifying monotonic relationships that may not necessarily be linear. The Spearman coefficient is defined as:

$$\rho = 1 - \frac{6\sum_{i=1}^{n} d_i^2}{n(n^2 - 1)} \tag{4.2}$$

where d_i represents the difference between the ranks of the two variables for observation i, and n denotes the number of observations. Similar to Pearson correlation, Spearman coefficients range between -1 and 1.

Pearson correlation was used to evaluate linear relationships between spectral reflectance and ALD, whereas Spearman correlation was used to investigate monotonic relationships independently of their exact functional form. The combined use of both metrics therefore provided a more comprehensive assessment of the spectral sensitivity of each wavelength to ALD variability.

The correlation analysis was performed independently for each of the 100 hyperspectral bands available in the dataset. Furthermore, the analysis was conducted using the different extraction approaches described in Section 4.1, including pixel-based reflectance values as well as mean reflectance values computed within buffer zones surrounding the measurement locations. This comparison allowed the influence of spatial averaging on the obtained correlations to be evaluated and contributed to the selection of the most suitable dataset for the rest of the analyses.

4.2.2 Comparison of Extraction Approaches

The Pearson and Spearman correlation coefficients were computed independently for the pixel-based dataset as well as for the datasets generated using the 2 m and 5 m buffer approaches. The objective of this comparison was to evaluate the influence of spatial averaging on the relationships observed between hyperspectral reflectance and Active Layer Depth (ALD).

Figures 4.1 and 4.2 present the correlation coefficients obtained across the full spectral range covered by the hyperspectral sensor.

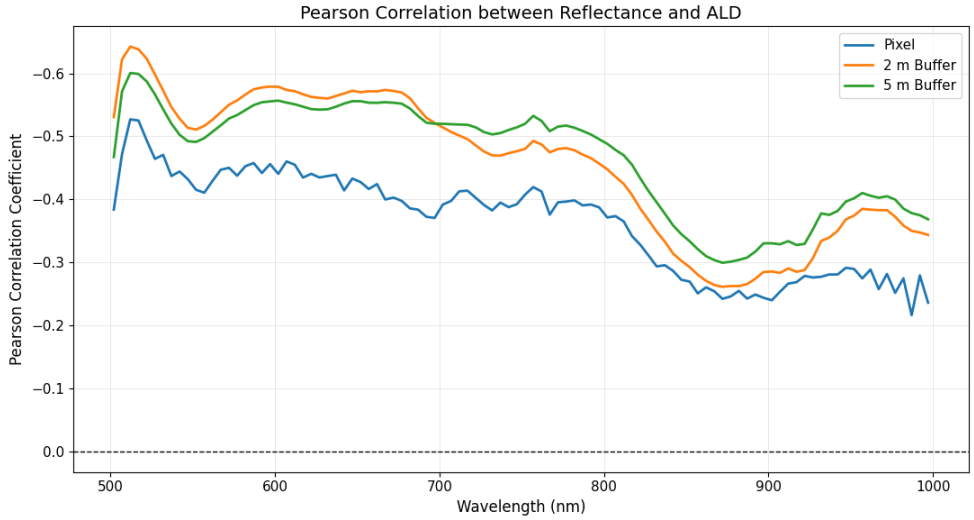


Figure 4.1: Comparison of Pearson correlation coefficients obtained for the pixel-based, 2 m buffer, and 5 m buffer datasets across the hyperspectral spectral range. The vertical axis was inverted for visualization purposes in order to facilitate the identification of wavelength regions exhibiting the strongest negative correlations with ALD.

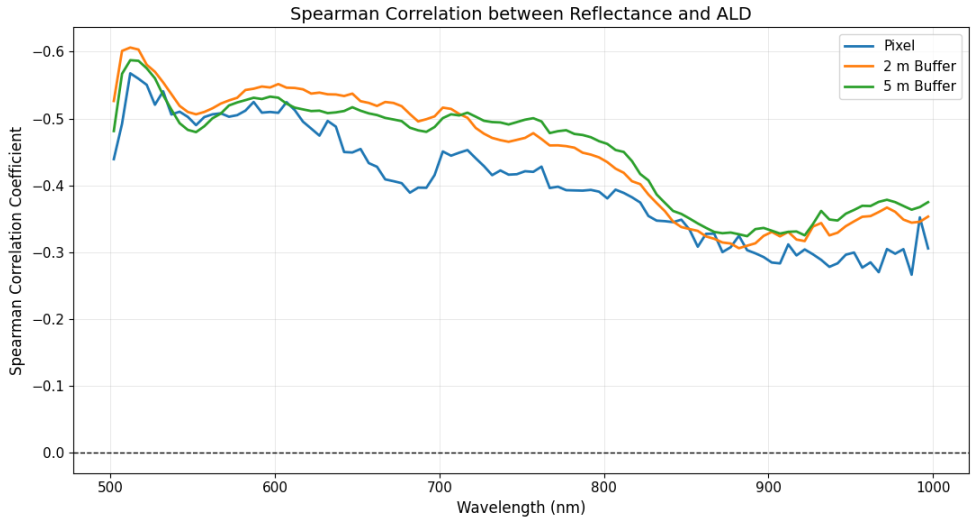


Figure 4.2: Comparison of Spearman correlation coefficients obtained for the pixel-based, 2 m buffer, and 5 m buffer datasets across the hyperspectral spectral range. The vertical axis was inverted for visualization purposes in order to facilitate the identification of wavelength regions exhibiting the strongest negative correlations with ALD.

Despite some local variations, the three extraction approaches exhibit similar overall spectral patterns. The main peaks and troughs are consistently observed at comparable wavelengths, suggesting that the identified spectral relationships are relatively robust and not solely driven by individual pixels or isolated observations.

For both Pearson and Spearman correlation coefficients, the pixel-based approach generally produced weaker correlations compared to the buffer-based approaches. This behavior is consistent with the limitations discussed in Section 4.1, where individual pixels may be more strongly affected by local spatial variability, residual georeferencing inaccuracies, and sensor noise. By averaging the reflectance values within a spatial neighborhood surrounding each measurement location, the buffer-based approaches reduced the influence of these local effects and provided more stable spectral responses.

The 2 m and 5 m buffer datasets exhibited very similar correlation patterns throughout the spectral range. In most wavelength regions, both approaches resulted in stronger correlations than the pixel-based dataset, confirming the benefits of spatial averaging for this application. At this point, the plots are showing a first clue that using buffer might perform better than working at the pixel-size level. As the rest of the analyses will show, the differences are going to be even clearer after.

4.2.3 Band-Wise Correlation Results

The spectral correlation analysis revealed several wavelength regions exhibiting moderate relationships with ALD. For both Pearson and Spearman correlation coefficients, the strongest correlations were consistently observed within the first spectral bands, corresponding approximately to the 510-530 nm wavelength range. Similar spectral patterns were obtained for both buffer-based extraction approaches, indicating that the identified relationships were relatively robust and not dependent on a specific buffer size.

Table 4.1 summarizes the strongest correlation coefficients obtained for the 2 m and 5 m buffer datasets. In both cases, the maximum correlation values were observed at 512 nm, with the 2m buffer dataset producing slightly stronger correlations than the 5 m buffer dataset. Again, this might be a first clue that the 2 m buffer is the best performing as the rest of the analyses will show.

Table 4.1: Highest Pearson and Spearman correlation coefficients obtained for the buffer-based datasets.

Dataset	Wavelength (nm)	Pearson r	Spearman ρ
2 m Buffer	512	-0.642	-0.606
5 m Buffer	512	-0.600	-0.587

Although the strongest correlations were observed at the same wavelength of the visible spectrum, the correlation curves indicate that several neighboring wavelength regions also exhibited moderate relationships with ALD, especially between 500 and 700 nm. This behavior suggests that the spectral response associated with ALD variability is not restricted to a single wavelength but rather extends across broader portions of the spectrum.

For both Pearson and Spearman coefficients, the correlations were negative. This indicates that higher reflectance values were generally associated with lower ALD measurements, whereas lower reflectance values tended to correspond to larger thaw depths. The negative sign itself does not indicate a weaker relationship, as the strength of the correlation is determined by the absolute magnitude of the coefficient rather than its direction.

Despite the presence of several moderately correlated wavelength regions, no individual band exhibited a sufficiently strong relationship to explain the full variability of the observed ALD measurements. Consequently, additional analyses were performed in order to investigate whether combinations of spectral bands could provide improved predictive capabilities. These analyses included vegetation index computation, di-

mensionality reduction through Principal Component Analysis (PCA), and machine learning approaches presented in the following sections.

4.3 Vegetation Indices Analysis

4.3.1 Methodology

Vegetation indices are mathematical combinations of spectral bands designed to enhance specific biophysical properties of vegetation. By combining reflectance measurements acquired at different wavelengths, these indices provide simplified indicators of vegetation characteristics that are often difficult to assess directly from individual spectral bands.

Vegetation indices have been widely used in remote sensing applications for the monitoring of vegetation health, biomass, photosynthetic activity, water content, and environmental stress.

In permafrost environments, vegetation characteristics are closely linked to surface conditions influencing Active Layer Depth (ALD). Vegetation cover affects the thermal regime of the ground through insulation, shading, and moisture regulation processes. Consequently, variations in vegetation density, water content, and physiological activity may indirectly reflect differences in thaw depth across the study area.

The objective of this analysis was therefore to investigate whether vegetation indices derived from hyperspectral imagery could provide stronger relationships with ALD than individual spectral bands. Several commonly used vegetation indices were computed and subsequently correlated with the measured ALD values using both Pearson and Spearman correlation coefficients.

The Normalized Difference Vegetation Index (NDVI) was included to characterize vegetation vigor and density. NDVI exploits the strong contrast between red reflectance, which is largely absorbed by chlorophyll, and near-infrared reflectance, which is strongly reflected by healthy vegetation [64]. It is defined as:

$$NDVI = \frac{NIR - Red}{NIR + Red} \tag{4.3}$$

The Normalized Difference Water Index (NDWI) was computed to investigate potential relationships between vegetation moisture conditions and ALD variability. In this study, NDWI was calculated as:

$$NDWI = \frac{Green - NIR}{Green + NIR} \tag{4.4}$$

The Simple Ratio (SR), another widely used vegetation metric, was also evaluated:

$$SR = \frac{NIR}{Red} \tag{4.5}$$

In addition to these conventional multispectral indices, several hyperspectral-specific indices were considered. The Photochemical Reflectance Index (PRI) was included because of its sensitivity to photosynthetic activity and vegetation stress:

$$PRI = \frac{R_{531} - R_{570}}{R_{531} + R_{570}} \tag{4.6}$$

Red-edge vegetation indices were also computed using wavelengths located near the red-edge region, which is known to be highly sensitive to vegetation structure and chlorophyll content. These indices included the red-edge NDVI (NDVI-RE) and the red-edge Simple Ratio (SR-RE).

Finally, the Modified Chlorophyll Absorption Ratio Index (MCARI) was calculated to assess whether chlorophyll-related spectral information could improve the relationship with ALD [81].

All vegetation indices were computed for the pixel-based, 2 m buffer, and 5 m buffer datasets. Their spatial distributions were first examined visually before evaluating their statistical relationships with ALD through correlation analysis.

4.3.2 Spatial Distribution of Vegetation Indices

Prior to the statistical analysis, the spatial distributions of several vegetation indices were examined in order to visualize the information extracted from the hyperspectral imagery. Among the computed indices, NDVI and PRI were selected as representative examples due to their widespread use in vegetation monitoring and their relevance to hyperspectral remote sensing applications.

Figure 4.3 presents the NDVI derived from the hyperspectral dataset. The index reveals spatial variability across the study area and highlights differences in vegetation conditions. Although the overall distribution appears relatively homogeneous, localized variations can be observed throughout the scene, indicating that the hyperspectral imagery successfully captures subtle changes in vegetation cover.

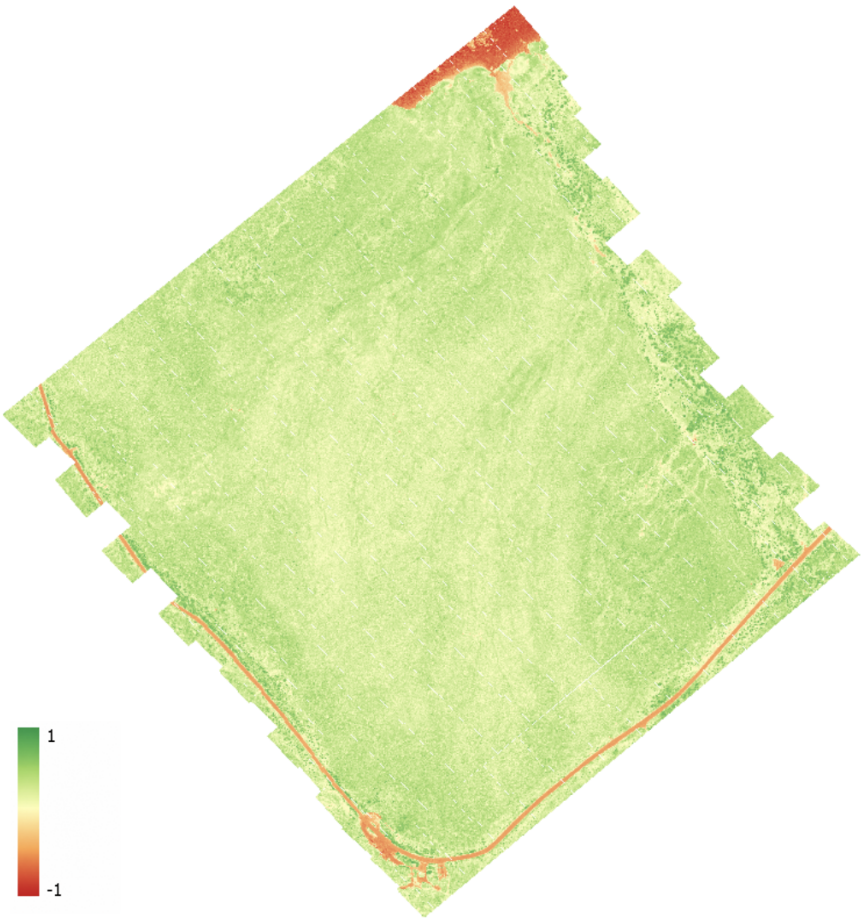


Figure 4.3: NDVI derived from the hyperspectral dataset.

Figure 4.4 shows the spatial distribution of the Photochemical Reflectance Index (PRI). Compared to NDVI, the PRI map exhibits different spatial patterns and a higher level of local variability. This behavior is expected since PRI is primarily related to vegetation physiological activity and stress rather than vegetation density alone. The resulting map illustrates the ability of hyperspectral imagery to derive vegetation indicators that exploit narrow spectral bands unavailable in most conventional multispectral sensors.

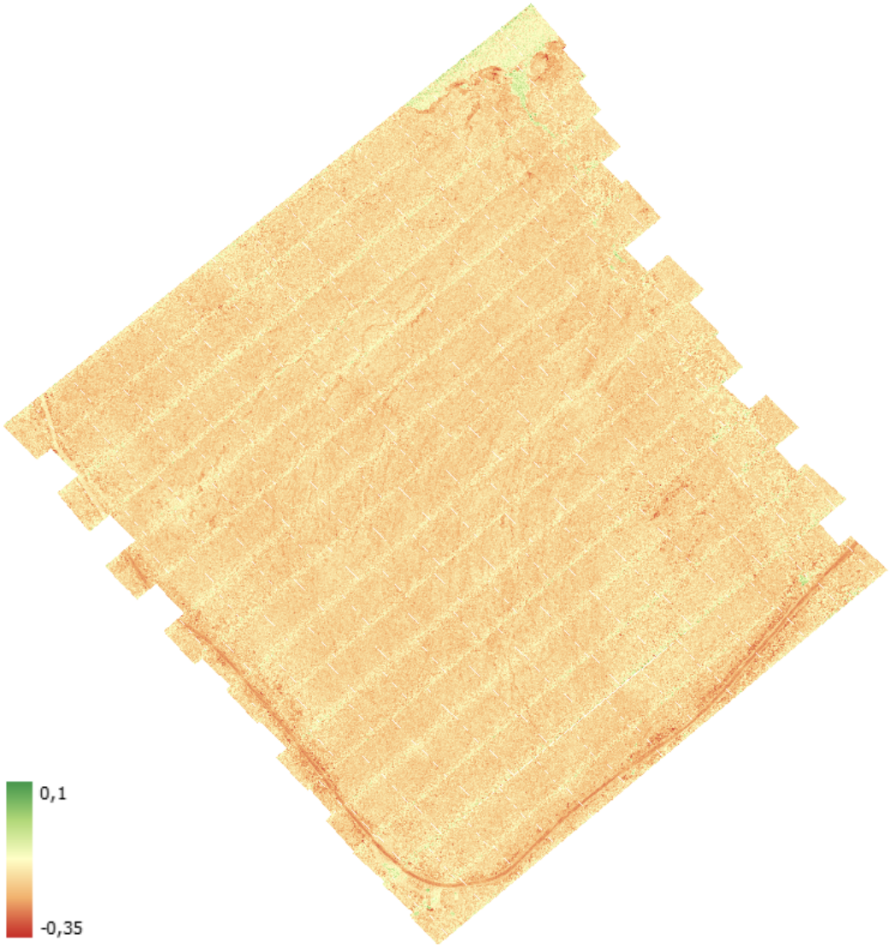


Figure 4.4: PRI derived from the hyperspectral dataset.

To assess the consistency of the generated products, the NDVI derived from the hyperspectral imagery was compared with the NDVI obtained from a pre-existing multispectral dataset seen on 4.5, which was utilized as an external reference for comparison purposes only. Figure 4.6 presents both NDVI products together with their corresponding difference map. This has been obtained by subtracting the NDVI value at each pixel of the image. Therefore, a value of 0 on the difference map would mean a perfect agreement between the multispectral and hyperspectral. The two NDVI datasets exhibit similar large-scale spatial patterns, indicating a good agreement between the hyperspectral and multispectral observations. The difference map further confirms that most discrepancies remain limited and spatially localized.

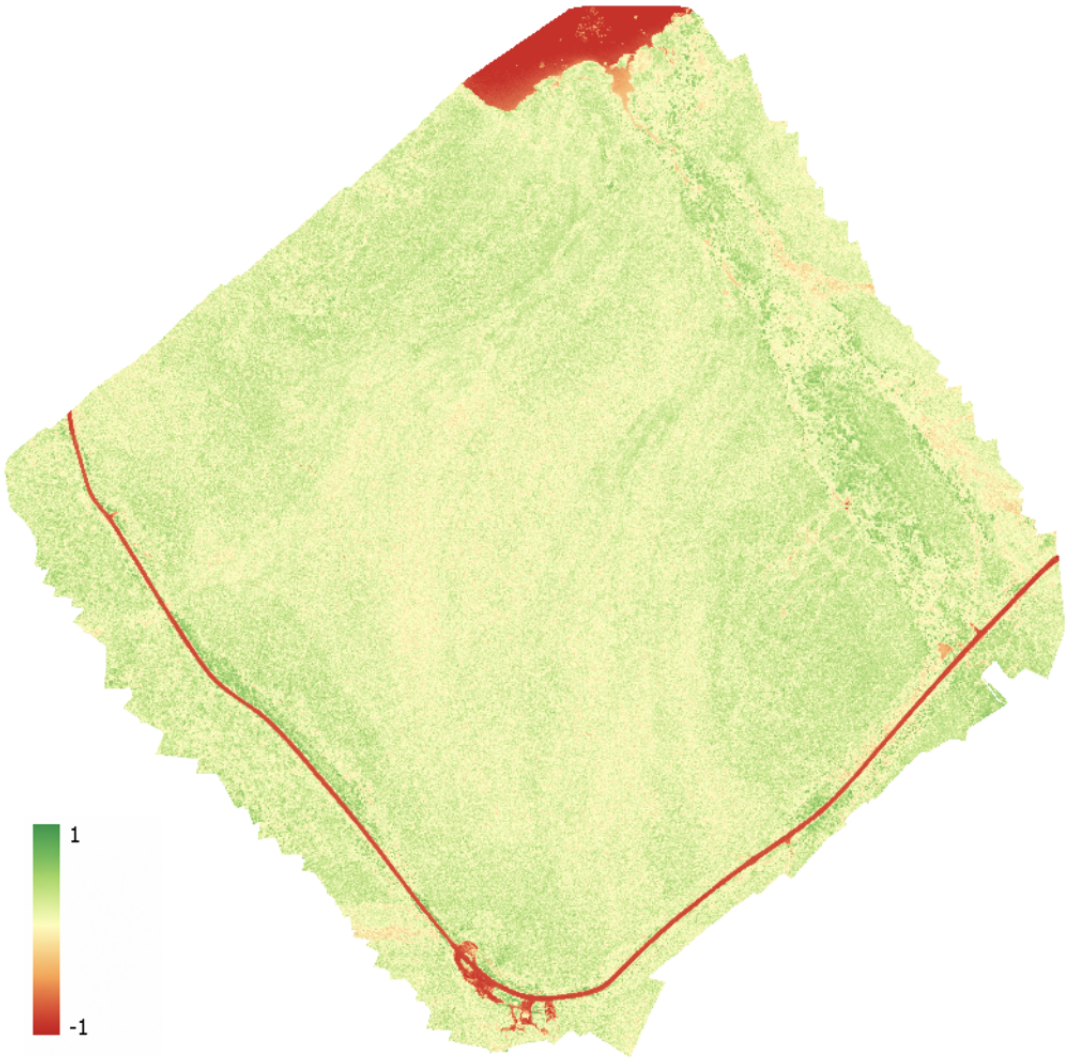


Figure 4.5: NDVI derived from multispectral imagery

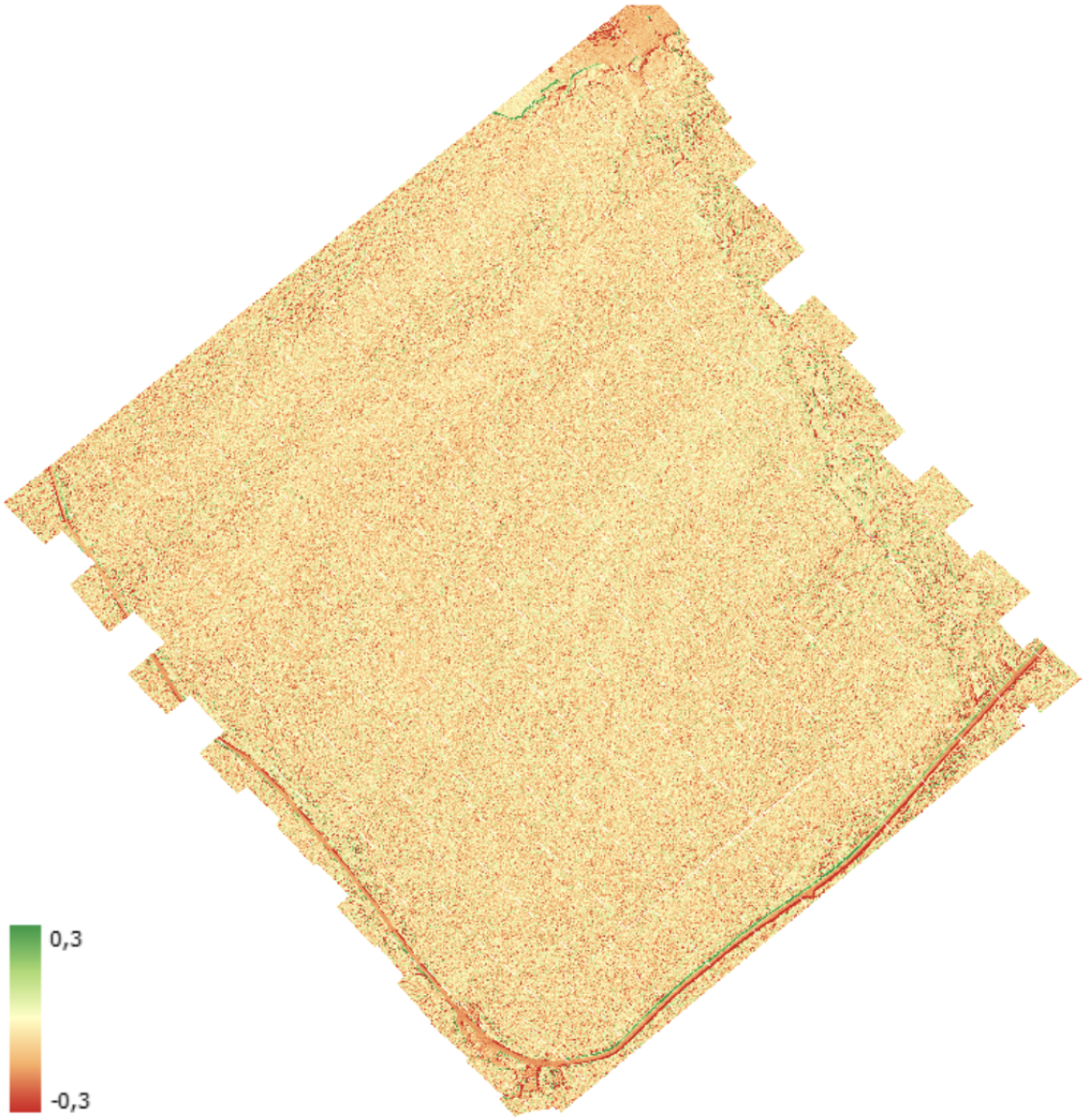


Figure 4.6: Comparison between NDVI derived from hyperspectral imagery, NDVI derived from multispectral imagery, and the corresponding difference map.

Overall, the computed vegetation indices provide a useful visual representation of the spatial variability present within the study area. However, visual inspection alone does not allow the relationship between vegetation characteristics and Active Layer Depth (ALD) to be quantified. Consequently, a statistical correlation analysis was performed in order to evaluate the predictive potential of the different vegetation indices.

4.3.3 Correlation with ALD

The relationship between the computed vegetation indices and Active Layer Depth (ALD) was evaluated using Pearson and Spearman correlation coefficients. Since both

metrics produced consistent rankings and similar conclusions, only the Pearson correlation results are presented in Figure 4.7 for clarity.

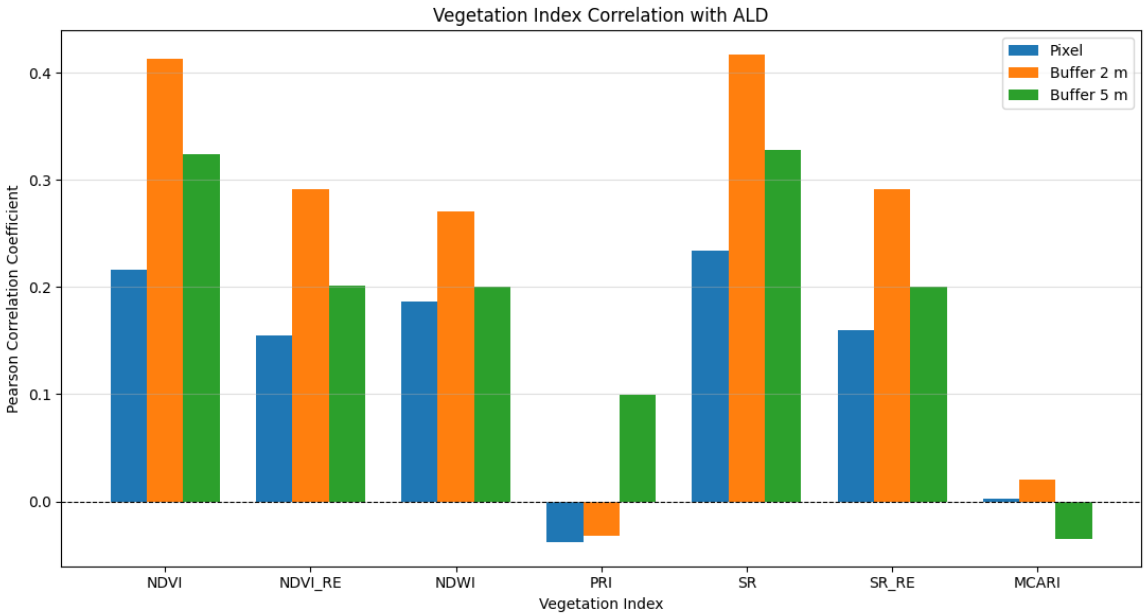


Figure 4.7: Pearson correlation coefficients between the computed vegetation indices and ALD for the pixel-based, 2 m buffer, and 5 m buffer datasets.

The results indicate that the strongest relationships with ALD were obtained using the Simple Ratio (SR) and the Normalized Difference Vegetation Index (NDVI). For the 2 m buffer dataset, both indices reached Pearson correlation coefficients of approximately 0.42, representing the highest values among all investigated vegetation indices. Similar trends were observed for the 5 m buffer and pixel-based datasets, although with lower correlation magnitudes.

Indices derived from the red-edge region, namely NDVI-RE and SR-RE, exhibited moderate correlations with ALD. While these indices provided useful information, their predictive potential remained lower than that of the conventional NDVI and SR indices. Likewise, NDWI produced moderate correlations, suggesting that moisture-related information may contribute to explaining part of the observed ALD variability.

In contrast, PRI and MCARI showed very weak relationships with ALD. Despite the hyperspectral nature of the dataset, these indices did not provide meaningful predictive information for the investigated site. This result suggests that vegetation physiological activity and chlorophyll-related indicators were not strongly linked to the measured ALD variations within the study area.

Overall, the vegetation index analysis confirms that certain vegetation characteristics are related to ALD. However, the maximum correlation coefficients obtained from the vegetation indices remain substantially lower than those achieved using the best

individual hyperspectral bands identified in Section 4.2. The strongest vegetation-index-based correlation ($r \approx 0.42$) remains significantly below the maximum band-wise correlation ($r \approx 0.64$). Consequently, combining spectral information through conventional vegetation indices does not appear to improve the relationship with ALD in this dataset. Also, a correlation coefficient of 0.42 is low, this is already a first hint that classical vegetation indices are not able to capture ALD accurately.

Nevertheless, these indices were retained as potential explanatory variables and will be further evaluated within the Random Forest framework presented later in this chapter which constitutes the biggest part of the analysis.

4.4 Principal Component Analysis

4.4.1 Methodology

Hyperspectral datasets typically contain a large number of highly correlated spectral bands. While this high spectral resolution provides detailed information about surface properties, it also introduces significant redundancy, since adjacent wavelengths often carry very similar information. Such redundancy can complicate data interpretation and may negatively impact subsequent modeling approaches [33].

Principal Component Analysis (PCA) is a widely used dimensionality reduction technique designed to transform the original variables into a new set of orthogonal variables known as principal components (PCs). Each principal component represents a linear combination of the original spectral bands and is constructed to maximize the variance explained within the dataset. The first principal component captures the largest proportion of variance, while each subsequent component explains the maximum remaining variance under the constraint of orthogonality [40].

Prior to PCA, the spectral bands were standardized in order to ensure that all wavelengths contributed equally to the analysis. PCA then seeks a new set of orthogonal axes, called principal components, that maximize the variance captured from the original dataset.

Mathematically, the first principal component is obtained by finding a vector of coefficients $\mathbf{a}_1$ that maximizes the variance of the projected data:

$$PC_1 = \mathbf{a}_1^T \mathbf{X} \tag{4.7}$$

subject to the constraint:

$$\mathbf{a}_1^T \mathbf{a}_1 = 1 \tag{4.8}$$

This optimization problem leads to the eigenvalue equation:

$$\mathbf{C}\mathbf{a}_k = \lambda_k \mathbf{a}_k \tag{4.9}$$

where $\mathbf{C}$ is the covariance matrix of the standardized spectral dataset, λ_k is the eigenvalue associated with the k-th principal component, and $\mathbf{a}_k$ is the corresponding eigenvector.

The eigenvector coefficients define the loadings of the principal component and quantify the contribution of each wavelength to the corresponding spectral pattern. The associated eigenvalue represents the amount of variance explained by that component. Consequently, principal components are ranked according to decreasing eigenvalues, with the first component capturing the largest fraction of the total dataset variance.

Each principal component can therefore be expressed as a linear combination of the original spectral bands:

$$PC_k = a_{k1}X_1 + a_{k2}X_2 + \cdots + a_{kn}X_n \tag{4.10}$$

where $X_1, X_2, \ldots, X_n$ are the standardized spectral bands and $a_{k1}, a_{k2}, \ldots, a_{kn}$ are the loading coefficients obtained from the eigenvector associated with the k-th principal component.

The cumulative explained variance after considering the first m principal components is defined as:

$$CV_m = \sum_{i=1}^{m} EV_i \tag{4.11}$$

where EV_i denotes the explained variance ratio associated with the i-th principal component and CV_m represents the cumulative explained variance.

Unlike the correlation analyses presented in the previous sections and the Random Forest models developed later in this study, PCA is an unsupervised technique. Consequently, the computation of the principal components does not take the Active Layer Depth (ALD) measurements into account. Instead, PCA identifies the dominant sources of spectral variability present within the hyperspectral dataset regardless of their relationship with ALD.

PCA was performed exclusively on the 2 m buffer dataset. Previous analyses, including the spectral correlation analysis and the vegetation index analysis, consistently showed that the 2 m buffer provided the strongest relationships with ALD. Therefore, this dataset was selected as the most relevant candidate for subsequent dimensionality reduction analyses. While the 5 m buffer and pixel-based datasets are fully evaluated within the subsequent Random Forest framework, they were excluded from the PCA workflow to maintain focus on the spatial support that exhibited the highest spectral sensitivity.

This analysis served two primary objectives. First, PCA was used as an exploratory tool to investigate the structure of the hyperspectral dataset and quantify the amount of redundancy present among the spectral bands. Second, PCA was evaluated as a potential feature selection strategy for subsequent Random Forest modeling. By identifying the wavelengths contributing most strongly to the principal components through loading analysis, PCA can be used to select a reduced subset of spectral bands while preserving a large proportion of the original spectral variability [10].

The explained variance ratios, cumulative explained variance, principal component loadings, and loading-based band importance metrics were examined.

4.4.2 Variance Explained by Principal Components

The explained variance associated with each principal component is presented in Figure 4.8, while the cumulative explained variance is shown in Figure 4.9.

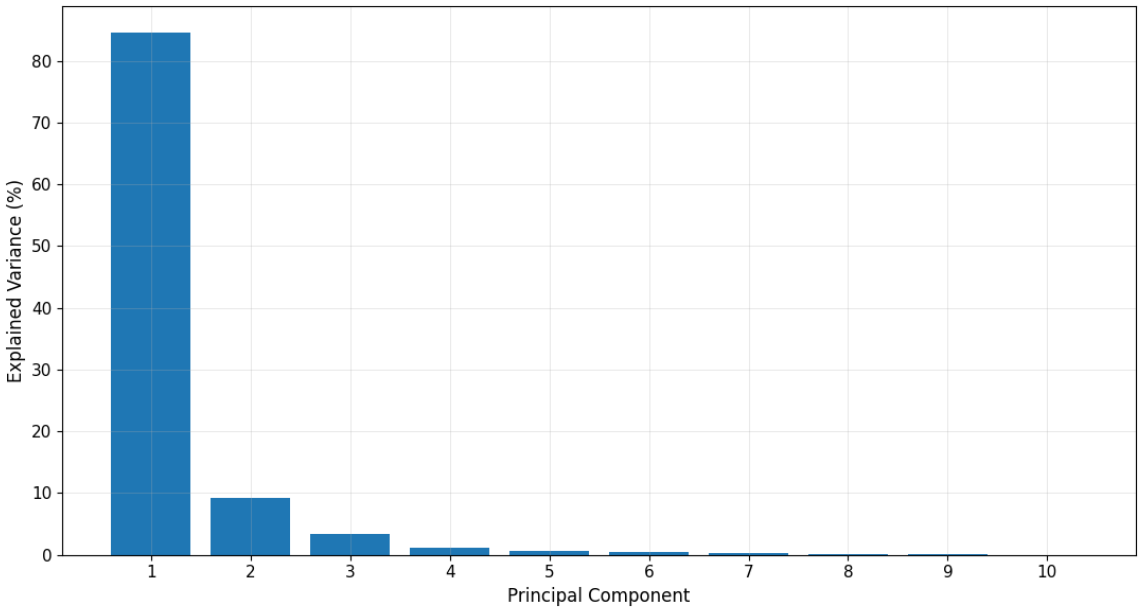


Figure 4.8: Explained variance ratio of the first principal components.

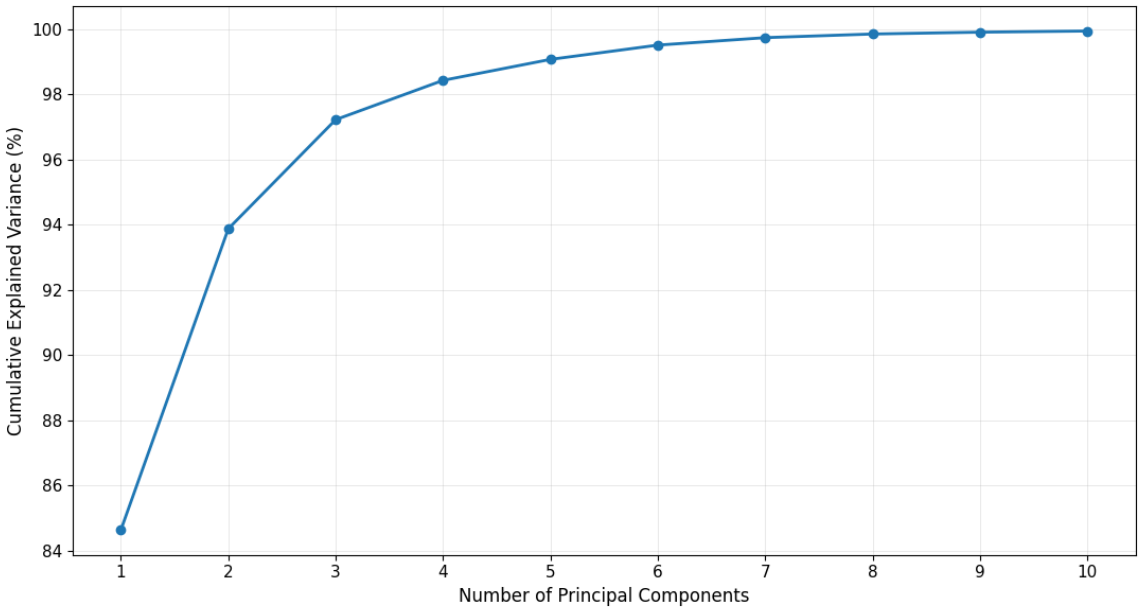


Figure 4.9: Cumulative explained variance as a function of the number of principal components.

The results reveal a very strong concentration of variance within the first principal components. The first principal component alone explains 84.63% of the total spectral variance, while the second and third components explain an additional 9.24% and 3.35%, respectively. The contribution of subsequent components decreases rapidly, with each component accounting for less than 1.5% of the remaining variance.

This behaviour is characteristic of hyperspectral datasets, where adjacent wavelengths are often highly correlated and therefore contain a large amount of redundant information. As a result, a large fraction of the original spectral variability can be represented using only a limited number of principal components.

The cumulative explained variance further highlights this redundancy. The first two principal components already account for 93.87% of the total variance, while the first three components explain 97.22%. When considering the first five principal components, 99.07% of the original spectral variance is retained.

Based on these results, the subsequent PCA analysis focused on the first five principal components. This choice provides an excellent compromise between dimensionality reduction and information preservation, while avoiding the inclusion of higher-order components that contribute only marginally to the overall spectral variability.

These observations confirm that substantial dimensionality reduction can be achieved without major information loss. However, it is important to note that the variance captured by PCA is not necessarily related to ALD. Since PCA is an unsupervised technique, the principal components are selected solely according to their ability to

explain spectral variability rather than their predictive relevance for the target variable. This will be showed and discussed later.

To better understand the spectral information represented by these components, the corresponding loading coefficients were subsequently analysed.

4.4.3 Analysis of PCA Loadings

The loading coefficients quantify the contribution of each wavelength to a given principal component. In practical terms, a loading can be interpreted as the weight assigned to a spectral band in the linear combination defining the principal component.

The magnitude of a loading reflects the importance of the corresponding wavelength. Bands associated with large absolute loading values contribute more strongly to the spectral pattern represented by the principal component, whereas bands with loadings close to zero have only a limited influence.

The sign of the loading indicates the direction of the contribution. Wavelengths with positive loadings increase the principal component score, whereas wavelengths with negative loadings decrease it.

The loading coefficients associated with the first five principal components are presented in Figure 4.10. Since the first five components explain more than 99% of the total spectral variance, they were considered sufficient to characterize the dominant spectral patterns present within the dataset.

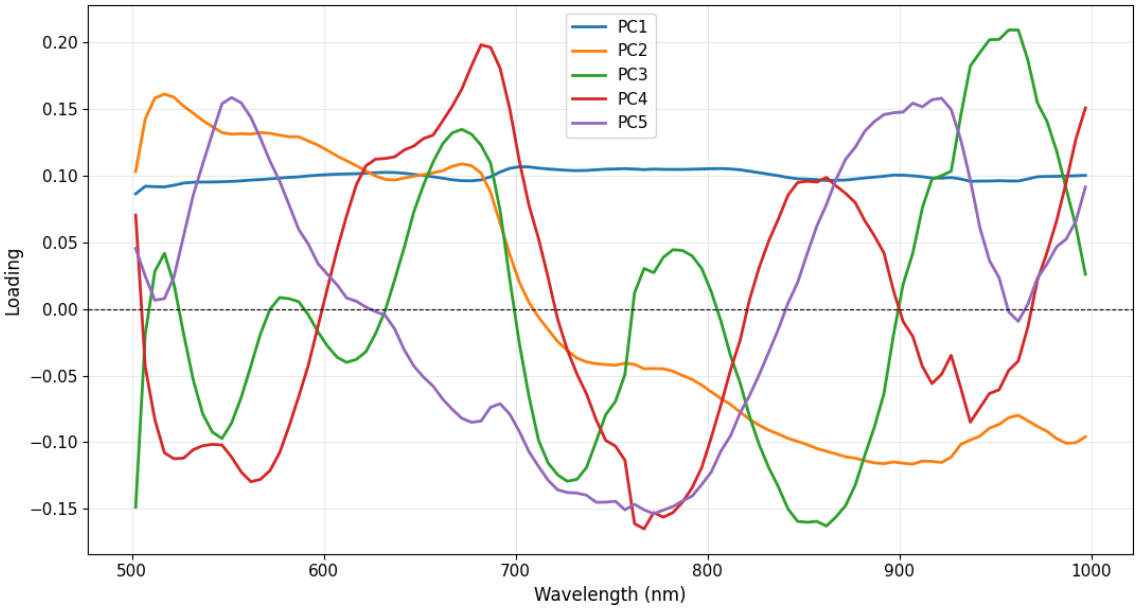


Figure 4.10: Loading coefficients of the first five principal components as a function of wavelength.

A clear distinction can be observed between PC1 and the higher-order components. The loading coefficients of PC1 remain relatively uniform across the entire spectral range, indicating that this component primarily captures overall reflectance variations affecting most wavelengths simultaneously. This observation is consistent with the dominant contribution of PC1 to the total explained variance (84.63%).

In contrast, PC2 to PC5 exhibit considerably larger fluctuations and multiple sign changes throughout the spectrum. These components therefore capture localized spectral variations and contrasts between different wavelength regions. Several spectral regions display pronounced loading magnitudes, particularly within the green visible domain (approximately 540–560 nm), the red region (approximately 670–690 nm), and parts of the near-infrared spectrum between 850 and 950 nm.

The presence of strong positive and negative loading values indicates that the corresponding principal components emphasize differences between spectral regions rather than overall reflectance intensity. Consequently, wavelengths associated with large loading magnitudes are expected to contribute more strongly to the dominant spectral variability captured by the PCA.

The loading analysis therefore provides a basis for identifying wavelengths that contribute most significantly to the principal components. To quantify this contribution and derive a reduced subset of spectral bands, a loading-based band importance metric was computed [60].

4.4.4 PCA-Based Band Selection

The loading analysis presented in the previous section revealed that several wavelength regions contributed strongly to the higher-order principal components. To quantify the overall contribution of each spectral band, a loading-based importance metric was computed.

Since both positive and negative loadings indicate strong contributions to a principal component, the absolute values of the loadings were considered. Furthermore, only PC2 to PC5 were included in the analysis. PC1 was excluded because its loading coefficients remained uniform across the spectral range and primarily reflected overall reflectance variations rather than localized spectral features. However, absolute loading sum has also been computed with PC1-PC5, but as it only resulted in a simple upward translation on the plot, PC1 hasn't been taken into account.

The importance score associated with wavelength (j) was defined as:

$$I_j = \sum_{k=2}^{5} |L_{jk}| \tag{4.12}$$

where (L_{jk}) denotes the loading coefficient of wavelength (j) for principal component (k).

The resulting wavelength importance scores are presented in Figure 4.11.

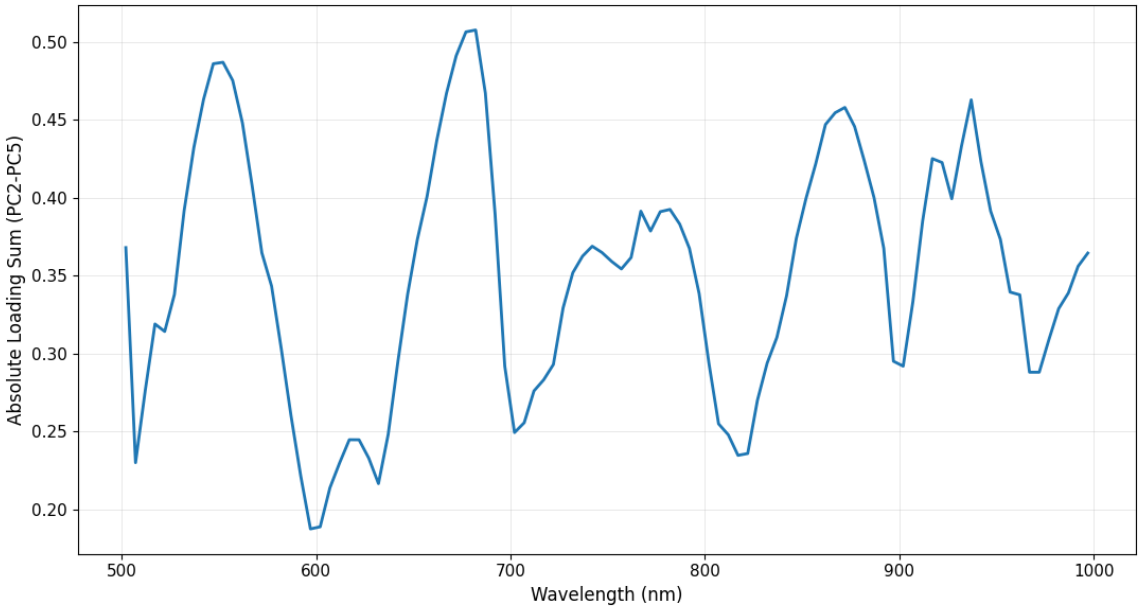


Figure 4.11: Band importance derived from the absolute loading sum of PC2–PC5.

Several wavelength regions exhibit consistently high importance values. The strongest contributions are observed around 540–560 nm, 670–690 nm, and within the near-infrared region between approximately 860 and 940 nm. These regions correspond closely to the spectral domains that displayed large loading magnitudes in the previous analysis.

The highest-ranked wavelength was located at 682 nm, followed by neighboring bands around 677 nm and 672 nm. Additional highly ranked wavelengths were identified around 552 nm and within the near-infrared region near 870–940 nm. Rather than selecting isolated wavelengths, the PCA therefore highlights broader spectral regions that contribute strongly to the dominant spectral variability of the dataset.

It is important to note that the PCA-based ranking differs from the wavelength ranking obtained through the correlation analysis presented earlier. While the correlation analysis identifies wavelengths that are most strongly related to ALD, PCA identifies wavelengths that contribute most to the overall spectral variance of the dataset. Consequently, wavelengths selected by PCA are not necessarily those exhibiting the

strongest relationship with ALD.

The resulting wavelength ranking was subsequently used to construct reduced spectral subsets that were evaluated within the Random Forest framework. This allowed the effectiveness of PCA-based dimensionality reduction to be compared with alternative feature selection strategies.

Chapter 5

Random Forest Modeling

5.1 Methodology

Following the exploratory analyses presented in the previous sections, Random Forest (RF) regression was used to evaluate the predictive capability of the hyperspectral data for Active Layer Depth (ALD) estimation. Unlike spectral correlation analysis or PCA, Random Forest is a supervised learning method, meaning that the model is trained directly using the measured ALD values as the target variable.

Random Forest was selected because it is well suited for high-dimensional remote sensing datasets, where many predictor variables may be correlated. Previous studies on permafrost ALT estimation using hyperspectral data successfully applied RF-based approaches and demonstrated the relevance of machine learning methods for upscaling field measurements using spectral information [82] [83]. In this study, RF was therefore used as the main modeling framework to compare the predictive value of different spectral datasets and feature selection strategies.

Random Forest is an ensemble method composed of multiple decision trees. A decision tree recursively partitions the predictor space into smaller regions by selecting split thresholds that reduce the prediction error [7]. For regression problems, the split at each node is generally chosen to minimize the mean squared error within the resulting child nodes. For a node containing N samples, the mean squared error can be written as:

$$MSE = \frac{1}{N} \sum_{i=1}^{N} (y_i - \bar{y})^2 \tag{5.1}$$

where y_i is the observed ALD value of sample i, and $\bar{y}$ is the mean ALD value within

the node.

In a Random Forest, each tree is trained using a bootstrap sample drawn from the original dataset. In addition, at each split, only a random subset of predictor variables is considered. This combination of bootstrap sampling and random feature selection reduces the correlation between individual trees and improves the generalization ability of the model.

For a regression problem, the final Random Forest prediction is obtained by averaging the predictions of all individual trees:

$$\hat{y} = \frac{1}{T} \sum_{t=1}^{T} \hat{y}_t \tag{5.2}$$

where T is the total number of trees in the forest and $\hat{y}_t$ is the prediction produced by tree t.

The number of trees was set to 500, and the number of candidate variables considered at each split was defined as the square root of the total number of predictors. A fixed random seed was used to ensure reproducibility of the results.

Model performance was assessed using a 10-fold cross-validation procedure. The dataset was randomly divided into ten subsets of approximately equal size. At each iteration, nine subsets were used for training and the remaining subset was used for validation. This process was repeated ten times so that each observation was used once for validation. The final performance metrics were computed from the cross-validated predictions.

A 10-fold cross-validation strategy was selected because it provides a good compromise between bias and variance in performance estimation while maintaining a sufficient number of training samples in each fold. This approach is widely used in machine learning studies and is particularly suitable for relatively small datasets such as the one considered in this work [37].

Model performance was evaluated using several complementary statistical metrics. The Pearson correlation coefficient (r) was first computed between observed and predicted ALD values:

$$r = \frac{\sum_{i=1}^{n}(y_i - \bar{y})(\hat{y}_i - \bar{\hat{y}})}{\sqrt{\sum_{i=1}^{n}(y_i - \bar{y})^2}\sqrt{\sum_{i=1}^{n}(\hat{y}_i - \bar{\hat{y}})^2}} \tag{5.3}$$

where y_i represents the observed ALD values, $\hat{y}_i$ the predicted ALD values, and $\bar{y}$ and $\bar{\hat{y}}$ their respective means.

The Pearson correlation coefficient was included to facilitate comparison with the correlation analyses presented in previous sections and with values commonly reported in the literature. Values of r close to 1 indicate a strong agreement between observations and predictions, whereas values close to 0 indicate little predictive relationship.

Four complementary metrics were used to evaluate model performance. Two different R^2 metrics are reported throughout this study.

The first metric, referred to as **Global** R^2, corresponds to the classical coefficient of determination. It is computed by training and testing the model on the entire dataset simultaneously:

$$R^2 = 1 - \frac{\sum_{i=1}^{n}(y_i - \hat{y}_i)^2}{\sum_{i=1}^{n}(y_i - \bar{y})^2} \tag{5.4}$$

where y_i is the observed Active Layer Depth, $\hat{y}_i$ is the value predicted by the model trained on the full dataset, $\bar{y}$ is the mean observed Active Layer Depth, and n is the total number of samples.

The second metric, referred to as **Mean CV** R^2, evaluates the model's generalization capability. It is obtained by averaging the individual R^2 values computed independently for each validation fold:

$$R^2_{\text{CV}} = \frac{1}{K}\sum_{k=1}^{K} R^2_k \tag{5.5}$$

where K is the number of cross-validation folds and R^2_k is the coefficient of determination obtained for fold k using only its out-of-fold validation data.

Because Mean CV R^2 assesses model performance independently on each validation subset, it is highly sensitive to fold-to-fold variability, thus providing a more conservative and realistic estimate of model robustness. In contrast, Global R^2 reflects the model's capacity to fit the training data and generally produces higher values due to the absence of data splitting.

Both the Pearson correlation coefficient (r) and the coefficient of determination (R^2) were used throughout this study to evaluate model performance. In fact, to facilitate the comparison with the reference study article [82] (which is using r to show their results) the Pearson correlation coefficient will be used. Additionally, R^2 is commonly used and although these metrics are related, they provide complementary information. The Pearson correlation coefficient measures the strength of the relationship between observed and predicted ALD values and facilitates comparison with the correlation analyses presented in previous sections as well as with values commonly reported in

the literature. In contrast, (R^2) quantifies the proportion of the observed variance explained by the model and therefore provides a more direct measure of predictive accuracy. Consequently, both metrics are reported throughout this work in order to provide a comprehensive assessment of model performance.

The Root Mean Square Error (RMSE) was computed as:

$$RMSE = \sqrt{\frac{1}{n}\sum_{i=1}^{n}(y_i - \hat{y}_i)^2} \tag{5.6}$$

and the Mean Absolute Error (MAE) was computed as:

$$MAE = \frac{1}{n}\sum_{i=1}^{n}|y_i - \hat{y}_i| \tag{5.7}$$

These metrics provide complementary information: R^2 measures the proportion of ALD variance explained by the model, while RMSE and MAE quantify the prediction error in the original ALD units.

Several predictor datasets were evaluated using the same RF framework. These included the complete hyperspectral dataset, reduced subsets of spectral bands selected using correlation analysis, PCA-based band selection, vegetation indices, multispectral variables, and combinations of hyperspectral and LiDAR-derived information. Different spatial extraction strategies were also tested, including pixel values, 2 m buffers, and 5 m buffers.

Finally, RF feature importance scores were used to rank the spectral bands according to their contribution to ALD prediction. These rankings were then used in a sensitivity analysis, where RF models were trained using different numbers of top-ranked bands. This allowed the influence of spectral dimensionality on model performance to be evaluated.

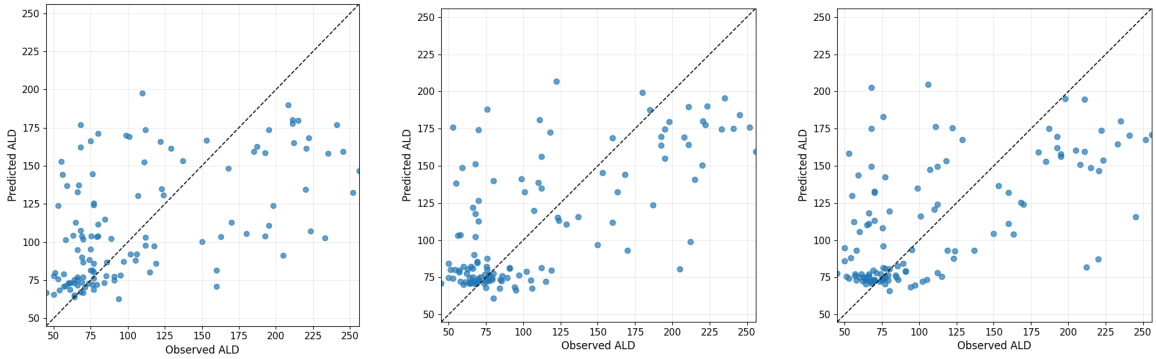
5.2 Full Hyperspectral Random Forest Model

Before investigating feature selection strategies and the integration of additional predictor variables, a baseline Random Forest (RF) model was developed using the complete hyperspectral dataset (100 spectral bands). The objective of this initial analysis was to evaluate the predictive capability of the hyperspectral observations and assess the influence of the spatial extraction strategy on model performance. As mentioned before, the 2 m buffer first analyses gave some hints that it was better performing, in

this section Random Forest will effectively demonstrate it again.

Three datasets were considered: pixel-level spectral values, a 2 m buffer average, and a 5 m buffer average. Model performance was evaluated using the Pearson correlation coefficient (r), the coefficient of determination (R^2), the root mean square error (RMSE), and the mean absolute error (MAE). In addition, the mean cross-validation R^2 and its standard deviation were computed to assess the stability of the model across the different folds.

Figure 5.1 presents the relationship between observed and predicted ALD values for the three extraction strategies.



(a) Pixel (b) Buffer 2 m (c) Buffer 5 m

Figure 5.1: Observed versus predicted ALD values obtained using Random Forest models trained with the complete hyperspectral dataset for the three spatial extraction strategies.

Table 5.1 summarizes the corresponding performance metrics.

Table 5.1: Baseline Random Forest performance obtained using all hyperspectral bands for the three spatial extraction strategies.

Dataset	r	R^2	Mean CV R^2	RMSE (cm)	MAE (cm)
Pixel	0.541	0.282	0.241 ± 0.321	49.4	37.3
Buffer 5 m	0.599	0.353	0.255 ± 0.276	46.8	34.6
Buffer 2 m	**0.690**	**0.475**	$\mathbf{0.398 \pm 0.320}$	**42.2**	**31.0**

The results indicate that the spatial extraction strategy has a significant impact on model performance. Among the three approaches, the 2 m buffer consistently produced the best results across all evaluation metrics. The highest predictive performance was obtained for this dataset, with a Pearson correlation coefficient of $r = 0.690$ and a coefficient of determination of $R^2 = 0.475$. In addition, the 2 m buffer yielded the lowest prediction errors, with an RMSE of 42.2 cm and an MAE of 31.0 cm.

The pixel-level extraction exhibited the weakest performance. This result is likely related to the increased sensitivity of individual pixels to local spectral variability, geolocation uncertainties, and small-scale environmental heterogeneity. Such effects introduce additional noise into the predictor variables and reduce the ability of the model to identify robust relationships with ALD.

Applying a spatial averaging procedure improved the predictive performance of the RF model. The 5 m buffer produced higher values of r and R^2 than the pixel-based extraction, indicating that part of the local spectral noise was successfully reduced. However, its performance remained inferior to that of the 2 m buffer. This suggests that the larger averaging window may introduce excessive spatial smoothing, thereby reducing the sensitivity of the spectral measurements to local variations in active layer depth.

Although the 2 m buffer achieved the highest performance, the obtained metrics remain moderate. The value of $R^2 = 0.475$ indicates that less than half of the variance in ALD can be explained by the hyperspectral predictors alone. Similarly, the observed scatter in Figure 5.1 reveals that substantial prediction errors remain, particularly for larger ALD values, which tend to be underestimated by the model. Consequently, while hyperspectral information contains useful information related to ALD variability, the predictive relationship remains relatively weak and additional feature selection strategies are required to improve model performance.

Given the superior performance of the 2 m buffer dataset, all subsequent analyses involving dimensionality reduction, feature selection, and model optimization were primarily conducted using this extraction strategy.

5.3 Feature Importance and Band Selection

The Random Forest full model analysis demonstrated that hyperspectral information contains predictive information related to ALD variability. However, the use of the complete hyperspectral dataset involves 100 highly correlated spectral bands, many of which contain redundant information due to the strong spectral continuity of reflectance measurements. Such redundancy may increase model complexity, amplify the influence of noise, and reduce the interpretability of the resulting model.

Consequently, several feature reduction strategies were investigated in order to identify a more compact set of predictor variables while preserving the predictive capability of the Random Forest model. In addition to potentially improving model robustness, reducing the number of input variables may facilitate the identification of the spectral

regions that are most relevant to ALD prediction.

Two different approaches were evaluated. Firstly, Principal Component Analysis (PCA) was used to transform the original spectral bands into a reduced set of components containing most of the spectral variance.

Secondly, feature importance scores derived directly from the Random Forest model were used to identify the most influential wavelengths and evaluate the possibility of reducing the number of spectral bands while maintaining model performance.

5.3.1 Principal Component Analysis

5.3.1.1 Random Forest Using Principal Components

To evaluate whether the dimensionality of the hyperspectral dataset could be reduced without compromising predictive performance, the principal components derived from the PCA were used directly as input variables for the Random Forest model. Based on the cumulative explained variance analysis presented previously, the first five principal components were initially selected, as they account for more than 99% of the total variance contained in the original 100-band dataset.

An additional model was trained using the first 10 principal components (99.94% of the total variance) to assess whether retaining a larger proportion of the transformed feature space could further improve predictive performance. Table 5.2 summarizes the obtained results.

Table 5.2: Random Forest performance obtained using PCA components as input variables.

Model	r	R^2	Mean CV R^2	RMSE (cm)	MAE (cm)
100 bands	0.690	0.475	0.398	42.17	30.95
5 PCs	0.688	0.469	0.406	42.41	30.80
10 PCs	0.693	0.452	0.391	43.09	33.30

The results demonstrate that PCA provides an effective dimensionality reduction strategy for hyperspectral ALD prediction. Using only the first five principal components, corresponding to more than 99% of the total spectral variance, resulted in predictive performances nearly identical to those obtained using the complete set of 100 spectral bands.

In particular, the model based on five principal components achieved a Pearson correlation coefficient of $r = 0.688$ and a coefficient of determination of $R^2 = 0.469$, compared

to $r = 0.690$ and $R^2 = 0.475$ for the full hyperspectral dataset. The corresponding RMSE and MAE values also remained nearly unchanged.

These results indicate that a substantial degree of redundancy exists within the hyperspectral dataset. Most of the information relevant to ALD prediction can therefore be represented using a small number of orthogonal variables without significant loss of predictive capability.

5.3.1.2 PCA-Guided Band Selection

Although the PCA transformation successfully reduced the dimensionality of the predictor space, an additional analysis was conducted to investigate whether the original hyperspectral dataset could be reduced through wavelength selection. For this purpose, the absolute loading sums derived from the first principal components were used to identify the wavelengths contributing most strongly to the PCA representation.

Based on this analysis, subsets containing the 10 and 20 most influential wavelengths were selected and used as input variables for the Random Forest model.

Table 5.3: Random Forest performance obtained using wavelengths selected from PCA loadings.

Model	r	R^2	Mean CV R^2	RMSE (cm)	MAE (cm)
100 bands	0.690	0.475	0.398	42.17	30.95
Top 20 PCA bands	0.593	0.339	0.219	47.29	34.58
Top 10 PCA bands	0.574	0.305	0.182	48.51	34.80

In contrast to the PCA component approach, selecting individual wavelengths based on PCA loadings resulted in a substantial decrease in predictive performance. Both the 10-band and 20-band subsets produced significantly lower values of r and R^2 compared to the full hyperspectral dataset.

This outcome highlights an important distinction between dimensionality reduction through component transformation and wavelength selection based on loading magnitude. PCA is designed to maximize the variance explained within the predictor space rather than the predictive relationship with the target variable. Consequently, wavelengths contributing strongly to the overall spectral variance are not necessarily the wavelengths containing the most relevant information for ALD prediction [58].

The results therefore suggest that PCA constitutes an effective feature transformation technique but is less suitable as a standalone wavelength selection strategy in the present application.

5.3.2 Random Forest Feature Importance

While PCA provides an effective dimensionality reduction strategy through feature transformation, the resulting principal components remain difficult to interpret physically since each component represents a combination of all original wavelengths. Consequently, an additional analysis was performed using the feature importance scores derived directly from the Random Forest model. Unlike PCA, which identifies directions of maximum spectral variance, Random Forest feature importance quantifies the contribution of each predictor to the predictive performance of the model [49].

Figure 5.2 presents the variation of feature importance as a function of wavelength for the baseline Random Forest model trained on the complete hyperspectral dataset. Several distinct patterns can be observed. First, the distribution of importance values is highly non-uniform, indicating that the predictive information relevant to ALD is concentrated within specific spectral regions rather than being evenly distributed across the spectrum.

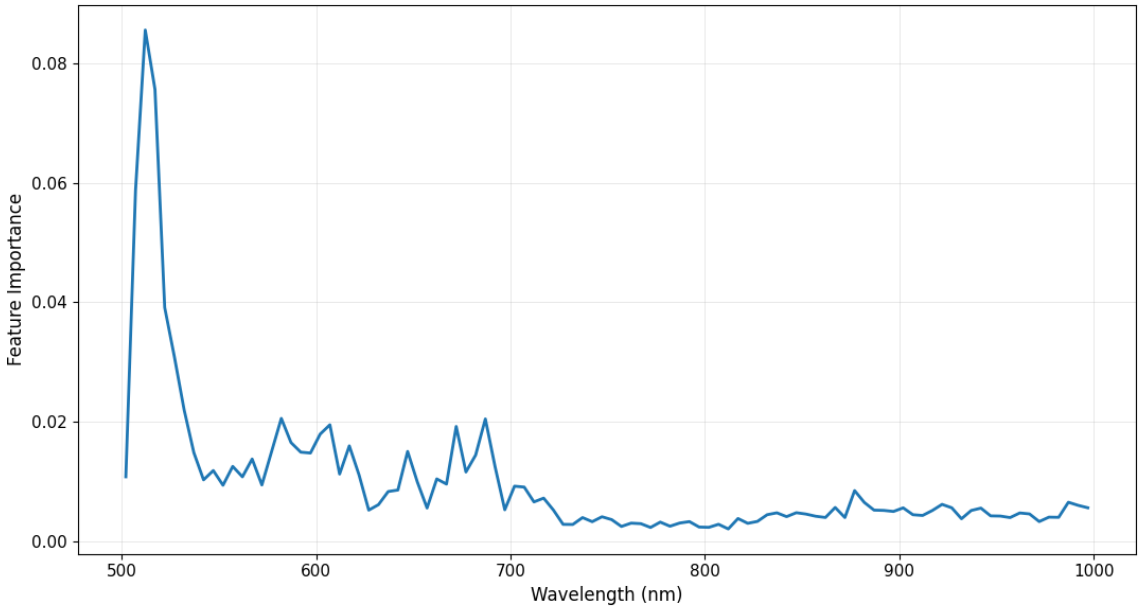


Figure 5.2: Random Forest feature importance as a function of wavelength for the 2 m buffer dataset.

The most prominent feature corresponds to a strong peak located near 512 nm. This wavelength exhibits an importance substantially larger than any other band in the dataset, suggesting that it contains particularly valuable information for ALD prediction. Additional local maxima are observed within the visible region, notably around 580–610 nm and 660–690 nm. In contrast, wavelengths located in the near-infrared region generally exhibit lower and more homogeneous importance values.

Some of the spectral regions identified by the Random Forest model are somewhat consistent with the patterns previously observed in the Pearson correlation analysis (same best performing band and decrease at higher wavelengths). This convergence suggests that these wavelengths are not selected randomly by the model but correspond to spectral regions that consistently contain information related to active layer depth variability.

To further investigate the relationship between PCA-based and Random Forest-based feature selection, the wavelengths identified as most important by both approaches were compared. Figure 5.3 contrasts the cumulative PCA loading contributions with the twenty most important wavelengths selected by the Random Forest model.

Although several RF-selected wavelengths are located within spectral regions exhibiting elevated PCA loading contributions, the correspondence between both approaches is far from perfect. The PCA loading analysis highlights wavelengths that contribute strongly to the overall spectral variance structure, whereas Random Forest importance quantifies the direct contribution of each wavelength to ALD prediction. Consequently, wavelengths associated with high spectral variability are not necessarily those providing the greatest predictive information for the target variable.

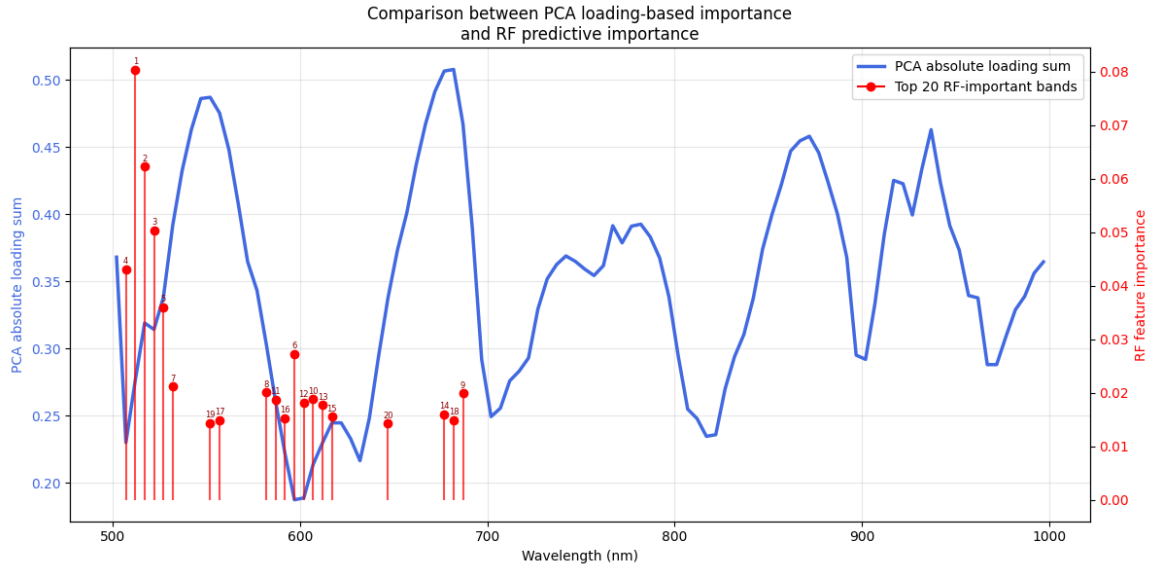


Figure 5.3: Comparison between PCA absolute loading sum and the top20 most important RF bands.

This observation is consistent with the performance results obtained in the previous section. While PCA component transformation successfully preserved predictive performance, selecting wavelengths solely on the basis of PCA loadings resulted in a noticeable decrease in model accuracy. The Random Forest feature importance therefore appears to provide a more task-oriented criterion for wavelength selection,

as it directly evaluates the predictive relevance of each spectral band rather than its contribution to overall spectral variance.

The concentration of predictive information within a limited number of spectral regions also indicates that a substantial degree of redundancy exists within the original hyperspectral dataset. Since many adjacent wavelengths contain highly correlated information, it is reasonable to investigate whether similar or even improved predictive performances can be achieved using only a subset of the most informative bands. This hypothesis is evaluated in the following section through a progressive feature selection analysis.

5.3.3 Band Selection Performance

To assess whether all hyperspectral bands were necessary for ALD prediction, the wavelengths were ranked according to their Random Forest feature importance scores. Models were subsequently trained using progressively larger subsets of the most important bands, ranging from three wavelengths to the complete 100-band dataset.

The results are summarized in Table 5.4 and Figure 5.4. A clear and consistent trend can be observed across all evaluation metrics. Rather than decreasing, model performance initially improved as the number of predictor variables was reduced. This behavior suggests that a substantial fraction of the original hyperspectral dataset contains redundant or noisy information that does not contribute positively to the predictive relationship between spectral measurements and ALD.

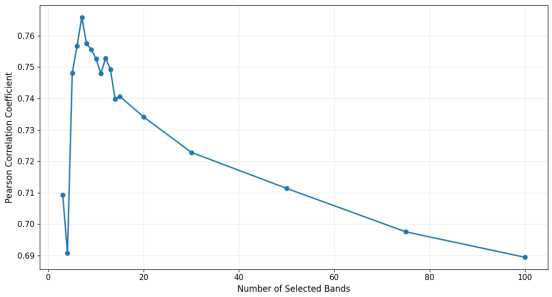
The highest predictive performance was obtained using only seven wavelengths. This reduced model achieved a Pearson correlation coefficient of $r = 0.766$, a global coefficient of determination of $R^2 = 0.586$, and a mean cross-validated coefficient of determination of $R^2 = 0.535$. In addition, the corresponding RMSE and MAE values decreased to 37.4 cm and 27.2 cm respectively. These values represent a significant improvement compared to the baseline model trained on the complete hyperspectral dataset.

Remarkably, the seven-band model outperformed the full 100-band model across all evaluation metrics. The Pearson correlation coefficient increased from 0.689 to 0.766, while the RMSE decreased from 42.2 cm to 37.4 cm. Similar improvements were observed for both the global and cross-validated coefficients of determination. Such results demonstrate that removing less informative wavelengths can improve model generalization by reducing the influence of redundant predictors and limiting overfitting effects [57].

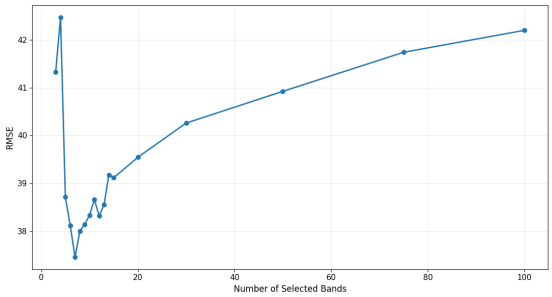
The performance curves further reveal that predictive accuracy remains relatively sta-

ble for feature subsets containing approximately five to ten wavelengths. Beyond this range, the progressive addition of lower-ranked bands results in a gradual decline in performance. This behavior strongly suggests that the information most relevant for ALD prediction is concentrated within a limited number of spectral regions, while many additional wavelengths contribute little useful information.

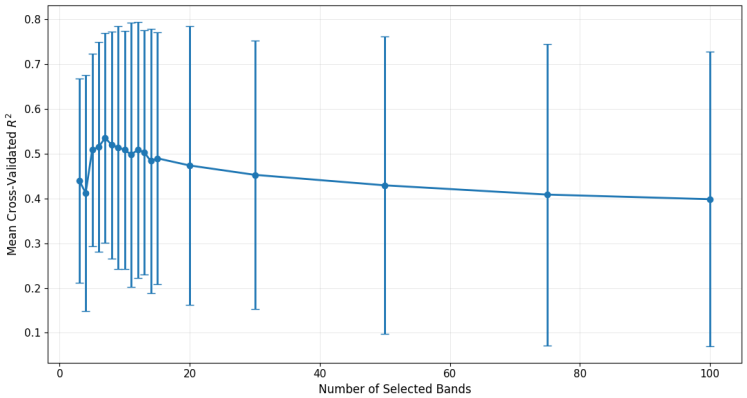
These findings constitute one of the most important results of this study. Although the original hyperspectral dataset contained 100 spectral bands, the Random Forest analysis indicates that only a small subset of carefully selected wavelengths is required to achieve optimal predictive performance. This result has important practical implications, as it suggests that future ALD monitoring efforts could potentially rely on a reduced set of strategically selected wavelengths without compromising predictive accuracy.



(a) Pearson correlation coefficient.



(b) RMSE.



(c) Mean cross-validated R^2.

Figure 5.4: Evolution of model performance as a function of the number of selected bands.

Table 5.4: Random Forest performance for selected feature subset sizes.

Number of bands	r	Global R^2	Mean CV R^2	RMSE (cm)	MAE (cm)
3	0.709	0.495	0.440	41.33	29.85
5	0.748	0.558	0.508	38.71	28.17
6	0.757	0.571	0.515	38.12	27.91
7	**0.766**	**0.586**	**0.535**	**37.45**	**27.16**
10	0.753	0.566	0.509	38.33	27.64
20	0.734	0.538	0.474	39.54	28.39
50	0.711	0.505	0.429	40.92	30.15
100	0.689	0.474	0.398	42.20	30.93

Although the feature selection procedure resulted in a substantial improvement in predictive performance, the obtained results should still be interpreted with caution. Even for the optimal seven-band model, the prediction error remains relatively large, with an RMSE of approximately 37 cm. Considering the range of observed ALD values within the study area, this indicates that important prediction errors remain for a number of sampling locations.

Similarly, the cross-validation results reveal a non-negligible variability between folds. While the seven-band model achieved the highest mean cross-validated coefficient of determination ($R^2 = 0.535$), the associated standard deviation remained relatively high (± 0.235). This observation indicates that model performance might still be sensitive to the specific composition of the training and validation subsets. This will be analyzed later.

5.4 Integration of DEM Information

The previous analyses demonstrated that hyperspectral information contains valuable predictive information related to active layer depth. However, ALD is not controlled exclusively by surface spectral characteristics. Topographic conditions may also influence permafrost dynamics.

To investigate whether topographic information could provide complementary predictive information, Digital Elevation Model (DEM) variables were integrated into the Random Forest framework. The objective was to determine whether the combination of spectral and topographic predictors could improve ALD estimation compared to hyperspectral information alone.

Figure 5.5 presents the resulting feature importance distribution.

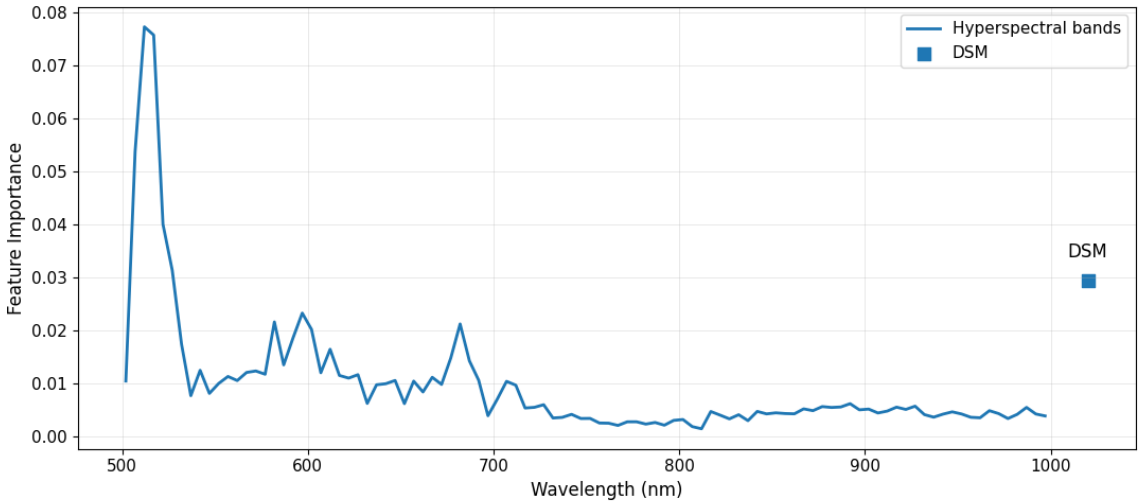
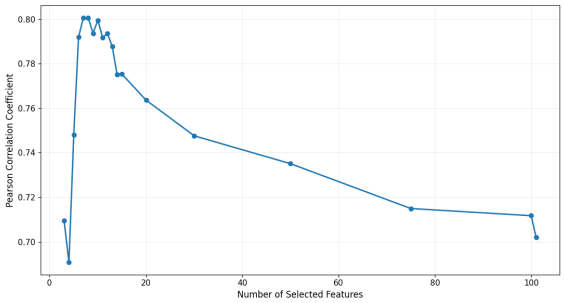


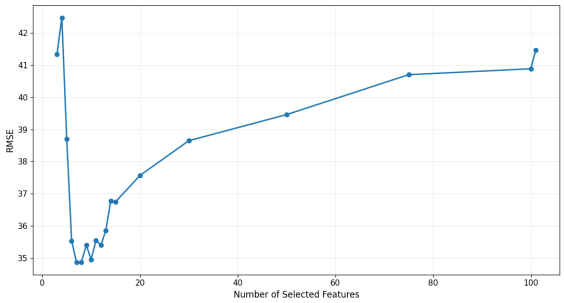
Figure 5.5: Random Forest feature importance obtained using hyperspectral bands and DEM information.

Although several hyperspectral wavelengths remain among the most influential predictors, the DEM variable exhibits a relatively high importance score compared to the majority of spectral bands. This observation suggests that topographic information contributes meaningful predictive information that is not fully captured by spectral reflectance measurements alone.

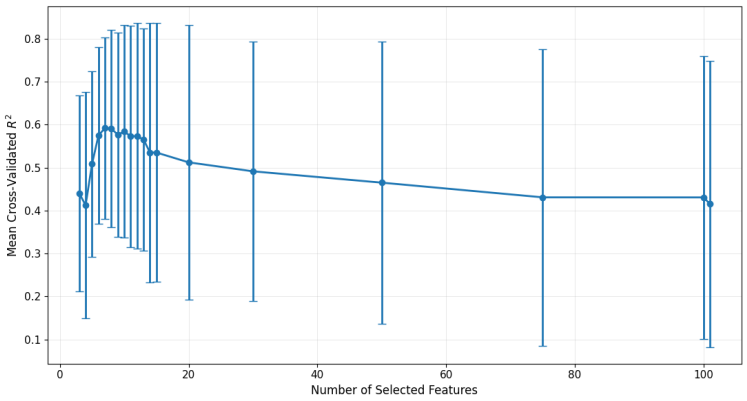
The influence of DEM integration on model performance is summarized in Figure 5.6 and Table 5.5. Similar to the hyperspectral-only analysis, model performance initially improved as less informative variables were removed. The optimal performance was obtained using a reduced subset of seven features, including the DEM variable.



(a) Pearson correlation coefficient.



(b) RMSE.



(c) Mean cross-validated R^2.

Figure 5.6: Evolution of model performance as a function of the number of selected hyperspectral and DEM features.

Table 5.5: Comparison between the optimal hyperspectral model and the optimal hyperspectral + DEM model.

Model	r	Global R^2	Mean CV R^2	RMSE (cm)	MAE (cm)
HS only (7 bands)	0.766	0.586	0.535	37.45	27.16
HS + DEM (7 features)	**0.801**	**0.641**	**0.592**	**34.87**	**25.75**

The inclusion of DEM information resulted in a consistent improvement across all evaluation metrics. The Pearson correlation coefficient increased from 0.766 for the optimal hyperspectral-only model to 0.801 after DEM integration. Similarly, the mean cross-validated coefficient of determination increased from 0.535 to 0.592. The global coefficient of determination also increased from 0.586 to 0.641, while the RMSE decreased from 37.4 cm to 34.9 cm.

These improvements indicate that the DEM provides complementary information relevant to ALD prediction. While hyperspectral measurements primarily characterize surface vegetation and soil properties, the DEM captures local topographic variability that influences hydrological and ecological processes affecting active layer development

[16]. The simultaneous improvement of all performance metrics strongly suggests that both information sources contribute independently to the prediction task.

Despite the observed improvement, the prediction error remains non-negligible and the cross-validation standard deviation remains relatively large. This indicates that a substantial fraction of the variability in ALD remains unexplained. Nevertheless, the DEM integration represents the most successful modeling configuration investigated this far and demonstrates the value of combining spectral and topographic information for permafrost monitoring applications.

5.5 Multispectral versus Hyperspectral Approaches

While hyperspectral sensors provide detailed spectral information, they are generally more expensive, generate larger datasets, and require more complex processing workflows than multispectral systems. Consequently, it is important to assess whether the additional spectral resolution effectively translates into improved ALD prediction performance.

To address this question, the performance of the optimal hyperspectral Random Forest models was compared with equivalent models trained using a reduced multispectral feature set. The obtained results were also compared with those reported in the reference study [83] in order to place the present work within the context of existing literature.

To evaluate the added value of hyperspectral imagery for ALD prediction, an equivalent Random Forest workflow was applied to both multispectral and hyperspectral datasets. Importantly, the same field observations, validation strategy, Random Forest parameters, and performance metrics were used throughout the analysis. Consequently, any differences in predictive performance can be directly attributed to the information content of the spectral data rather than methodological differences.

The comparison between the different modelling configurations is presented in Table 5.6.

Table 5.6: Comparison between multispectral and hyperspectral Random Forest models.

Model	r	Global R^2	Mean CV R^2	RMSE (cm)	MAE (cm)
Multispectral	0.712	0.507	0.486	40.85	28.44
Multispectral + DEM	0.769	0.589	0.552	37.29	26.62
Hyperspectral (7 bands)	0.766	0.586	0.535	37.45	27.16
Hyperspectral + DEM	**0.801**	**0.641**	**0.592**	**34.87**	**25.75**

The multispectral model achieved a Pearson correlation coefficient of $r = 0.712$ and a mean cross-validated coefficient of determination of $R^2 = 0.486$. Although these results already indicate a reasonable predictive capability, they remained below those obtained using the optimised hyperspectral model, which achieved $r = 0.766$ and a mean cross-validated R^2 of 0.535.

The integration of DEM information improved the performance of both approaches. For the multispectral dataset, the mean cross-validated coefficient of determination increased from 0.486 to 0.552, while the RMSE decreased from 40.8 cm to 37.3 cm. Similar improvements were observed for the hyperspectral models, where the inclusion of DEM information resulted in the best overall performance obtained in this study ($r = 0.801$, mean CV $R^2 = 0.592$, RMSE = 34.9 cm).

These results demonstrate that hyperspectral imagery consistently outperformed multispectral imagery, both with and without DEM integration. However, the performance gap remained relatively moderate. This suggests that a substantial fraction of the predictive information is already captured by the broad multispectral bands. Nevertheless, the additional spectral resolution provided by the hyperspectral sensor resulted in measurable improvements across all evaluation metrics.

The feature importance analysis further supports this conclusion. As shown in Figures 5.7 and 5.8, the blue band was consistently identified as the most influential predictor in the multispectral models. This observation is fully consistent with the hyperspectral analysis, which highlighted wavelengths located around 510–530 nm as the most important predictors of ALD.

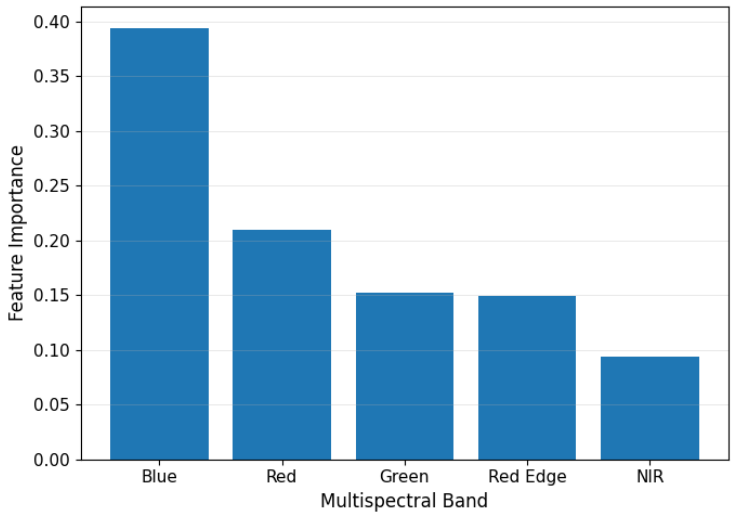


Figure 5.7: Feature importance obtained using the multispectral dataset.

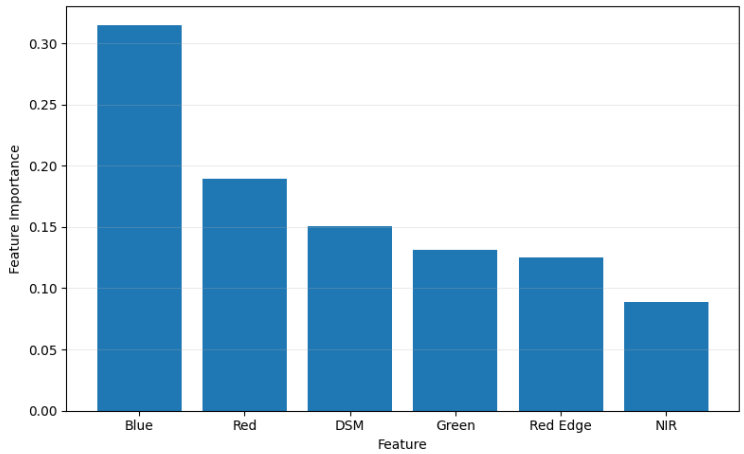


Figure 5.8: Feature importance obtained using the multispectral dataset combined with DEM information.

The agreement between the multispectral and hyperspectral analyses is particularly important. Independent methodologies, including Pearson correlation analysis, Random Forest feature importance and multispectral modeling, all identified the same portion of the spectrum as the most informative spectral region. This convergence strongly suggests that these wavelengths contain physically meaningful information related to active layer depth variability rather than statistical artefacts arising from the modeling process.

Overall, the results indicate that hyperspectral imagery provides a measurable advantage for ALD prediction. However, the improvement remains smaller than the gain obtained through DEM integration. This finding suggests that while detailed spectral information contributes positively to model performance, topographic information represents an equally important source of predictive information for active layer depth estimation.

From an operational perspective, the results indicate that multispectral imagery combined with DEM information can already provide satisfactory predictive performances. Nevertheless, the best results obtained in this study were achieved using a reduced hyperspectral feature set combined with DEM information. In conclusion, while hyperspectral datasets yield consistently superior predictive accuracy compared to multispectral imagery, this enhancement requires significantly higher computational costs, extensive preprocessing pipelines, and specialized feature optimization strategies to mitigate spectral noise.

5.6 Comparison with Hyperspectral Reference Study

The results obtained in this study were compared with those reported in the reference hyperspectral study [83](Table 5.7).

Table 5.7: Comparison between the results obtained in this study and those reported in the reference hyperspectral study.

Study	Data source	r	RMSE (cm)	MAE (cm)
Reference study (2014)	Hyperspectral	0.67	15.6	12.0
Reference study (2015)	Hyperspectral	0.64	15.6	12.3
Reference study (2019)	Hyperspectral	0.54	30.2	20.8
This study (100 bands)	Hyperspectral	0.689	42.2	30.9
This study (7 bands)	Hyperspectral	0.766	37.4	27.2
This study (6 bands + DEM)	Hyperspectral + DEM	**0.801**	**34.9**	**25.8**

Although both studies investigate active layer depth prediction from UAV-based hyperspectral imagery using Random Forest regression, the comparison should be interpreted with caution due to differences in study location, environmental conditions, hyperspectral sensors, field measurements, and processing workflows.

The reference study reported Pearson correlation coefficients ranging from 0.54 to 0.67 depending on the year of acquisition, with corresponding RMSE values between 15.6 cm and 30.2 cm. In the present work, correlation coefficients ranged from 0.689 for the baseline hyperspectral model to 0.801 for the optimized hyperspectral model integrating DEM information. While the RMSE values obtained here are larger than those reported in the literature, this difference must be interpreted in the context of the underlying ALT distributions.

The reference study considered ALT ranges of approximately 40–135 cm in 2014, 40–130 cm in 2015, and 50–225 cm in 2019, whereas the measurements used in this work ranged from approximately 50 cm to 250 cm. Because prediction errors generally increase with the variability and range of the target variable, larger RMSE values can be expected when modeling a broader distribution of active layer depths [78].

5.7 Model Validation and Robustness Analysis

The results presented in the previous sections were obtained using a 10-fold cross-validation framework. This validation strategy was selected in order to maximize the use of the available field observations while providing a more reliable estimate of

model performance than a single train-test split. Given the relatively limited number of sampling locations available for this study, a conventional approach could have produced performance estimates that were strongly dependent on the specific partition of the dataset. By contrast, cross-validation ensures that all observations are used for both training and validation while reducing the influence of a particular data split.

Beyond performance assessment, it is also important to evaluate the robustness of the conclusions derived from the Random Forest analysis. In particular, the identification of important wavelengths should not depend on a specific feature selection method or on the ordering of the spectral bands within the dataset. Similarly, the influence of specific landscape features, such as edge-effect areas, should be assessed to determine whether they bias the observed relationships between spectral information and active layer depth.

Several complementary analyses were therefore conducted. First, Recursive Feature Elimination with Cross-Validation (RFECV) was applied to independently identify the most informative predictors and compare them with the wavelengths selected through Random Forest feature importance. Second, a sensitivity analysis was performed to evaluate how model performance evolves as a function of the number of selected predictors. Additional tests were also conducted to verify that the identified spectral regions were not influenced by the ordering of the hyperspectral bands. Finally, the influence of edge-effect areas was investigated through both spectral signature analysis and dedicated modeling experiments.

5.7.1 Influence of Band Ordering

The feature importance analysis consistently identified wavelengths located at the beginning of the spectrum as the most informative predictors of active layer depth. The feature importance was then gradually decreasing as wavelength grows. Consequently, it was essential to verify that the algorithm was not artificially assigning importance weights based on the structural ordering of the bands.

To assess this possibility, the order of the hyperspectral bands was completely reversed prior to training the Random Forest model, thus starting with band 100 and finishing with band 1. The feature selection procedure was then repeated using this reordered dataset, and the performance metrics were compared with those obtained from the original configuration.

The results are summarized in Tables 5.8 and 5.9.

Table 5.8: Influence of hyperspectral band ordering on model performance.

Configuration	r	Mean CV R^2	Global R^2	RMSE (cm)
Original ordering	0.801	0.592	0.641	34.87
Reversed ordering	0.801	0.586	0.641	34.87

Table 5.9: Most important predictors identified using the original and reversed band ordering.

Original ordering	Reversed ordering
512 nm	512 nm
517 nm	517 nm
507 nm	507 nm
522 nm	522 nm
527 nm	527 nm
DEM	DEM
597 nm	532 nm

Reversing the order of the predictors produced basically completely identical model performances. The Pearson correlation coefficient remained equal to 0.801, the global coefficient of determination remained unchanged at 0.641, and the RMSE remained stable at approximately 34.9 cm. Only a very small decrease in the mean cross-validated coefficient of determination was observed, from 0.592 to 0.586.

In addition to the nearly identical performance metrics, the same spectral region was consistently identified as the most informative. The selected wavelengths remained concentrated within the green portion of the spectrum, while DEM information continued to be retained among the most important predictors. Minor differences were observed in the exact ranking of individual wavelengths (only the seventh band), which is not a big difference as importance differences are $<.001\%$. However, the overall conclusions remained unchanged.

These results demonstrate that the feature importance rankings obtained throughout this study are not influenced by the position of the predictors within the dataset. Instead, the identified wavelengths appear to be selected because of their genuine predictive relationship with active layer depth. Consequently, the spectral regions highlighted by the Random Forest analysis can be considered robust with respect to predictor ordering.

5.7.2 RFECV

All Random Forest models presented throughout this study were evaluated using a 10-fold cross-validation framework. This approach was adopted from the beginning of the analysis to maximize the use of the available field observations and to obtain performance estimates that are more robust than those derived from a single train-test split. Consequently, the reported performance metrics already reflect the model's ability to generalize to unseen data.

However, an important distinction must be made between model validation and feature selection. In the workflow adopted throughout this study, Random Forest feature importance was first computed using the complete dataset, after which the most important predictors were selected and evaluated through cross-validation. While the predictive performance itself was therefore assessed using independent validation folds, the feature selection step was performed beforehand using information from the entire dataset.

This introduces a potential source of selection bias. Because the selected predictors were identified prior to cross-validation, there remains a possibility that some wavelengths were favored due to characteristics specific to the available dataset. As a result, the corresponding performance estimates may be slightly optimistic [4].

Recursive Feature Elimination with Cross-Validation (RFECV) was therefore applied as an additional validation procedure. Unlike the previous approach, RFECV integrates feature selection directly within the cross-validation process. During each iteration, predictors are recursively removed and model performance is evaluated on validation folds that were not used for training. Consequently, both the selection of predictors and the estimation of predictive performance are performed within the same validation framework [28].

The objective of this analysis was not necessarily to obtain higher predictive performances, but rather to determine whether the wavelengths identified by the Random Forest feature importance analysis remain optimal when feature selection is performed under a more rigorous cross-validation scheme.

The RFECV procedure identified an optimal subset of nine predictors, consisting of eight hyperspectral bands and the DEM variable (Table 5.10).

Table 5.10: Predictors selected by RFECV.

Selected predictor
507 nm
512 nm
517 nm
522 nm
527 nm
532 nm
552 nm
592 nm
DEM

The selected wavelengths were concentrated between 507 nm and 592 nm, corresponding to the blue-green portion of the spectrum previously highlighted by the correlation analysis, Random Forest feature importance rankings, and band ordering validation.

The predictive performance obtained using the RFECV-selected features is summarized in Table 5.11.

Table 5.11: Comparison between the RF feature importance approach and RFECV.

Method	Features	r	Mean CV R^2	RMSE (cm)	MAE (cm)
RF feature importance	7	0.801	0.592	34.87	25.58
RFECV	9	0.799	0.586	34.99	25.36

The resulting model achieved a Pearson correlation coefficient of 0.799, a mean cross-validated coefficient of determination of 0.586, and an RMSE of 35.0 cm. These values are nearly identical to those obtained using the feature importance approach, which achieved a correlation coefficient of 0.801, a mean cross-validated R^2 of 0.592, and an RMSE of 34.9 cm.

The similarity between both sets of results is particularly important because RFECV performs feature selection within the cross-validation procedure itself, thereby reducing the risk of selection bias. The fact that RFECV independently identified nearly the same spectral region and produced almost identical predictive performances suggests that the wavelengths selected through the Random Forest feature importance analysis are not artifacts of the original feature selection procedure.

Furthermore, RFECV required substantially longer computation times than the feature importance approach, especially when applied to the full hyperspectral dataset. Given the negligible differences in predictive performance and the strong agreement

between the selected predictors, the Random Forest feature importance method was retained for the remainder of the analysis. This approach provides a considerably more computationally efficient solution while yielding essentially equivalent results.

Overall, the RFECV analysis confirms the robustness of the feature selection strategy adopted throughout this study and provides additional evidence that the blue-green spectral region, together with topographic information derived from the DEM, contains the most relevant information for active layer depth prediction.

5.7.3 Sensitivity Analysis

Throughout the previous analyses, model performance was evaluated using a 10-fold cross-validation framework with a fixed random state. This approach ensures full reproducibility of the results by generating the same partitioning of the dataset at each execution. However, although the observations are shuffled before the folds are created, the resulting partition remains identical for a given random state.

Consequently, all previously reported results were obtained using a single cross-validation configuration. While this is a common practice in machine learning studies, it raises the question of whether the identified wavelengths and associated performance metrics may be partially influenced by a particularly favorable partition of the dataset [43]. In other words, different random shuffles of the observations could potentially lead to very different feature rankings and model performances.

To investigate this possibility, a sensitivity analysis was conducted by repeating the complete feature selection procedure using ten different random states. Each random state generated a different 10-fold cross-validation partition, allowing the stability of the selected wavelengths and performance metrics to be evaluated across multiple validation configurations.

For each random state, Random Forest feature importance was first computed using the complete hyperspectral dataset and DEM information. The optimal number of predictors was then determined and the corresponding model performance was evaluated. The results obtained using the selected predictors were also compared with those obtained using the complete set of 100 hyperspectral bands and DEM information.

The results obtained for the different random states are summarized in Table 5.12.

Table 5.12: Sensitivity analysis results obtained using different random states for the cross-validation procedure.

Random State	Best N	r	Mean CV R^2	Global R^2	RMSE (cm)	MAE (cm)
5	10	0.805	0.586	0.648	34.54	25.16
10	9	0.797	0.628	0.635	35.15	25.67
42	7	0.801	0.592	0.641	34.87	25.58
100	10	0.800	0.554	0.640	34.91	25.40
123	10	0.798	0.601	0.637	35.05	25.17
309	8	0.808	0.587	0.651	34.36	24.69
538	8	0.790	0.532	0.624	35.66	26.04
767	6	0.808	0.613	0.653	34.30	24.66
999	6	0.794	0.554	0.630	35.40	25.49
2026	10	0.807	0.597	0.648	34.41	24.21

Although the optimal number of selected predictors varied between six and ten, model performances remained remarkably stable. The Pearson correlation coefficient ranged from 0.790 to 0.808, corresponding to a maximum variation of approximately 2.3% between the least and most favorable cross-validation configurations. Similarly, the mean cross-validated coefficient of determination remained within a relatively narrow interval, ranging from 0.532 to 0.628, while RMSE values varied only between 34.30 and 35.66 cm.

This stability indicates that the predictive performance of the proposed methodology is only weakly affected by the specific partitioning of the dataset. Consequently, the performance improvements observed throughout this study cannot be attributed to a particularly favorable cross-validation configuration.

The frequency of selection of each predictor is reported in Table 5.13.

Table 5.13: Frequency of selection of the best performing wavelengths across the ten tested random states.

Wavelength	Frequency
507 nm	10 / 10
512 nm	10 / 10
517 nm	10 / 10
522 nm	10 / 10
527 nm	10 / 10
DEM	10 / 10
597 nm	8 / 10
582 nm	7 / 10
682 nm	5 / 10
602 nm	4 / 10

Five wavelengths located between 507 nm and 527 nm, together with DEM information, were selected in all ten tested configurations. This result demonstrates a high degree of consistency in the feature selection process and confirms the dominant role of the blue-green spectral region identified throughout the previous analyses.

Additional wavelengths, including 582 nm, 597 nm, 602 nm, and 682 nm, were selected less frequently and therefore appear to play a secondary role in the prediction of active layer depth. The systematic selection of the 507–527 nm spectral region across all random states provides strong evidence that these wavelengths contain robust and physically meaningful information related to active layer depth variability.

Finally, the average performances reported in Table 5.14 demonstrate that the reduced feature subsets consistently outperformed the complete hyperspectral dataset.

Table 5.14: Average model performance across all tested random states.

Metric	Full 100 Bands + DEM	Optimal Top-N
Pearson r	0.700	0.801
Mean CV R^2	0.409	0.584
Global R^2	0.490	0.641
RMSE (cm)	41.56	34.86
MAE (cm)	30.60	25.21

On average, feature selection increased the Pearson correlation coefficient from 0.700 to 0.801 and improved the mean cross-validated coefficient of determination from 0.409 to 0.584. At the same time, RMSE decreased from 41.56 cm to 34.86 cm and MAE

decreased from 30.60 cm to 25.21 cm. These results confirm that the benefits of feature selection remain consistent regardless of the cross-validation partition and further support the robustness of the selected wavelengths.

Overall, the sensitivity analysis confirms that the main conclusions of this study do not depend on a particular random state or cross-validation configuration. The wavelengths located between 507 nm and 527 nm, together with DEM information, can therefore be considered robust predictors of active layer depth.

Given the strong agreement observed across the different random states, the feature subset identified using the original validation configuration (random_state = 42) was retained for the rest of the analyses. This configuration produced performance metrics that are fully representative of the average behavior observed during the sensitivity analysis while ensuring consistency with the models presented throughout the previous sections.

5.7.4 Edge-Effect Analysis

During the visual inspection of the reflectance mosaics, a noticeable edge effect was observed at several locations situated within the transition zones between adjacent flight lines. These areas appeared as degraded regions in the final reflectance mosaics and raised concerns regarding their potential influence on the subsequent machine learning analyses [36].

A first hypothesis was that these observations could behave as anomalous samples due to preprocessing artifacts introduced during the mosaicking workflow. If this were the case, retaining these points within the training dataset could potentially bias the feature selection process and affect the predictive performance of the Random Forest models.

To investigate this issue, three representative edge-effect locations were identified. For each edge-effect point, two nearby reference locations situated outside the degraded region were selected. The objective was to determine whether the edge-effect locations exhibited substantially different spectral behavior compared with neighboring observations representing similar environmental conditions.

The analysis was performed in two steps. First, the spectral signatures of the selected points were visually compared and quantitative spectral differences were evaluated. Second, the influence of these observations on model performance was assessed by repeating the Random Forest analysis after removing all identified edge-effect locations.

5.7.4.1 Spectral Signature Comparison

The spectral signatures of all selected locations are presented in Figure 5.9. Overall, the edge-effect locations and the neighboring reference points exhibit similar spectral shapes across the full wavelength range. No selected edge-effect point appears as a clear spectral outlier when compared with the rest of the observations.

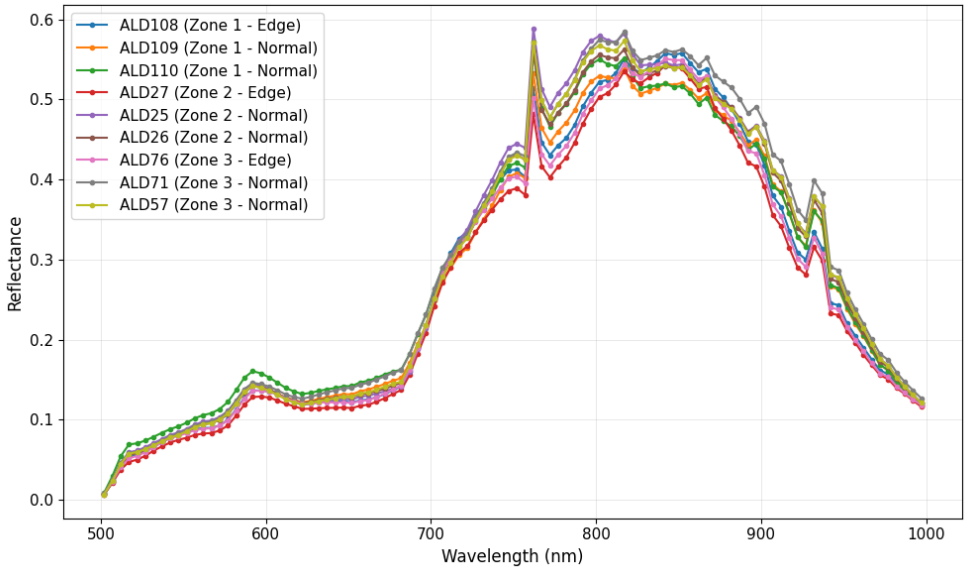
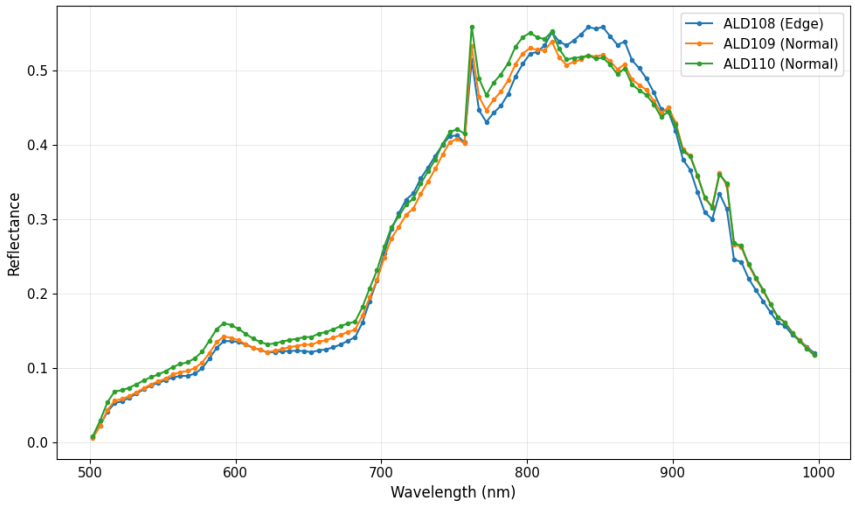
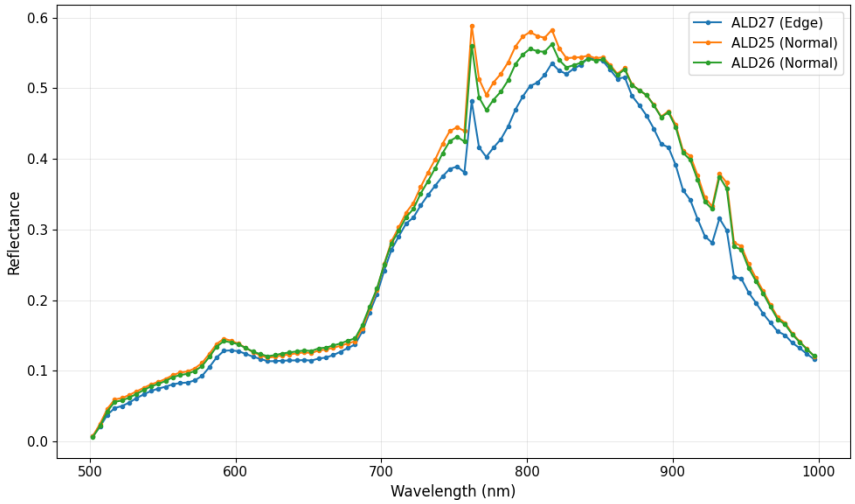


Figure 5.9: Spectral signatures of all selected locations used in the edge-effect analysis.

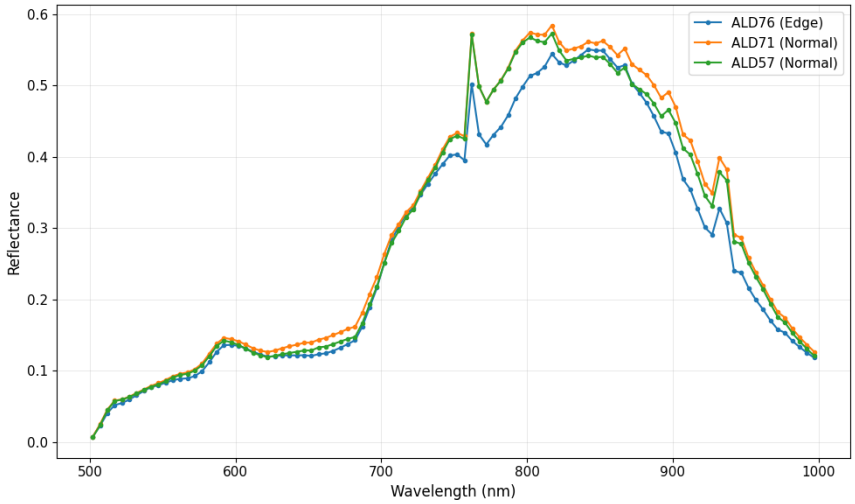
A more detailed comparison for each investigated zone is shown in Figure 5.10. In each case, the edge-effect point follows the same general spectral behavior as the two neighboring reference points. However, moderate differences in reflectance can still be observed, particularly in some wavelength regions.



(a) Zone 1.



(b) Zone 2.



(c) Zone 3.

Figure 5.10: Spectral signatures for the three investigated edge-effect zones. Each zone contains one edge-effect location and two neighboring reference locations.

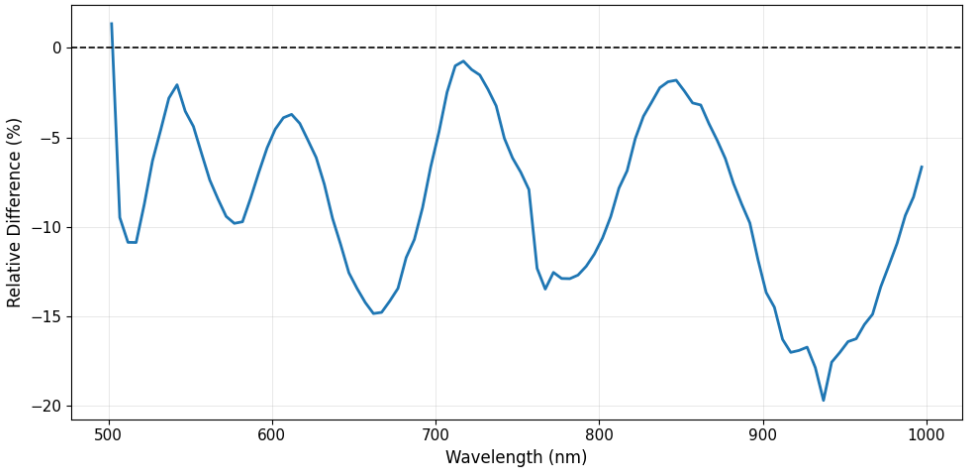
To quantify these differences, the mean absolute relative spectral difference was calculated between each edge-effect point and the two neighboring reference points. A reference-to-reference comparison was also performed within each zone in order to estimate the local spatial variability unrelated to the identified edge effect. The results are summarized in Table 5.15.

Table 5.15: Mean absolute spectral differences between edge-effect and reference locations.

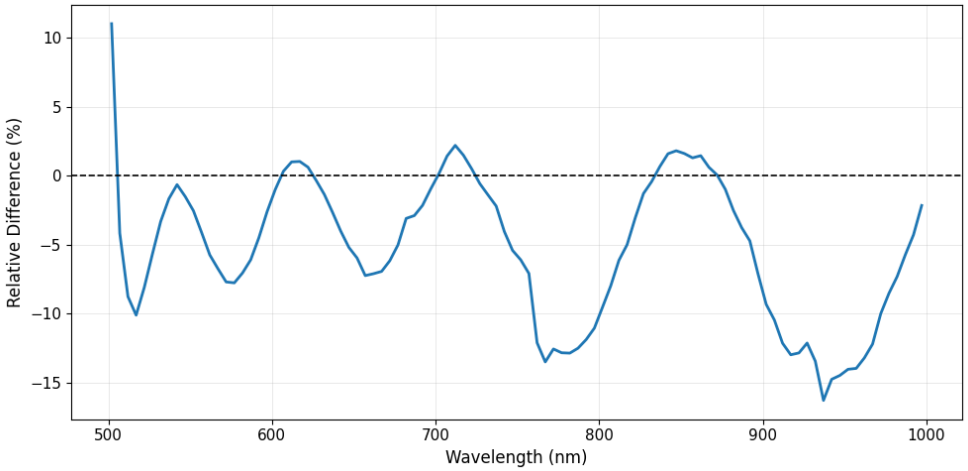
Zone	Edge vs Normal 1 (%)	Edge vs Normal 2 (%)	Normal 1 vs Normal 2 (%)
Zone 1	4.55	8.51	5.52
Zone 2	10.03	8.74	2.75
Zone 3	8.77	5.88	3.80

The calculated differences indicate that edge-effect locations generally exhibit larger spectral deviations than neighboring reference locations. This behavior is particularly clear in Zones 2 and 3, where the differences involving the edge-effect point are larger than the reference-to-reference comparison. In Zone 1, however, the differences are of the same order of magnitude, indicating that natural spatial variability also contributes to the observed spectral variability.

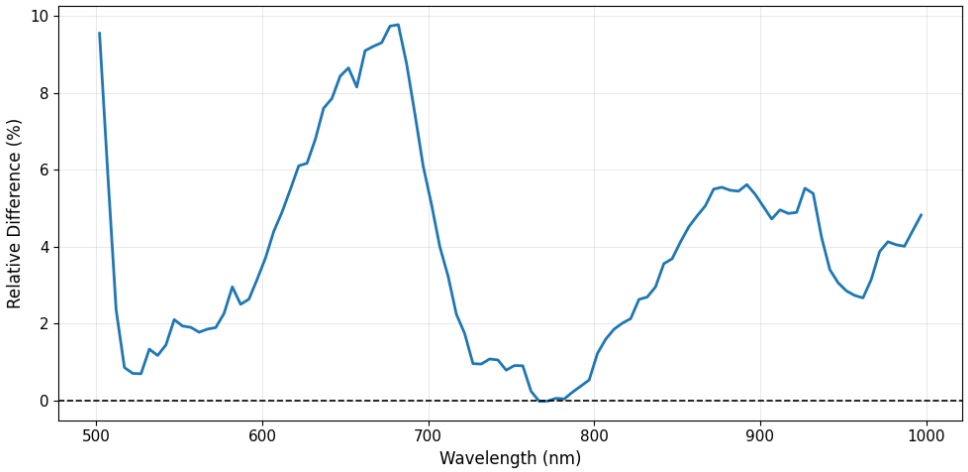
An example of the wavelength-dependent relative differences is presented in Figure 5.11 for Zone 3. The differences vary across the spectrum and are not uniform across all wavelengths. This confirms that the observed deviations do not correspond to a simple constant offset in reflectance.



(a) Edge vs Normal 1.



(b) Edge vs Normal 2.



(c) Normal 1 vs Normal 2.

Figure 5.11: Example of wavelength-dependent relative spectral differences observed in Zone 3.

It should be noted that relative differences in the lower part of the spectrum must be interpreted with caution, since reflectance values are comparatively small in this wavelength range. As a result, modest absolute reflectance differences may produce relatively large percentage variations [15].

Overall, the spectral signature analysis suggests that the edge-effect locations exhibit measurable differences relative to nearby reference observations. However, these differences remain moderate and partly comparable to the local spatial variability observed between reference points. Therefore, the spectral analysis alone is insufficient to determine whether these observations should be excluded from the dataset.

To further assess their influence, the Random Forest analysis was repeated after removing all sampling points located within the identified edge-effect regions. This provides a more direct evaluation of whether these observations behave as problematic samples or contain useful information for active layer depth prediction.

5.7.4.2 Influence of Edge-Effect Observations on Model Performance

Only the identified edge-effect observations were removed from the dataset. All other aspects of the modeling workflow remained unchanged, including the Random Forest parameters, the feature selection strategy and the 10-fold cross-validation procedure. This allows the influence of the edge-effect observations to be isolated from all other factors.

Table 5.16 compares the average performance metrics obtained using the original dataset and the dataset after removing the edge-effect observations.

Table 5.16: Comparison of the optimized Random Forest model before and after removing the identified edge-effect observations. Results correspond to the average values obtained across ten different cross-validation random states.

Metric	Original Dataset	Without Edge-Effect Points
Pearson r	0.801	0.771
Mean CV R^2	0.584	0.291
Global R^2	0.641	0.594
RMSE (cm)	34.86	36.97
MAE (cm)	25.21	26.46
Optimal Number of Features	8.4	6.9

The removal of the edge-effect observations resulted in a degradation of all performance metrics. Although the decreases in Pearson correlation coefficient and Global R^2 remained moderate, a much stronger effect was observed for the cross-validation

results. The average Mean CV R^2 decreased from 0.584 to 0.291, corresponding to a reduction of approximately 50%.

To further investigate this degradation, the Mean CV R^2 values obtained for individual random states were compared before and after removing the edge-effect observations. Representative examples are presented in Table 5.17.

Table 5.17: Influence of edge-effect removal on Mean CV R^2.

Random State	Original Dataset	Without Edge Points
Full RF (100 Bands + DEM)		
100	0.390	-0.398
309	0.435	-1.228
767	0.462	0.419
Best RF Model		
100	0.554	-0.229
309	0.587	-0.589
767	0.613	0.541

The impact of removing the edge-effect observations was found to be highly dependent on the cross-validation shuffling procedure. While certain random states, such as 767, still produced relatively stable performances after removing the identified observations, other random states exhibited dramatic degradations. For example, the Mean CV R^2 of the optimized Random Forest model decreased from 0.587 to -0.589 for random state 309, while the corresponding full model decreased from 0.435 to -1.228. Similarly, random state 100 produced negative Mean CV R^2 values for both the full and optimized models.

Such negative values indicate that the predictive performance of the model becomes worse than a simple prediction based on the mean active layer depth. More importantly, they demonstrate that the removal of the edge-effect observations substantially increases the sensitivity of the model to the random partitioning of the folds. While the original dataset consistently produced stable performances across all tested random states, the dataset without edge-effect observations generated highly variable outcomes depending on the specific distribution of samples between training and validation subsets.

These results also highlight the importance of the random-state sensitivity analysis presented in the previous section. If only a single random state had been considered, such as 767, the detrimental effect of removing the edge-effect observations could easily have remained unnoticed. Evaluating multiple cross-validation configurations therefore provides a more reliable assessment of model robustness.

Overall, the results suggest that the removed observations contain valuable information regarding the natural variability of active layer depth within the study area. Although these points were initially suspected to be affected by preprocessing artifacts, their removal systematically reduced model robustness and frequently produced unstable cross-validation results.

Consequently, the identified edge-effect observations were retained in the final dataset used throughout the remainder of this study. Despite exhibiting moderate spectral differences relative to neighboring locations, they cannot be considered simple artifacts or outliers. Instead, the results indicate that they contribute meaningful information to the Random Forest model and improve its generalization capability.

5.8 Linear Regression Analysis

While the Random Forest model demonstrated the best predictive performance throughout this study, its internal decision-making process remains difficult to interpret directly. Although feature importance rankings provide information regarding the relative contribution of each predictor, they do not explicitly describe the nature of the relationship between the predictors and active layer depth (ALT).

To gain additional insight into these relationships, a multiple linear regression analysis was performed using the most relevant predictors previously identified by the Random Forest feature selection procedure. Two models were evaluated: a spectral-only model based on the seven most important hyperspectral bands and a second model combining six spectral bands with DEM information. The objective was not to maximize predictive performance, but rather to investigate whether a simpler and more interpretable linear model could adequately describe the observed ALT variability.

Table 5.18 shows a comparison between the Linear Regression and Random Forest results.

Table 5.18: Comparison between Linear Regression and Random Forest models.

Model	r	Mean CV R^2	Global R^2	RMSE (cm)	MAE (cm)
LR (Top 7 Spectral Bands)	0.645	0.337	0.414	44.53	36.52
LR (Top Features + DEM)	0.696	0.405	0.482	41.87	34.19
RF (Optimized Model)	0.801	0.584	0.641	34.86	25.21

The inclusion of DEM information slightly improved the performance of the linear model, increasing the Pearson correlation coefficient from 0.645 to 0.696 and the Mean

CV R^2 from 0.337 to 0.405. Nevertheless, both linear models remained substantially less accurate than the Random Forest models presented previously.

The best linear model achieved a Mean CV R^2 of 0.405, compared to approximately 0.58 obtained using the optimized Random Forest model. Similarly, the Pearson correlation coefficient increased from 0.696 for the linear model to approximately 0.80 for the Random Forest approach. These results indicate that the relationship between spectral information, DEM data and active layer depth cannot be fully described using a purely linear framework [8].

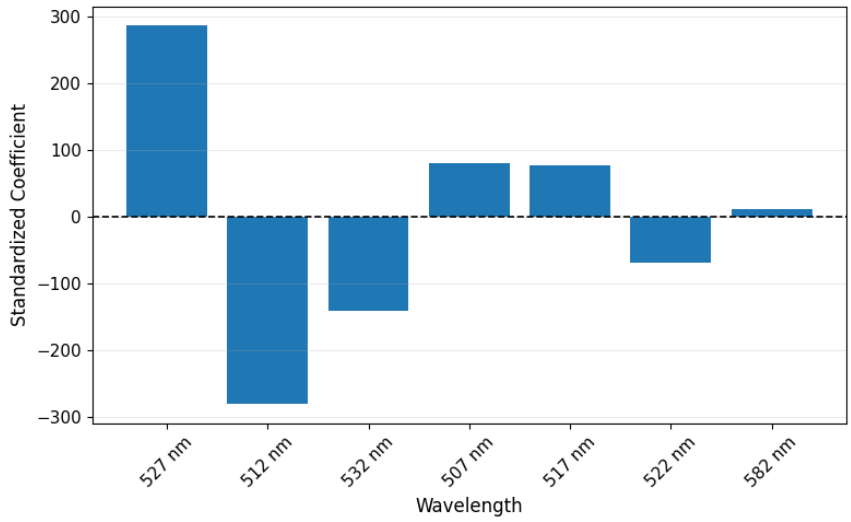


Figure 5.12: Standardized regression coefficients obtained for the linear regression model using the seven most important spectral bands selected by the Random Forest feature selection procedure. Variables are ranked according to the absolute value of their coefficients.

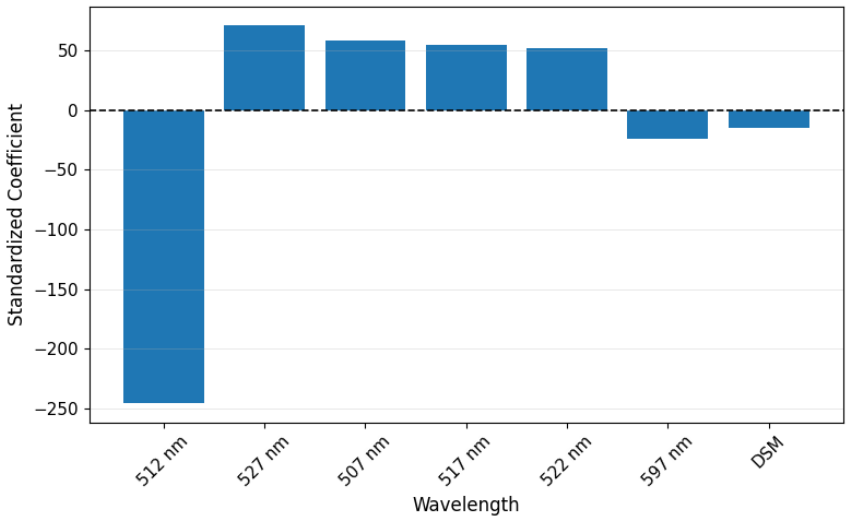


Figure 5.13: Standardized regression coefficients obtained for the linear regression model using the optimized feature set including DEM information. Variables are ranked according to the absolute value of their coefficients.

The standardized regression coefficients obtained for both linear models are presented in Figures 5.12 and 5.13. In both cases, the largest absolute coefficients were associated with wavelengths located in the green portion of the spectrum, particularly between approximately 510 and 530 nm. This observation is consistent with the Random Forest feature selection results, which also identified this spectral region as highly informative for ALT prediction.

When DEM information was included, its coefficient remained relatively small compared to those of the spectral predictors, suggesting a secondary contribution within the linear modeling framework. This result is consistent with the Random Forest analysis, where spectral information generally provided stronger predictive power than topographic information alone.

However, neighboring hyperspectral bands are strongly correlated and therefore exhibit substantial multicollinearity. As a consequence, the sign and magnitude of individual regression coefficients should be interpreted with caution. The alternating positive and negative coefficients observed for adjacent wavelengths are likely a consequence of this multicollinearity rather than evidence of direct physical relationships with active layer depth [18].

To overcome these multicollinearity constraints and achieve a more robust interpretation in future investigations, several alternative modeling frameworks could be explored. First, regularized regression techniques such as Ridge, Lasso, or Elastic Net regression could be implemented; these methods introduce a penalty term that stabilizes coefficient estimates when predictors are highly correlated [79]. Second, the

use of Partial Least Squares (PLS) regression or Principal Component Regression (PCR) would allow for the transformation of the original highly correlated bands into a reduced set of orthogonal, uncorrelated latent variables, thereby isolating the true spectral drivers of ALT without the interference of redundant information [31]. Finally, computing structural structural metrics like Variance Inflation Factors (VIF) or employing feature-grouping algorithms before running the linear models could help quantify and mitigate the impact of collinearity, ensuring that the isolated spectral regions reflect physically meaningful environmental proxies rather than statistical artifacts.

Chapter 6

Discussion

6.1 Main Findings

The objective of this thesis was to investigate the potential of UAV-based hyperspectral remote sensing for the characterization of Active Layer Depth (ALD) in Arctic tundra environments. Through a combination of spectral analysis, dimensionality reduction techniques, vegetation indices, and machine learning approaches, several important findings emerged.

First, the correlation analysis revealed consistent relationships between hyperspectral reflectance and ALD. The strongest correlations were observed within the green spectral region, particularly between approximately 507 and 532 nm, where Pearson correlation coefficients reached values close to -0.60. These results indicate that spectral information acquired by the hyperspectral sensor contains meaningful information related to active layer variability.

The comparison of extraction approaches further demonstrated that the buffer-based methods outperformed the pixel-based approach. The 2 m buffer consistently produced the strongest correlations and the best predictive performance throughout the study. This suggests that averaging spectral information over a small neighborhood reduces local noise and geolocation uncertainties while preserving relevant environmental information.

The vegetation index analysis showed that commonly used indices such as NDVI, SR, NDWI, and PRI were moderately correlated with ALD. However, none of the tested indices outperformed the best individual hyperspectral bands. This result suggests that important information related to ALD is distributed across multiple spectral regions and may not be fully captured by conventional vegetation indices.

Principal Component Analysis highlighted the highly redundant nature of hyperspectral data. More than 84% of the total variance was explained by the first principal component, indicating that a large fraction of the spectral variability was associated with overall reflectance variations. Nevertheless, the analysis of PCA loadings identified specific spectral regions contributing to the remaining variability and provided useful guidance for wavelength selection.

The Random Forest models produced the best predictive performances of the study. Feature selection demonstrated that only a limited number of wavelengths were required to achieve near-optimal results. The most important wavelengths identified by the Random Forest models were consistently located within the visible green region, in agreement with the correlation analysis.

The integration of Digital Elevation Model (DEM) information provided a measurable improvement in predictive performance. Although the contribution of DEM remained smaller than that of the most important spectral bands, the results indicate that topographic information contains complementary information related to active layer variability.

Finally, the comparison between multispectral and hyperspectral approaches confirmed the added value of hyperspectral observations. While multispectral models achieved satisfactory performances, hyperspectral data consistently produced better results, highlighting the benefits of the increased spectral resolution for environmental characterization.

6.2 Recurrent Importance of the 512 nm Wavelength

One particularly noteworthy observation is the recurrent importance of the 512 nm wavelength throughout the study. This wavelength was consistently identified among the most relevant predictors by several independent approaches, including correlation analysis, Random Forest feature importance rankings, RFECV feature selection, and linear regression models. Such consistency suggests that this spectral region contains information strongly related to the spatial variability of Active Layer Depth within the study area.

The 512 nm wavelength lies within the green portion of the visible spectrum, which is generally associated with vegetation reflectance characteristics. More specifically, this narrow band is located at the transition between pigment absorption and green reflectance, a spectral region highly sensitive to subtle variations in canopy stress and background soil-vegetation mixing [5] [63]. Since vegetation properties are known to

influence (and be influenced by) soil thermal conditions, moisture availability, and active layer dynamics, the repeated selection of this wavelength may indicate an indirect relationship between vegetation-related pigment responses and ALT variability. In permafrost ecosystems, micro-variations in thaw depth directly alter root hydrology and nutrient access, which likely translates into subtle surface stress signals captured at 512 nm. Nevertheless, the exact physical mechanisms decoupling these mixed soil-vegetation pixels remain uncertain and would require dedicated investigations beyond the scope of the present study.

6.3 Implications for Permafrost Monitoring

The results obtained in this study demonstrate that UAV hyperspectral imagery can provide valuable information for the characterization of Active Layer Depth at local scale.

It is important to emphasize that ALD cannot be directly observed from remote sensing measurements. Instead, hyperspectral sensors capture surface properties that are indirectly related to subsurface thaw dynamics. Variations in vegetation composition, vegetation vigor, moisture conditions, and surface material properties may all influence the recorded spectral response and simultaneously be linked to active layer development.

The identification of strong relationships within the visible green region suggests that vegetation-related processes play an important role in explaining ALD variability within the study area. This observation is consistent with previous studies reporting interactions between vegetation characteristics, ground thermal conditions, and permafrost dynamics.

Another important result concerns the relatively small number of wavelengths required to achieve near-optimal model performances. This finding suggests that future monitoring systems may not necessarily require the complete hyperspectral spectrum to characterize ALD. Carefully selected spectral regions could potentially provide similar predictive capabilities while reducing data dimensionality and processing requirements.

More broadly, the combination of UAV platforms and hyperspectral sensors offers a promising compromise between traditional field measurements and satellite observations. UAV acquisitions provide very high spatial resolution and operational flexibility, while hyperspectral imagery delivers detailed spectral information capable of capturing subtle environmental variations. Together, these characteristics make UAV hyperspectral remote sensing a promising tool for local-scale permafrost monitoring.

6.4 Limitations

Despite the encouraging results obtained in this study, several limitations must be acknowledged.

The first limitation concerns the relatively limited number of observations available for model development. After data cleaning, approximately 123 valid sampling locations remained available for the analyses. Although this number was sufficient to identify meaningful relationships, larger datasets would likely improve model robustness and reduce sensitivity to cross-validation partitioning.

A second limitation is related to the spatial representativeness of the study. All analyses were conducted within a single study area located near Eight Mile Lake in Interior Alaska. Consequently, the relationships identified between spectral information and ALD may be partly site-specific. Additional study sites covering different permafrost environments would be required to assess the generalizability of the results.

The study is also limited by the temporal coverage of the dataset. The analyses were performed using a single acquisition campaign acquired during late summer conditions. Seasonal variations in vegetation, moisture conditions, and thaw dynamics may influence the observed spectral relationships. Multi-temporal observations would therefore provide a more comprehensive understanding of ALD-related processes.

Another important limitation is the indirect nature of the relationship between hyperspectral observations and Active Layer Depth. Since ALD is a subsurface variable, remote sensing methods cannot directly measure it. The predictive models developed in this study therefore rely on indirect environmental indicators linked to thaw dynamics. Consequently, the identified relationships should not be interpreted as direct causal relationships.

The robustness analyses also revealed a noticeable sensitivity of the Random Forest models to the cross-validation shuffling procedure. Although the average performances remained relatively stable, substantial variations were observed for certain random states, particularly after removing the edge-effect observations. These results highlight the importance of evaluating model robustness across multiple cross-validation configurations rather than relying on a single partitioning scheme.

Finally, the linear regression analysis revealed strong multicollinearity among the selected hyperspectral bands. As a result, the individual regression coefficients could not be interpreted independently. This limitation reflects the highly correlated nature of hyperspectral datasets and further justifies the use of machine learning approaches capable of handling complex multivariate relationships.

6.5 Future Work

Several research directions could further improve the characterization of Active Layer Depth using remote sensing approaches.

A first improvement would consist of extending the analysis to multiple study sites covering different permafrost regions and environmental conditions. Such an approach would allow the development of more generalizable predictive models and improve the understanding of the environmental drivers controlling ALD variability.

The acquisition of multi-temporal hyperspectral datasets would also represent an important advancement. Repeated observations throughout the thawing season could provide valuable information regarding the temporal evolution of spectral signatures and their relationship with active layer dynamics.

Future studies could additionally investigate more advanced machine learning techniques, including gradient boosting algorithms, neural networks, or deep learning approaches. These methods may be able to exploit complex non-linear relationships not fully captured by the models evaluated in this work.

6.6 Concluding Remarks

Overall, the results obtained in this thesis demonstrate the potential of UAV-based hyperspectral remote sensing for the characterization of Active Layer Depth in Arctic tundra environments. Although several limitations remain, meaningful relationships were identified between hyperspectral reflectance and ALD, and predictive models achieved encouraging performances.

The combination of high spatial resolution, detailed spectral information, and flexible UAV acquisitions provides valuable opportunities for future permafrost monitoring applications. As hyperspectral sensors, processing workflows, and machine learning techniques continue to improve, UAV hyperspectral remote sensing is likely to play an increasingly important role in the study of permafrost dynamics and climate-related environmental change.

Chapter 7

Conclusion

This thesis investigated the potential of UAV-based hyperspectral remote sensing for the characterization of Active Layer Depth in a discontinuous permafrost environment located near Eight Mile Lake, Alaska. A complete processing workflow was developed to transform raw hyperspectral acquisitions into analysis-ready reflectance products, providing the basis for a detailed investigation of the relationships between spectral information and ALD variability.

The different analyses demonstrated that hyperspectral imagery contains meaningful information related to Active Layer Depth. Correlation analyses revealed consistent relationships between several spectral bands and ALD, with the strongest correlations reaching approximately $|r| = 0.60$. The use of spatial averaging through buffer-based extraction significantly improved the results compared with pixel-based approaches, highlighting the importance of accounting for spatial variability and geolocation uncertainties.

Vegetation index analyses showed that conventional indices such as NDVI and Simple Ratio were moderately correlated with ALD, although their predictive power remained lower than that of several individual hyperspectral bands. Principal Component Analysis confirmed the presence of strong spectral redundancy, with the first principal component explaining more than 80% of the total variance. PCA-based feature selection nevertheless identified spectral regions consistent with those highlighted by the correlation analyses.

Among the tested machine learning approaches, Random Forest proved to be the most effective. Feature selection enabled a substantial reduction in dimensionality while preserving predictive performance, and the integration of DEM information further improved the results. The optimized Random Forest model achieved a Pearson correlation coefficient of 0.801, a mean cross-validation R^2 of 0.592, and a global R^2 of 0.641,

demonstrating the potential of combining hyperspectral and topographic information for ALD estimation.

Several robustness analyses were also conducted. The sensitivity analysis confirmed that model performance remained relatively stable across multiple cross-validation configurations, while the RFECV results largely supported the wavelength selection obtained through Random Forest feature importance. The edge-effect analysis further demonstrated that the identified observations should not be considered simple artifacts, as their removal systematically reduced model robustness and predictive performance.

One particularly notable result was the recurrent importance of the 512 nm wavelength, which consistently emerged among the most informative predictors across multiple independent analyses. Although the exact physical mechanisms remain uncertain, this observation suggests that specific spectral regions within the green portion of the visible spectrum may contain valuable information related to environmental factors influencing Active Layer Depth variability.

Despite these encouraging results, several limitations remain. The study relied on a relatively limited number of field observations collected within a single study area, and the indirect relationship between surface spectral properties and subsurface thaw depth remains inherently complex. Additional investigations involving larger datasets, multiple sites, and complementary environmental variables would be required to improve model generalization and physical interpretability.

Overall, this work demonstrates that UAV-based hyperspectral remote sensing represents a promising approach for the characterization of Active Layer Depth at local scales. By combining high spatial and spectral resolution observations with machine learning techniques, hyperspectral imagery can provide valuable insights into permafrost-related environmental variability and contribute to the development of future monitoring strategies in rapidly changing Arctic environments.

Appendix A

Additional Orthomosaics

Additional RGB orthomosaics generated from the remaining UAV campaigns are presented in this appendix.

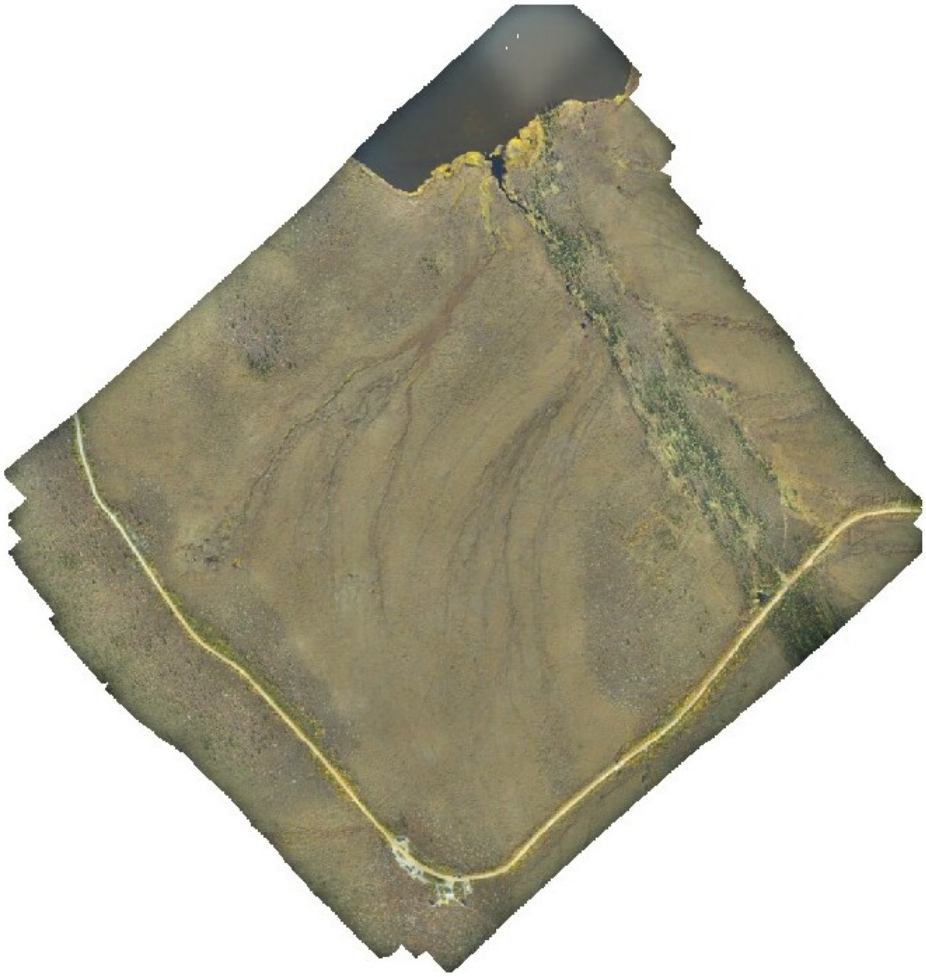


Figure A.1: RGB orthomosaic generated from Campaign 3.



Figure A.2: RGB orthomosaic generated from Campaign 5.



Figure A.3: RGB orthomosaic generated from Campaign 6.

Bibliography

[1] Adobe. Tiff files, 2025.

[2] Telmo Adão, Jonatan Hruška, Luís Pádua, J. Sousa, Emanuel Peres, Raul Morais, and J. J. Sousa. Hyperspectral imaging: A review of its applications and chain processing for unmanned aerial vehicles (uavs). *Remote Sensing*, 9(11):1110, 2017.

[3] Agisoft Forum. Tiff format support discussion, 2025.

[4] Christophe Ambroise and Geoffrey J. McLachlan. Selection bias in gene extraction on the basis of microarray expression data. *Proceedings of the National Academy of Sciences*, 99(10):6562–6566, 2002.

[5] Gregory P. Asner. Biophysical and biochemical sources of variability in canopy reflectance. *Remote Sensing of Environment*, 64(3):234–253, 1998.

[6] Jose M. Bioucas-Dias, Antonio Plaza, Gustavo Camps-Valls, Paul Scheunders, Nasser Nasrabadi, and Jocelyn Chanussot. Hyperspectral remote sensing data analysis and future challenges. *IEEE Geoscience and Remote Sensing Magazine*, 1(2):6–36, 2013.

[7] Leo Breiman. Random Forests. *Machine Learning*, 45(1):5–32, 2001.

[8] Leo Breiman. Statistical modeling: The two cultures (with comments and a rejoinder by the author). *Statistical Science*, 16(3):199–231, 2001.

[9] Jerry Brown, Kenneth M. Hinkel, and Frederick E. Nelson. The circumpolar active layer monitoring (calm) program: Data collection, management, and dissemination strategies. 2000.

[10] Jorge A. S. Centeno, J. Kerm, E. A. Mitishita, and Mario E. J. Palma. PCA Band Selection Method for a Hyperspectral Sensors Onboard an UAV. In *Proceedings of the 2020 IEEE Latin American GRSS & ISPRS Workshop (LAGIRSS)*, pages 77–82, 2020.

[11] D. Chutia, D. K. Bhattacharyya, K. K. Sarma, R. Kalita, and S. Sudhakar. Hyperspectral remote sensing classifications: A perspective survey. *Transactions in GIS*, 20(4), 2016.

[12] Circumpolar Active Layer Monitoring (CALM). Active layer monitoring, 2025.

[13] Circumpolar Active Layer Monitoring (CALM). Circumpolar active layer monitoring program, 2025.

[14] Copernicus Programme. Sentinel-2, 2025.

[15] Paul J. Curran and Jennifer L. Dungan. Estimation of signal-to-noise ratios for geographic information systems and remote sensing. *International Journal of Remote Sensing*, 10(9):1423–1428, 1989.

[16] Baptiste Dafflon, Susan Hubbard, Kirstin Elger, Sebastian Uhlemann, Ian Shirley, and John Peterson. High-resolution characterization of active layer thickness and its relation to vegetation and topography using airborne remote sensing and machine learning. *Remote Sensing of Environment*, 184:421–432, 2016.

[17] Witold Dobiński. Permafrost. *Earth-Science Reviews*, 2020.

[18] Carsten F. Dormann, Jane Elith, Sven Bacher, Carsten Buchmann, Gudrun Carl, Gabriel Carré, Jírgen R. G. Marquéz, Bernd Gruber, Benjamin Lafourcade, Pedro J. Leitão, and et al. Collinearity: a review of methods to deal with it and a simulation study evaluating their performance. *Ecography*, 36(1):27–46, 2013.

[19] European Space Agency. Hyperspectral image data cube, 2014.

[20] European Space Agency. Permafrost, 2025.

[21] Mark A. Fonstad, James T. Dietrich, Brittany C. Courville, Jennifer L. Jensen, and Patrice E. Carbonneau. Topographic structure from motion: A new development in photogrammetric measurement. *Earth Surface Processes and Landforms*, 38(4):421–430, 2013.

[22] Global Terrestrial Network for Permafrost. Measurement recommendations and guidelines, 2025.

[23] Global Terrestrial Network for Permafrost. Measurement standards and monitoring guidelines, 2025.

[24] Global Terrestrial Network for Permafrost. Permafrost, 2025.

[25] Alexander F. H. Goetz, Gregg Vane, John E. Solomon, and Barrett N. Rock. Imaging spectrometry for earth remote sensing. *Science*, 228(4704):1147–1153, 1985.

[26] Megandhren Govender, Kershani Chetty, and Hartley Bulcock. A review of hyperspectral remote sensing and its application in vegetation and water resource studies. *Water SA*, 33, 2009.

[27] GRID-Arendal. Permafrost in the northern hemisphere, 2020.

[28] Isabelle Guyon, Jason Weston, Stephen Barnhill, and Vladimir Vapnik. Gene selection for cancer classification using support vector machines. *Machine Learning*, 46(1):389–422, 2002.

[29] HAIP Solutions. Hyperspectral cameras, 2025.

[30] Tobias B. Hank, Katja Berger, Heike Bach, Jan G. P. W. Clevers, Anatoly Gitelson, Pablo Zarco-Tejada, and Wolfram Mauser. Spaceborne imaging spectroscopy for sustainable agriculture: Contributions and challenges. *Surveys in Geophysics*, 40:515–551, 2019.

[31] Trevor Hastie, Robert Tibshirani, and Jerome Friedman. Feature selection and shrinkage methods for high-dimensional data in remote sensing. *Remote Sensing of Environment*, 240:111–125, 2020.

[32] Zeke Hausfather. What is permafrost? q&a, 2018.

[33] Gordon F. Hughes. On the mean accuracy of statistical pattern recognizers. *IEEE Transactions on Information Theory*, 14(1):55–63, 1968.

[34] Intergovernmental Panel on Climate Change (IPCC). Annex vii: Glossary, 2021.

[35] IPCC. Changes in snow, ice and frozen ground, 2007.

[36] S. Jakob, R. Zimmermann, and R. Gloaguen. Radiometric normalization of UAV-based hyperspectral data for multi-temporal vegetation monitoring. *Remote Sensing*, 9(11):1166, 2017.

[37] Gareth James, Daniela2 Witten, Trevor Hastie, and Robert Tibshirani. *An Introduction to Statistical Learning: with Applications in R.* Springer, New York, 2013.

[38] Mike R. James, Stuart Robson, Sebastian d'Oleire Oltmanns, and Uwe Niethammer. Optimising uav topographic surveys processed with structure-from-motion: Ground control quality, quantity and bundle adjustment. *Geomorphology*, 280:51–66, 2017.

[39] John R. Jensen. *Remote Sensing of the Environment: An Earth Resource Perspective*. Pearson Prentice Hall, Upper Saddle River, NJ, 2nd edition, 2007.

[40] Ian T. Jolliffe. *Principal Component Analysis*. Springer, 2002.

[41] François Jonard. Remote sensing, 2025. Course material, University of Liège.

[42] Jussi Juola, Jaan Rönkkö, Aarne Hovi, and Miina Rautiainen. Biophysical variables of tree canopies in northern peatlands from hyperspectral enmap imagery. *Ecological Informatics*, 92, 2025.

[43] Max Kuhn and Kjell Johnson. *Applied Predictive Modeling*. Springer, New York, NY, 2013.

[44] W. Kurz, K. Wang, F. Bektas, et al. Dimensionality reduction in hyperspectral imaging using standard deviation-based band selection for efficient classification. *Scientific Reports*, 15, 2025.

[45] Andreas Kääb. Remote sensing of permafrost-related problems and hazards. *Permafrost and Periglacial Processes*, 2008.

[46] Arthur H. Lachenbruch. Permafrost, the active layer, and changing climate, 1994.

[47] Kaixi Liao, Zhaoying Zhou, and Cheng Yang. Comparing lidar and sfm digital surface models for three land cover types. *Open Geosciences*, 13(1):391–404, 2021.

[48] N. Lopes Bento, G. Araújo E Silva Ferraz, R. Alexandre Pena Barata, L. Santos Santana, B. Diennevan Souza Barbosa, L. Conti, and G. Rossi. Overlap influence in images obtained by an unmanned aerial vehicle on a digital terrain model of altimetric precision. *European Journal of Remote Sensing*, 55(1), 2022.

[49] Gilles Louppe, Louis Wehenkel, Antonio Sutera, and Pierre Geurts. Understanding variable importances in forests of randomized trees. *Advances in Neural Information Processing Systems (NeurIPS)*, 26:431–439, 2013.

[50] Bing Lu, Yuhong He, and Phuong D. Dao. Comparing the performance of multispectral and hyperspectral images for estimating vegetation properties. *IEEE Journal of Selected Topics in Applied Earth Observations and Remote Sensing*, 2019.

[51] Salvatore Manfreda, Matthew F. McCabe, Pauline E. Miller, Richard Lucas, Victor Pajuelo Madrigal, Giorgos Mallinis, Eyal Ben Dor, David Helman, Lyndon Estes, Giuseppe Ciraolo, et al. On the use of unmanned aerial systems for environmental monitoring. *Remote Sensing*, 10(4):641, 2018.

[52] David F. Maune. Digital elevation model technologies and applications. 2007.

[53] Gonzalo Morales, John W. Sheppard, Robert D. Logan, and Joseph A. Shaw. Hyperspectral dimensionality reduction based on inter-band redundancy analysis and greedy spectral selection. *Remote Sensing*, 13(18):3649, 2021.

[54] Mavuto M. Mukaka. *A Guide to Appropriate Use of Correlation Coefficient in Medical Research*. 2012.

[55] National Aeronautics and Space Administration (NASA). Mission: Landsat satellites, 2025.

[56] T. E. Osterkamp, M. T. Jorgenson, E. A. G. Schuur, Y. L. Shur, M. Z. Kanevskiy, J. G. Vogel, and V. E. Tumskoy. Physical and ecological changes associated with warming permafrost and thermokarst in interior alaska. *Permafrost and Periglacial Processes*, 20:235–256, 2009.

[57] Mahesh Pal. Random forest classifier for remote sensing applications. *International Journal of Remote Sensing*, 26(21):4917–4922, 2005.

[58] Mahesh Pal and Paul M. Mather. Dimensionality reduction of hyperspectral data using data transformation methods: A comparative study. *International Journal of Remote Sensing*, 22(5):873–879, 2001.

[59] Marius Philipp, Andreas Dietz, Sebastian Buchelt, and Claudia Kuenzer. Trends in satellite earth observation for permafrost related analyses—a review. *Remote Sensing*, 2021.

[60] Ruiliang Pu and Peng Gong. Band Selection from Hyperspectral Data for Conifer Species Identification. *Geographic Information Sciences*, 6(2):127–133, 2000.

[61] Pauli Putkiranta, Aleksi Räsänen, Pasi Korpelainen, Rasmus Erlandsson, Tiina H. M. Kolari, Yuwen Pang, Miguel Villoslada, Franziska Wolff, Timo Kumpula, and Tarmo Virtanen. The value of hyperspectral uav imagery in characterizing tundra vegetation. *Remote Sensing of Environment*, 308, 2024.

[62] B. Raychaudhuri. Imaging spectroscopy: Origin and future trends. *Applied Spectroscopy Reviews*, 51(1):23–35, 2016.

[63] Martha K. Raynolds, Donald A. Walker, Howard E. Epstein, Jorge E. Pinzon, and Compton J. Tucker. A new estimate of tundra-biome phytomass from trans-arctic field data and its relationship to heating. *Remote Sensing Letters*, 3(5):403–411, 2012.

[64] J. W. Rouse, R. H. Haas, J. A. Schell, and D. W. Deering. Monitoring the vernal advancement and retrogradation (green wave effect) of natural vegetation. In *NASA 3rd Earth Resources Technology Satellite (ERTS) Symposium*, pages 309–317, 1974.

[65] Daniel Schläpfer. *PARGE — Parametric Geocoding and Orthorectification for Airborne Imaging Spectrometers: User Manual, Version 3.4*. ReSe Applications GmbH, Wil, Switzerland, 2018.

[66] Daniel Schläpfer and Rudolf Richter. Geo-atmospheric processing of airborne imaging spectrometry data. part 1: Parametric orthorectification. *International Journal of Remote Sensing*, 23(13):2609–2630, 2002.

[67] Daniel Schläpfer, Rudolf Richter, and Thomas Popp. Drone data atmospheric correction concept for multi- and hyperspectral imagery — the droacor model. *The International Archives of the Photogrammetry, Remote Sensing and Spatial Information Sciences*, XLIII-B3-2020:473–478, 2020.

[68] E. A. G. Schuur, A. D. McGuire, C. Schädel, et al. Climate change and the permafrost carbon feedback. *Nature*, 2015.

[69] Edward A. G. Schuur, James Bockheim, Josep G. Canadell, et al. Vulnerability of permafrost carbon to climate change: Implications for the global carbon cycle, 2008.

[70] Edward A. G. Schuur, Kathryn G. Crummer, Jason G. Vogel, and Michelle C. Mack. Plant species composition and productivity following permafrost thaw and thermokarst in alaskan tundra. *Ecosystems*, 10:280–292, 2007.

[71] M. W. Smith and D. W. Riseborough. Permafrost monitoring and detection of climate change. *Permafrost and Periglacial Processes*, 7(4):301–309, 1996.

[72] Juha Suomalainen, Nils Anders, Muhammad Naveed Iqbal, Gerbert Roerink, Jappe Franke, Harm Bartholomeus, and Lammert Kooistra. A lightweight hyperspectral mapping system and photogrammetric processing chain for unmanned aerial vehicles. *Remote Sensing*, 6(11):11013–11030, 2014.

[73] Darren Turner, Arko Lucieer, and Luke Wallace. Direct georeferencing of ultrahigh-resolution uav imagery. *IEEE Transactions on Geoscience and Remote Sensing*, 52(5):2738–2745, 2014.

[74] University of Alaska Fairbanks. Frost tubes, 2025.

[75] Maëlle Villani, Elisabeth Mauclet, Yannick Agnan, Arsène Druel, Briana Jasinski, Meghan Taylor, Edward A. G. Schuur, and Sophie Opfergelt. Mineral element recycling in topsoil following permafrost degradation and a vegetation shift in sub-arctic tundra. *Geoderma*, 421, 2022.

[76] C. Wang, X. Yang, X. Xi, S. Nie, and P. Dong. *Introduction to LiDAR Remote Sensing*. CRC Press, 1 edition, 2024.

[77] Matthew J. Westoby, James Brasington, Neil F. Glasser, Michael J. Hambrey, and John M. Reynolds. Structure-from-motion photogrammetry: A low-cost, effective tool for geoscience applications. *Geomorphology*, 179:300–314, 2012.

[78] Cort J. Willmott and Kenji Matsuura. Advantages of the mean absolute error (MAE) over the root mean square error (RMSE) in assessing average model performance. *Climate Research*, 30(1):79–82, 2005.

[79] Svante Wold, Michael Sjöström, and Lennart Eriksson. Pls-regression: a basic tool of chemometrics. *Chemometrics and Intelligent Laboratory Systems*, 58(2):109–130, 2001.

[80] Paul R. Wolf, Bon A. Dewitt, and Benjamin E. Wilkinson. *Elements of Photogrammetry with Applications in GIS*. McGraw-Hill Education, 4 edition, 2014.

[81] Jiali Xue and Baofeng Su. Significant remote sensing vegetation indices: A review of developments and applications. *Journal of Sensors*, 2017:1–17, 2017.

[82] Caiyun Zhang, Thomas A. Douglas, and John E. Anderson. Mapping vegetation and seasonal thaw depth in central alaska using airborne hyperspectral and lidar data. In *IGARSS 2020 IEEE International Geoscience and Remote Sensing Symposium*, pages 3070–3073, 2020.

[83] Caiyun Zhang, Thomas A. Douglas, and John E. Anderson. Modeling and mapping permafrost active layer thickness using field measurements and remote sensing techniques. *International Journal of Applied Earth Observation and Geoinformation*, 102, 2021.

[84] Zhengxin Zhang and Lixue Zhu. A review on unmanned aerial vehicle remote sensing: Platforms, sensors, data processing methods, and applications. *Drones*, 7(6):398, 2023.